University of Cape Town

Submitted is partial fulfilment of the requirements for the master's degree

Masters Dissertation

The study of intermetallic particles in aluminium alloy AA3104 can-body stock during homogenisation

Livhuwani Tessa Magidi

Supervisor: Dr Sarah L. George

Co-supervisor: Prof Robert D. Knutsen

March 2017

PLAGARISM DECLARATION

1. "I know the meaning of plagiarism and declare that all the work in the document, save for that which is properly acknowledged, is my own. This thesis/dissertation has been submitted to the Turnitin module (or equivalent similarity and originality checking software) and I confirm that my supervisor has seen my report and any concerns revealed by such have been resolved with my supervisor."

2. Each significant contribution to, and quotation in, this project from the work, or works of other people has been attributed and has cited and referenced.

3. This project is my own work.

4. I have not allowed, and will not allow, anyone to copy my work with the intention of passing it off as his or her own work.

5. I acknowledge that copying someone else's assignment or project, or part of it, is wrong, and declare that this is my own work.

Livhuwani Tessa Magidi

SIGNATURE: Signed by candidate

DATE: 12 March 2017

EBE Faculty: Assessment of Ethics in Research Projects (Rev2)

Any person planning to undertake research in the Faculty of Engineering and the Built Environment at the University of Cape Town is required to complete this form before collecting or analysing data. When completed it should be submitted to the supervisor (where applicable) and from there to the Head of Department. If any of the questions below have been answered YES, and the applicant is NOT a fourth year student, the Head should forward this form for approval by the Faculty EIR committee: submit to Ms Zulpha Geyer (Zulpha.Geyer@uct.ac.za; Chem Eng Building, Ph 021 650 4791).
NB: A copy of this signed form must be included with the thesis/dissertation/report when it is submitted for examination

This form must only be completed once the most recent revision EBE EiR Handbook has been read.

Name of Principal Researcher/Student: LIVHUWANI MAGIDI Department: MECHANICAL ENGINEERING

Preferred email address of the applicant: mgdliv002@myuct.ac.za

If a Student: Degree: MASTERS IN MATERIALS ENGINEERING Supervisor: Dr SARAH GEORGE

If a Research Contract indicate source of funding/sponsorship:

Research Project Title: HOMOGENISATION OF ALUMINIUM ALLOY AA3104

Overview of ethics issues in your research project:

Question 1: Is there a possibility that your research could cause harm to a third party (i.e. a person not involved in your project)?	YES	NO X
Question 2: Is your research making use of human subjects as sources of data? If your answer is YES, please complete Addendum 2.	YES	NO X
Question 3: Does your research involve the participation of or provision of services to communities? If your answer is YES, please complete Addendum 3.	YES	NO X
Question 4: If your research is sponsored, is there any potential for conflicts of interest? If your answer is YES, please complete Addendum 4.	YES	NO X

If you have answered YES to any of the above questions, please append a copy of your research proposal, as well as any interview schedules or questionnaires (Addendum 1) and please complete further addenda as appropriate. Ensure that you refer to the EiR Handbook to assist you in completing the documentation requirements for this form.

I hereby undertake to carry out my research in such a way that

- there is no apparent legal objection to the nature or the method of research; and
- the research will not compromise staff or students or the other responsibilities of the University;
- the stated objective will be achieved, and the findings will have a high degree of validity;
- limitations and alternative interpretations will be considered;
- the findings could be subject to peer review and publicly available; and
- I will comply with the conventions of copyright and avoid any practice that would constitute plagiarism.

Signed by:

	Date
Principal Researcher/Student:	06/06/2013

This application is approved by:

Supervisor (if applicable):	06/06/2013
HOD (or delegated nominee): *Final authority for all assessments with NO to all questions and for all undergraduate research.*	07/06/2013
Chair : Faculty EIR Committee For applicants other than undergraduate students who have answered YES to any of the above questions.	

ACKNOWLEDGEMENTS

I would like to express my sincere thanks to God the Almighty and to the following people:

Dr Sarah George my supervisor for the help, the guidance and equipment use around the lab when conducting my research

Professor Robert Knutsen for the advice and further guidance on how to approach my research

The staff and students of the Centre of Materials Engineering (CME) for the encouragement and help around the lab

Penny Park- Ross for the assistance in the lab with regards to our project needs and more

Velile Vilane for the help on equipment use around the (CME) lab

Peter Dobias from the Department of Chemical Engineering workshop for designing and making the autoclave (pressure vessel) used in this research

Tracy Booysen from the Department of Mechanical Engineering for coding a MATLAB script used in image analysis

Nico Fischer and Kirsten Corin from the Department of Chemical Engineering for X-ray diffraction (XRD) conduction and analysis, respectively

Dr Hong Su from the Department of Chemistry for XRD conduction

Mudindivhathu Tshivhombela from the Department of Mechanical Engineering for designing and making the gas purifier used in this research

Miranda Waldron and Dr Innocent Shuro from the Centre for Imaging and Analysis

The Department of Mechanical Engineering workshop for the mechanical support

Kumar Sundaram from the University of Oxford for guidance on how to adapt the SiBut method (particle extraction process)

Tim Low from the Education Development Unit for the statistical help

My family for the support and encouragement

UCT Carnegie Scholarship for women in Science and Engineering for sponsoring my studies and giving me the opportunity to study further

And Hulamin for supplying the samples and the project as well as financial support (It has been an honour working on this project)

CONTENTS

LIST OF FIGURES

LIST OF TABLES

LIST OF EQUATIONS

ABSTRACT

Aluminium alloy AA3104 is commonly used for the manufacture of beverage can bodies. This alloy has excellent formability and strength properties. The evolution of the AA3104 microstructure and intermetallic particles during thermo-mechanical processing (TMP) has a direct impact on quality parameters, which influence the formability of the material during beverage can deep drawing and wall ironing. These parameters are earing, tear-off and galling resistance. During homogenisation of AA3104 direct chill (DC) ingot, there is a phase transformation from β-Al_6(Fe,Mn) orthorhombic phase to the harder α-Al_x(Fe,Mn)$_3Si_2$ cubic phase.

Phase transformation occurs by diffusion of Si and Mn, where diffusion of Mn determines the rate of transformation. The presence of the α-phase intermetallic particles is crucial for galling resistance, thus improving the formability of the material. Ideal galling resistance requires 1-3% total volume fraction (VF) of intermetallic particles, 50% of which should be the harder α-phase. The homogenisation treatment variables, such as temperature, as well as the effect of the intermetallic particle VFs with the correct β to α ratio is investigated.

The aim of this research is to characterise intermetallic particles in the as-cast condition and investigate the evolution of particles as a result of a two-step homogenisation treatment, where the primary step temperature was varied between 560^0C and 580^0C, and the secondary step was performed at 520^0C. The characterisation process involves particle phase identification using compositional and morphological analysis. A particle extraction setup is then used to extract intermetallic particles from the bulk specimen by dissolving Al matrix in dry butanol and those particles are analysed. The evolution of volume fraction of particles and their distribution is then investigated using light microscopy, image analysis, XRD and the Rietveld method.

The SEM micrographs show a larger quantity of smaller, more closely dispersed intermetallic particles at the edge of the ingot, compared to those at the centre. The β-Al_6(Fe,Mn) phase is more geometric in shape, while the α-Al_x(Fe,Mn)$_3Si_2$ phase comprises isolated areas of Al-matrix within the particle centres (Chinese-script like). The phases are distinguished based on morphological identification using SEM and compositional identification using EDS, where Si content within the α–phase is used to differentiate between the phases. XRD patterns with the Rietveld method show the presence of β and α as the major phase particles within the homogenised specimens near the edge and at the centre.

Phase quantification using 2-D analysis and particle extraction shows more α-phase near the edge and less α-phase at the centre. The two techniques agree in trend but differ in values. The particle extraction analysis is more trustworthy than 2-D particle analysis, where error is suggested to arise during thresholding in 2-D microstructural analysis. Additionally, homogenisation at 580°C/520°C yields more α-phase than homogenisation at 560°C/520°C both near the edge and at the centre of the ingot.

Important observations emerge from this study: (i) Microstructural [two-dimensional (2-D)] and particle extraction [three-dimensional (3-D)] techniques agree when it comes to microstructural qualification and tend to slightly differ on particle quantification (value obtained from both techniques), (ii) both techniques show the presence of α and β phases, as well as reveal the morphological differences within the particles, (iii) both techniques show similar trends of high amount of β-phase during as-cast and an increase in α-phase after homogenisation due to phase transformation. Additionally, phase quantification reveals that more α-phase near the edge and less α-phase at the centre, and (iv) homogenisation at 560°C/520°C yields α-phase VF which is closer to the desired β→α ratio of 50% compared to homogenisation at 580°C/520°C.

Therefore, homogenisation at 560°C/520°C is the better homogenisation treatment temperature option. Furthermore, both 2-D microstructural analysis and particle extraction analysis are reliable techniques that complement each other when qualitatively and quantitatively studying the evolution of intermetallic particles in aluminium alloy AA3104 can-body stock during homogenisation. However, particle extraction analysis has been shown to have a higher accuracy, thus is deemed more reliable.

1 INTRODUCTION

1.1 Background and motivation to the investigation

In 2015, South Africa moved to the production of all aluminium beverage can, which is fast becoming the only beverage can available in South Africa. Hulamin rolled product is the majority supplier and producer of the beverage can-body stock material, namely AA3104-H19 rolled sheet. This is a relatively new product, thus Hulamin is driving for the optimisation of the processing route.

The driving force for the use of an aluminium beverage can is because the material is light weight which is advantageous for packaging and shipping, has high recyclability, has high quality surface, formable and improved strength for filling. Most importantly 100% of Al can-body is made of recyclable Al, while only 25% of a steel can-body is made of recyclable steel [1]. Recycling a single Al beverage can saves enough energy to power a television for three hours or burn a 100-watt light bulb [2]. When energy is saved, manufacturing companies make a profit.

The production of AA3104 sheet metal for the manufacture of beverage can bodies is complex due to very stringent requirements of the final sheet. Therefore, it is important that caution is taken when processing beverage can sheets. Caution is taken by tight control on processes from casting through to final stages of cold rolling the can-body sheet. This is to obtain a desired random texture and grain structure in the metal, including size and distribution of the intermetallic phases and non-intermetallic inclusions. Al can-body stock is a very demanding product for the simple reason that a large proportion of its strip is severely “tested” during drawing and wall ironing when can-body forming. When processing can-bodies, there must be focus on the sheet’s strength, formability, earing and galling. Can-body sheets must have good strength, be formable, and have better earing properties and good galling resistance. Thus, texture and microstructure of alloy during homogenisation is important. Homogenisation of AA3XXX DC-cast ingot results in some microstructural changes. These changes include even distribution across grains and dendrites, intermetallic particle phase transformation from the β–$Al_6(Fe,Mn)$ form to the harder α-$Al_x(Fe,Mn)_3Si_2$ form, as well as Mn in solid solution supplying growth of existing intermetallic particles.

The aim of this research is to detect the extent to which the intermetallic particles evolve from β–Al_6(Fe,Mn) form to harder α-Al_x(Fe,Mn)$_3Si_2$ form during homogenisation in order to prevent galling. This is achieved using 2-dimensional (2-D) microstructural analysis and 3-dimensional (3-D) particle extraction analysis. Sufficient galling resistance requires a significantly harder phase of approximately 50% volume fraction in the alloy's microstructure. This is done by performing two-step homogenisation treatments on AA3104, with a variation of 560°C/520°C and 580°C/520°C as the first step while keeping the second step at 520°C. This is to get the correct intermetallic particle composition ratio before hot rolling, which allows for drawing and wall ironing of beverage can sheets without any occurrence of galling.

1.2 Objectives of the report

The objectives of this study are to:

- Assess the transformation, compositional and morphological evolution of intermetallic phases during homogenisation.
- Evaluate reliable testing methods that identify the intermetallic phases and measure their volume fractions in AA3104 alloy.
- Investigate the effect of homogenisation temperature on the evolution of the intermetallic phase particles.
- Determine which homogenisation temperature yields the desired volume fraction of intermetallic particles with a correct ratio of β and α phases.

1.3 Methodology

To achieve the objectives of this research, experiments were performed and results were analysed. Firstly, specimens were cut to desired pieces. Then they were put in a programmable furnace and homogenised at different homogenisation temperatures. Specimens were then metallographically prepared for image analysis by grinding, polishing and etching. The alloy's microstructure was then characterised using light microscopy and scanning electron microscopy (SEM) coupled with energy dispersive spectroscopy (EDS). After that, image analysis was performed on a high number of micrographs for intermetallic particle volume fraction estimation.

Furthermore, particle extraction was conducted on both as-cast and homogenised specimens. The extracted particles were then characterised using SEM coupled with EDS. Using the particle extraction technique based on the SiBut method, X-ray diffraction (XRD) together with the Rietveld method was used to identify and quantify the phases within the extracted particle respectively. Lastly, results obtained were then combined to give a clear picture of how the composition of intermetallic particles evolved during homogenisation.

1.4 Scope and limitations of the investigation

The purpose of this project is to qualitatively and quantitatively investigate the evolution of intermetallic particles in aluminium alloy AA3104 can-body stock during homogenisation that is performed prior to the commencement of hot rolling. Of importance in this research is to assess the microstructural changes as well as volume fraction (VF) of the primary α- and β-intermetallic particle phases using 2-D and particle extraction techniques. These particles are important because they promote particle stimulated nucleation (PSN) and the correct β- to α-phase ratio which improves galling resistance during thermo-mechanical processing (TMP).

This study focused on qualitatively and quantitatively investigating the evolution of intermetallic particles in aluminium alloy AA3104 can-body stock during homogenisation. The experiments conducted for this study have certain limitations associated with it. Firstly, image analysis was conducted on easily available ImageJ and MATLAB software but advanced software would have taken less time and analysed the micrographs in more detail. Secondly, time is a factor when conducting experiments for this study. Image analysis requires approximately 200 micrographs and particle extraction takes more than 12 hrs to complete. Lastly, particle extraction depends on temperature and an inert gas, Ar, which makes the experiment very sensitive to the environment. Thus, if the experiment is contaminated, the extraction reaction will not occur.

1.5 Plan of development

This report begins with a literature review, which highlights previous work done on alloy AA3104 by other authors. It then focuses on experimental procedures performed on the alloy to obtain the desirable results for this research. After that the results of experimentation are recorded and discussed to outline how the evolution of intermetallic particle of AA3104 can-body stock occurs during homogenisation treatments. Conclusions are then drawn based on the results and discussion. Finally, recommendations are made, based on these conclusions.

2 LITERATURE REVIEW

2.1 Material

2.1.1 Pure aluminium

Aluminium (Al) is an element found in the earth's crust known as bauxite (typically $Al_2O_3.2H_2O$). Bauxite contains Fe_2O_3, SiO_2, and other impurities. The pure aluminium is refined (removal of impurities) from bauxite using the Bayer process [3]. Al in its highest form is soft, light weight and ductile. It is the second-most used metal (after iron) as it can be alloyed with almost any other metal to create materials with a whole range of useful properties [4]. Pure Al is a silvery-white metal with many desirable characteristics. The metal is non-toxic, non-magnetic and non-sparking. It has a high corrosion resistance and is highly decorative. .

Table 2.1 shows Al properties before it is treated or alloyed with other elements. The table shows that pure Al is light and has poor strength properties compared to Al alloy.

Table 2.1: Properties of Aluminium [5].

Properties	**Value**
Tensile strength (MPa)	90
Density (g/m^3)	2.6898
Elastic modulus (GPa)	68.3
Melting point (°C)	660.2
Crystal structure	Face-centred cubic (FCC)
Co-efficient of linear expansion (0-100°C) (x 10^{-6}/°C)	23.5

The metal can be modified and altered to greater strength for commercial uses by adding alloying elements. After alloying elements have been added it is possible for the metal tensile strength to increase to over 690 MPa [5]. Table 2.2 shows different Al alloying series with their main alloying elements. These series are categorised according to major alloying element(s) contained in the alloy. Further strengthening is possible by means which classify the alloys roughly into two categories, heat-treatable and non-heat-treatable. These Al alloys are used for many applications and one of them is beverage can production, where Al 5xxx series is used for the beverage can lid and Al 3xxx series for the can-body stock.

Table 2.2: Designations from wrought aluminium alloys [6]

Aluminium alloying series	**Major alloying elements**
1XXX	None (99% + Aluminium)
2XXX	Copper (Cu)
3XXX	Manganese (Mn)
4XXX	Silicon (Si)
5XXX	Magnesium (Mg)
6XXX	Magnesium (Mg) + Silicon (Si)
7XXX	Zinc (Zn)
8XXX	Lithium (Li)/other

2.1.2 Aluminium alloy AA3104

The 3XXX Al series has Mn as the major alloying element and is generally non-heat-treatable. The non-heat-treatable Al series are then strengthened using the temper designations seen in Table 2.3. Furthher strengthening of 3XXX series is possible by various degrees of cold working (strain hardening), denoted by H series of tempers. AA3104-H19 belongs to the Al 3xxx series, where H19 denotes that the material was cold rolled to this temper and it is harder than other denotations [7]. This series has a typical ultimate tensile strength range of 110-283 MPa which is higher compared to pure Al [8].

Table 2.3: The basic Aluminium temper designations [9]

Letter	Meaning
F	As fabricated – Applies to products of a forming process in which no special control over thermal or strain hardening conditions is employed
O	Annealed – Applies to product which has been heated to produce the lowest strength condition to improve ductility and dimensional stability
H	Strain Hardened – Applies to products which are strengthened through cold-working. The strain hardening may be followed by supplementary thermal treatment, which produces some reduction in strength. The “H” is always followed by two or more digits
W	Solution Heat-Treated – An unstable temper applicable only to alloys which age spontaneously at room temperature after solution heat-treatment
T	Thermally Treated - To produce stable tempers other than F, O, or H. Applies to product which has been heat-treated, sometimes with supplementary strain-hardening, to produce a stable temper. The “T” is always followed by one or more digits

AA3XXX series applications include building (especially architectural sheet), home appliances and other packaging. These alloys are frequently used for their good combination of strength and formability, weldability, anodising behaviour (for building applications) and corrosion performance. They are also used for heating equipment, such as brazing sheet and heating tubes because they perform well with their relatively high thermal conductivity combined with medium strength and good corrosion resistance [10].

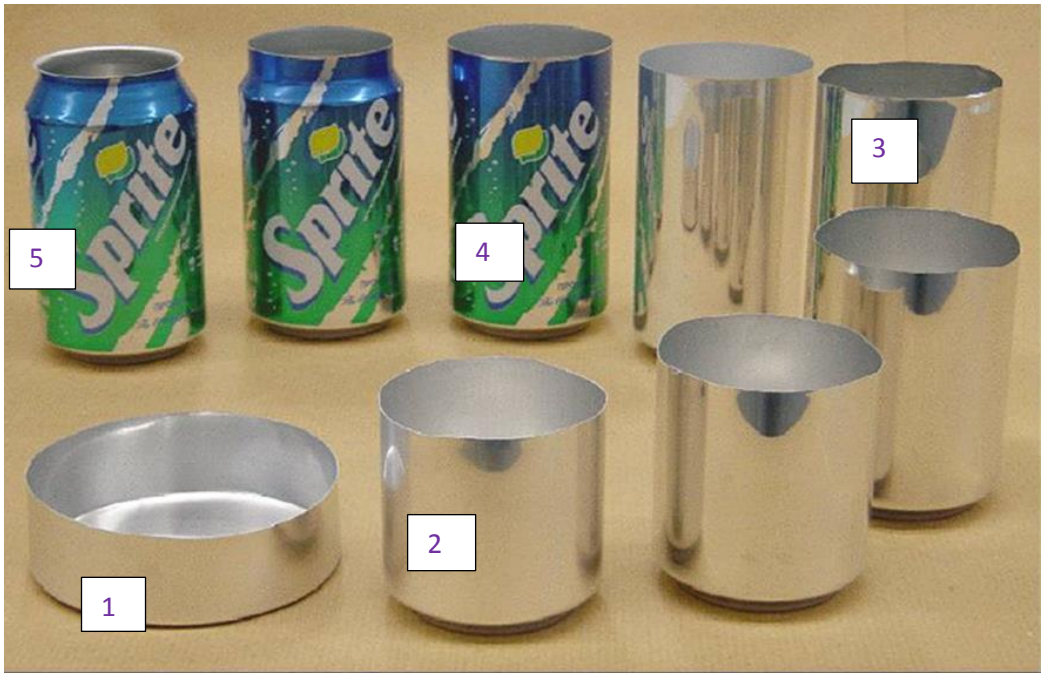

Figure 2.1: The sequence of can-body production from circular blanks by deep drawing, re-drawing and wall ironing [11].

Figure 2.1 shows the sequence of the making of a beverage can-body. This is one of the major applications for 3XXX series due to the alloys' good formability by pressing, roll forming and drawing. As per Figure 2.1, the beverage can-body making process involves: (1) firstly punching a cup from an aluminium sheet. (2) The punched cup is then drawn and redrawn to make it thinner and taller. (3) After that the beverage can walls are ironed to make the beverage can taller and thinner, creating a perfect mirror finish. (4) The beverage can is then decorated for consumer attraction. (5) Finally, the beverage can top is squeezed slightly to form a neck, with an outward flange at the top edge, which is folded over after the beverage can is filled. The success of these processes depends on final gauge sheet.

The basic alloy for can-making is the Al-Mg-Mn non-heat treatable groups, mainly because of the properties mentioned above. Alloys AA3004 and its modification AA3104 are principals for can-body stock (CBS) of drawn and ironed beverage cans. Table 2.4 shows alloying elements and amounts contained in AA3104. While Table 2.5 shows how these alloying elements contribute to the properties of the metal necessary for successful final sheet gauge production used in CBS production. For example, Mn, Si and Fe promote the formability of the alloy necessary for beverage can drawing. Cr, V and Zr increase the thermal stability of the alloy. Furthermore, Mg, Mn and Cu improve the strength of the alloy through solid solution strengthening.

Table 2.4: Aluminium AA3104 Composition.

Element	Al	Cu	Ga	Fe	Mg	Mn	Si	Ti	V	Zn	Other
Wt%	95.0-98.4	0.05-0.25	≤0.05	≤0.80	0.80-1.30	0.80-1.40	≤0.60	≤0.10	≤0.05	≤0.25	≤0.15

Table 2.5: Alloying elements that affect the properties of AA3104 [12].

Alloying elements	Metal properties
Mg	Improves the alloy's Strength through solid solution hardening and work hardening [13]
Cu	Improves the alloy's Strength by solid solution strengthening [13 and 14]
Mn	Improves the alloy's Strength by solid solution strengthening Mn diffusion determines the rate of phase transformation which promotes Good Formability. Also promotes Low and Consistent Earing
Si	Increasing Si content influences phase transformation during homogenisation which promotes Good Formability
Fe	Significant effect on the number of particles formed in the microstructure during casting and homogenisation promoting Good Formability
Cr, V and Zr	Increases the alloy's thermal stability [13]

Figure 2.2 shows a graph comparing pure Al and AA3104 CBS stress vs strain curves which shows how strain hardening in Al alloys can improve the metal's properties. CBS has a steeper and higher yield strength compared to pure Al as seen on the graph. This shows that CBS is stronger compared to pure Al, which then emphasises the desirable mechanical properties of strength and formability of the material [14]. As a result, they are among the most used individual alloys in the aluminium system, in excess of 1.6 billion kg per year [5]. This project focuses on AA3104 because AA3104-H19 temper sheets are used for Aluminium CBS production. The sheet production involves processing that alters the material's microstructure, thus altering properties. Therefore, the characteristics and processing of this material needs careful understanding for successful CBS production explained in section 2.2.

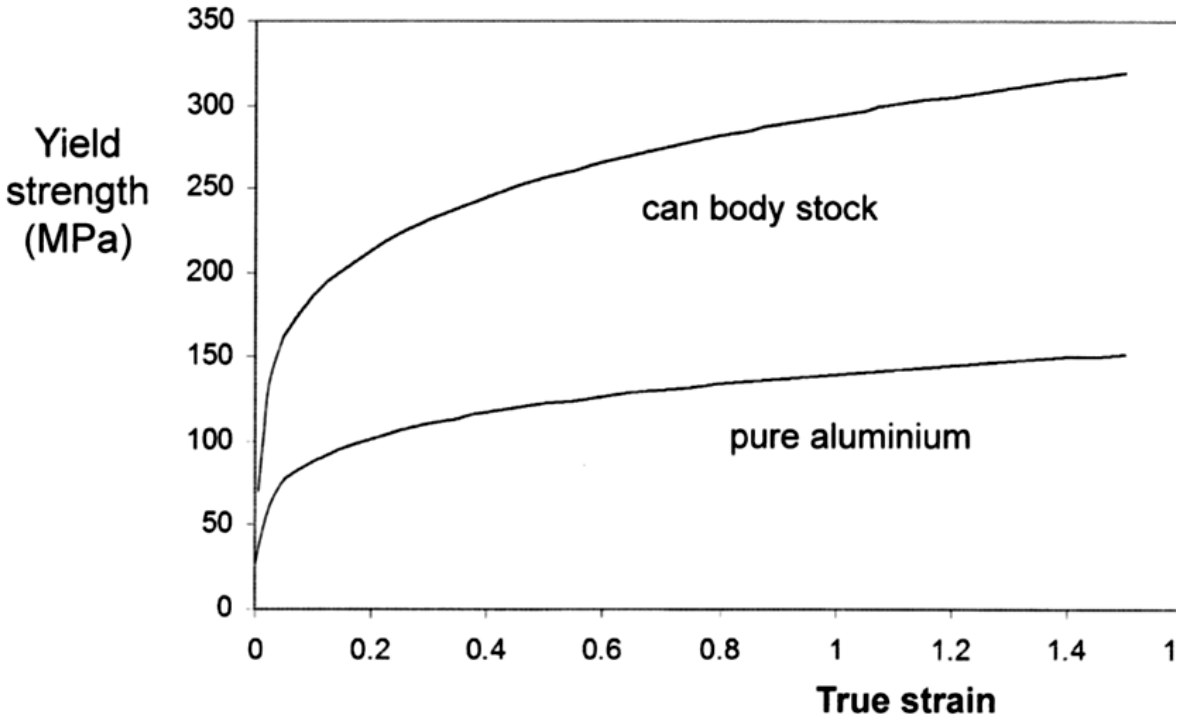

Figure 2.2: Graph showing effects of strain on yield strength of pure Al and can-body stock [15].

2.2 Industrial can-body sheet and can making process

2.2.1 Industrial can-body sheet making processes

Industrial can-body sheet production involves a number of thermo-mechanical processes (TMP) that need careful attention as they all affect the final gauge sheet quality. Below isFigure 2.3. showing the full process stream for a can-body sheet production. Firstly, AA3104 alloying elements are put in a decoater induction furnace, a melting furnace and then in-line treatment until a direct chill (DC) cast ingot is produced. The ingot is then scalped to remove surface defects and then homogenised to ensure that there is phase transformation and that the alloy components are uniformly distributed through the microstructure. After that the ingot is processed into sheets. The processes involve hot rolling, annealing, quenching, cold rolling and coiling sheets [16]. In hot rolling, the ingot is subjected to breakdown hot rolling in a number of passes using reversing or non-reversing mill stands, which serve to reduce the thickness of the ingot. Then the ingot is supplied to a tandem mill for cold rolling at 350°C. After that the cold rolled material is heat treated for particle recrystallisation by intermediate annealing. The rolled and heat treated sheet stock is coiled, air cooled and stored.

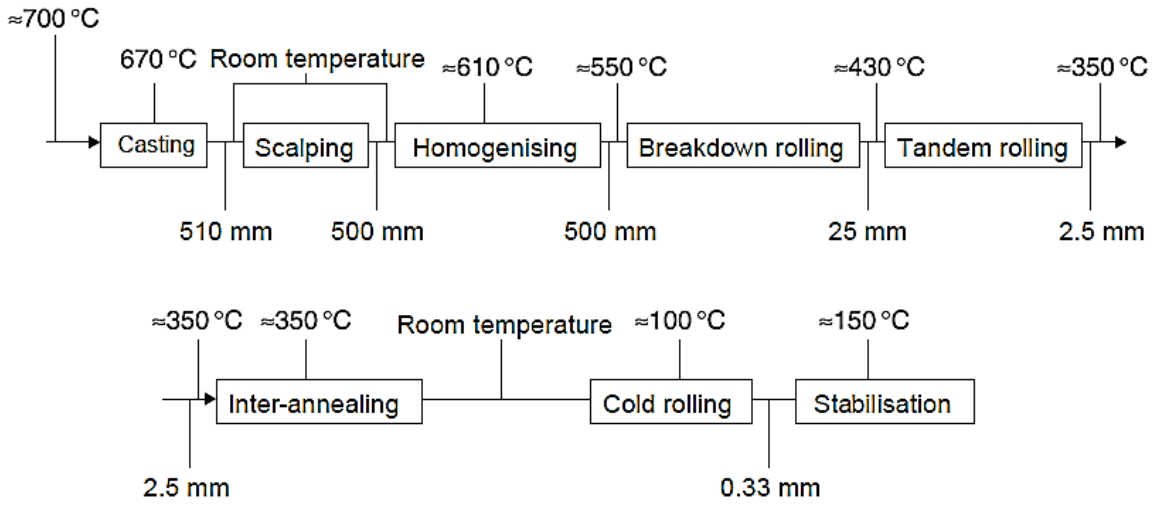

Figure 2.3: Typical process route for can-body stock [17].

The coil is then annealed in a batch step. The coiled sheet is then further reduced to final gauge by cold rolling using un-winders and re-winders and single and/or tandem rolling mills [16]. Lastly, the final gauge sheet is carefully packaged to seal against moisture intrusions and then shipped long distances to can-making customers. It is important to note that careful processing of AA3104 is necessary because it determines the microstructure of the alloy. The microstructural evolution of AA3104 during TMP is crucial for the development of high quality sheet for can deep drawing and wall ironing processes while manufacturing beverage cans.

2.2.2 Industrial can making process

An effective can-making process consists of high strength sheet for manufacturing and filling, good formability which includes a high quality surface finish, low and consistent earing (Figure 2.7), as well as essential galling resistance in section 2.2.3. Successful CBS production entails a high quality final gauge sheet. Figure 2.4 below shows the can-body making process whereby a blank sheet metal is firstly drawn by circular blanks into a cup. The cups are then redrawn using a blank holder and a steeped punch to elongate the initial cup. Lastly, the redrawn-cup wall is ironed using ironing dies, which makes the wall thinner and the beverage can longer. It is said that the as-cast ingot microstructure and subsequent homogenisation treatment impact some of the key drawn and iron sheet quality parameters such as earing, tear-off (Figure 2.6) and pinhole frequency, and galling resistance [18 - 20]. This research focuses on improving galling resistance. Therefore, metallurgical evaluation during these processes is essential for consistent can-body stock production [19].

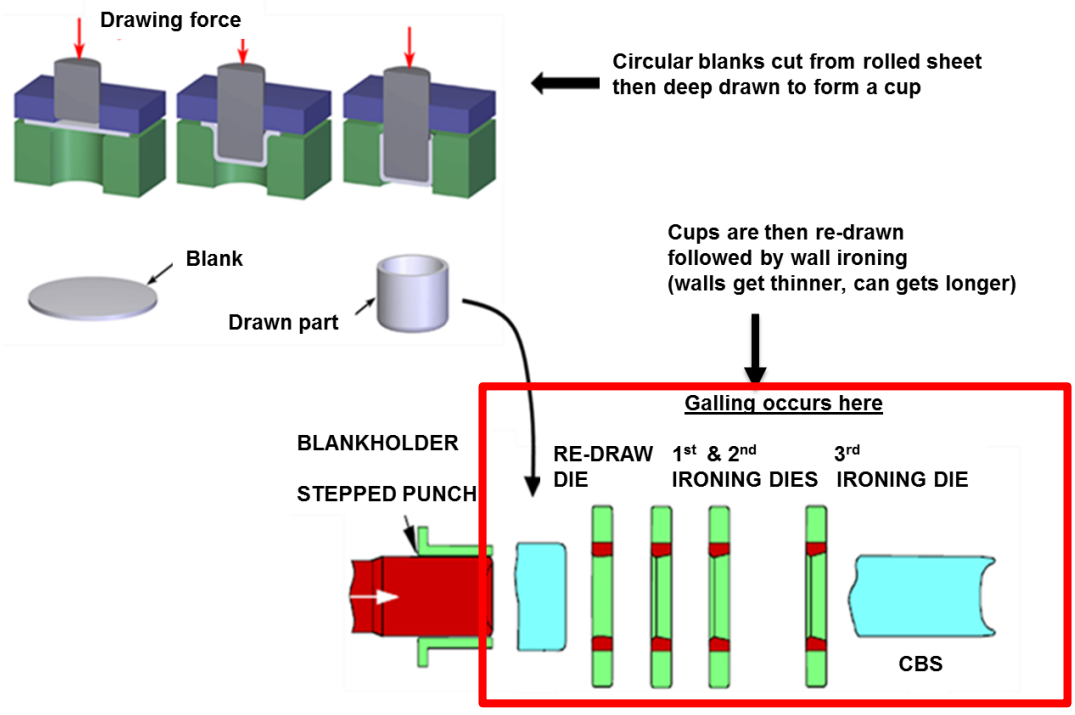

Figure 2.4: Industrial can-body stock making process [15].

2.2.3 Galling resistance

Galling (also known as scoring), in beverage can production, is an accumulation of aluminium and aluminium oxide pick-up on ironing tool-pieces, which results in scoring of can bodies degrading their strength and surface finish [21]. This manufacturing problem occurs during can re-drawing and wall ironing as indicated in Figure 2.4, whereby the sheet metal is not strong enough to clean the dies during processing, thus metal sticks on to the dies.

Galling problems have been observed on gauge sheet produced by certain strip-casting processes with high solidification rate, which produce a small intermetallic particle size. This indicates that a certain particle size is needed for the dies. Kamat reviewed that intermetallic particles are broken during hot and cold rolling (25%) [19]. The particles are further broken during can-making's successive ironing of the metal (up to 65% sheet-thickness reduction), which results in particles becoming smaller, thus reducing their effectiveness in cleaning dies. Other variables such as lubrication type (e.g. Post-lube, cupping lube, and body maker lube) and quantity, sheet surface roughness and tooling (e.g. ironing-die entry angle) may also influence galling during the body making process which makes it difficult to clearly define the minimum size of particles for preventing galling [19]. Furthermore, the large intermetallic particles are of value in preventing galling only at the surface of the material [12 and 14].

The exact significance of the transformation of β-Al_6(Fe,Mn) to α-Al_{15}(Fe,Mn)$_3Si_2$ is not completely understood, although an increased level of α-Al_{15}(Fe,Mn)$_3Si_2$ has been reported to improve the drawing and ironing behaviour in can-making [15, 19 and 20]. α-Al_{15}(Fe,Mn)$_3Si_2$ phase particles are harder than β-Al_6(Fe,Mn) phase particles which reduces galling, this is owing to the fact that they are sufficiently harder and act to abrade the tool-pieces hence removing metal pick-up [21]. Therefore, it can be concluded that galling resistance is improved through particle size and distribution as well as phase transformation of orthorhombic β-Al_6(Fe,Mn) phase (Vickers micro-hardness of 700-750 Hv) to a harder cubic α-Al_{15}(Fe,Mn)$_3Si_2$ phase which has hardness of 900-950 Hv [15, 18 and 22].

Figure 2.5 shows an example of the effect of metal build-up caused by galling during CBS processing, the metal build-up occurs due to an unclean die, which produces a degraded surface finish. Improving galling resistance requires 1-3% of intermetallic particles by total volume fraction, of which approximately 50% should be the harder α-phase [15]. It is important to control the intermetallic particles volume fraction so as to prevent poor galling resistance and too much galling resistance. A volume fraction >3% is not required as it causes tool wearing "tear offs" on the CBS, as shown in Figure 2.6. This is because the sheet would contain too many harder particles, thus making it difficult to obtain a very thin beverage can wall.

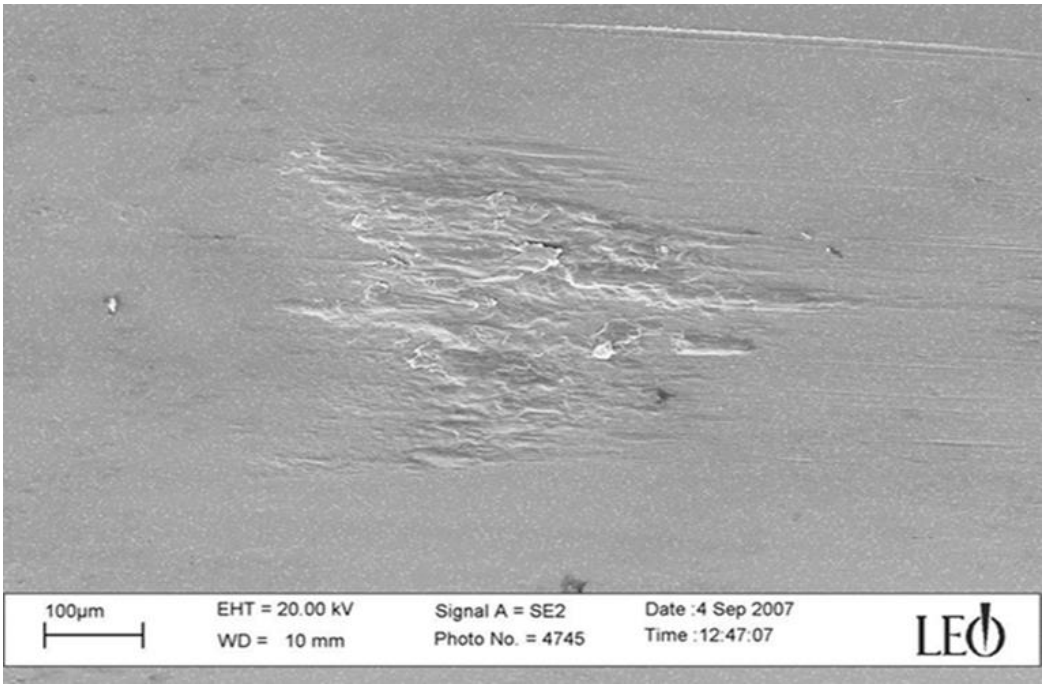

Figure 2.5: Metal build-up on tooling surface caused by galling [15].

Figure 2.6: Tool wearing on can-body caused by too much galling resistance [15].

2.2.4 Particle stimulated nucleation

It is well established that particles, through particle-stimulated nucleation (PSN), can affect the recrystallisation microstructure and texture of materials. PSN is a mechanism whereby deformation zones that occur at particles act as nucleation sites for recrystallization because they have a high dislocation density and fine sub-grains. This also means that the spatial distribution of resulting orientations can also be affected. In AA3XXX alloys, large Al-Fe-Mn-Si second phase particles promote recrystallisation by stimulating nucleation after hot rolling. Particle size distribution from homogenisation treatment, deformation rate, reduction and hot rolling temperature all act to control the critical size and number of particles that act as nucleation sites for recrystallisation.

PSN resulting from a low number fraction of large (>5μm) particles can counteract the effects of Zener drag during intermediate annealing (IA). Sufficient efficient PSN is needed to prevent "runaway growth" of a single or just few orientations such that a coarse-grained microstructure (resulting from IA) is avoided. This is important because "runaway growth" results in a microstructure consisting of coarse, elongated grains which appear to promote texture banding in Al alloys.

The IA step achieves the requisite balance between recrystallisation texture and deformation texture to minimise earing. Annealing results in crystallographic texture of the recrystallisation type (cube, goss) which develops four ears at 0°, 90°, 270° and 360°. Earing occurs when there is anisotropy in the mechanical properties within the beverage can-body. The ears are then cut off, thus leading to wastage [23]. A balanced texture of strong cube and random gives a tendency of 0/90° and 45° earing respectively. This gives little or no earing tendency on the final sheet product [24]. As can be seen in Figure 2.7, these two types of ears are positioned to fill each other's valleys. Thus, the intermediate anneal recrystallisation texture balances the cold rolling texture to give an overall reduced earing percentage (Figure 2.7a) [14]. The reduction of earing percentage results in improved metal yield and productivity during drawing and ironing in the beverage can-making process [14].

In addition, the number of constituents/particles formed has an effect on hot rolling due to particle stimulated nucleation (PSN). Furthermore, Gandhi suggests that the number of constituent particles that form due to Fe addition will have a direct impact on the recrystallization kinetics and the texture which forms in hot rolled sheets as PSN becomes more dominant [18]. The critical size and number of particles that act as nucleation sites for recrystallisation are dependent upon the hot-rolling temperature, reduction, rate of deformation, and the particle size distribution from the homogenisation treatment [25]. Therefore, the evolution of intermetallic particles/precipitates during homogenisation plays a crucial role during beverage can-making.

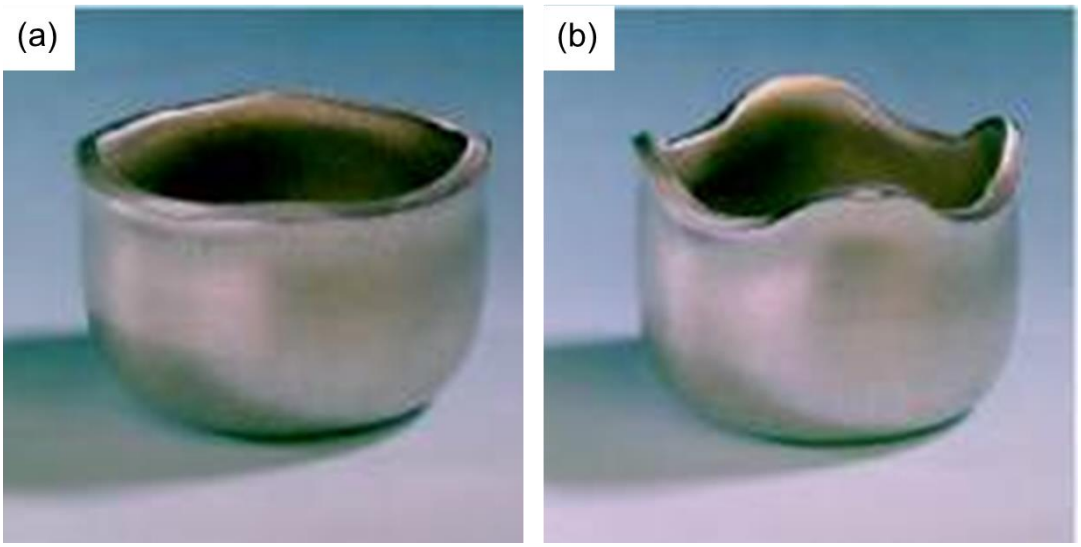

Figure 2.7: Aluminium punched beverage can showing (a) low and consistent, (b) high and inconsistent earing [23].

2.3 As-cast microstructure

During solidification of AA3XXX, a microstructure is formed that consists of a cellular dendritic Al matrix containing intermetallic particle phases along the grain and cell boundaries which are remnants of the last highly segregated melt to freeze [18]. The cast microstructure shows an initial cast structure which influences the size and distribution of particles in the final gauge sheet. This cast structure helps define the evolution of the alloy microstructure after homogenisation. Casting conditions determine growth velocities and composition in various regions of the ingot. These conditions then control important features defining cast structures. These features are: grain and intermetallic particle size, type and distribution of the intermetallic particles, as well as the eutectic element micro-segregation (i.e. Mg, Si, Cu and

to a lesser extent Mn in segregation order) [18, 19, 20 and 22] Elemental segregation during solidification occurs for the first few centimetres from the edge and at the centre of the ingot.

The as-cast AA3104 microstructure shows evidence of segregation occurring on scales of micro-segregation and macro-segregation. Micro-segregation occurs by chemical non-uniformity when pure Al solidifies early causing different scales of dendritic arm spacing (DAS), rejecting alloying elements. The DAS decreases with increasing cooling rate. Coarsening of DAS also occurs during solidification and thicker branches survive. Whereas, macro-segregation occurs on a larger scale due to movement of liquid or solid as solidification rate decreases from the ingot outer periphery toward the centre of the ingot [19]. However, modern casting treatments have largely eliminated macro-segregation in AA3104 can-body stock, therefore this feature is not of concern.

Residual liquid between two solid surfaces in the final stages of solidification are enriched in solute elements and may thermodynamically favour the formation of comparatively enriched intermetallic phases. The observation/suggestion results from the intermetallics located at the grain and cell boundaries due to the solute elements such as Fe and Si segregating in to the liquid at solid/liquid interface during non-equilibrium solidification of Al alloys [26]. Fe and Si have low solid solubility in Al, resulting in them forming various insoluble secondary intermetallic phases on solidification.

The chemical composition and solidification conditions influence the variation of the intermetallic particles' type, size and shape within Al alloys [27]. Figure 2.8 shows the particles present within the AA3104 as-cast microstructure. The microstructure consists of intermetallic particles with different phases at the grain boundary. The orthorhombic β-Al_6(Fe,Mn) phase is the primary phase at approximately 85% of the particles. These predominant long lath-shaped Al_6(Fe,Mn) intermetallic particles grow parallel to the solidification direction. Traces of the cubic α-Al_x(Fe,Mn)$_3Si_2$ is also seen as the remainder phase at cooling rates of about 1°C/s. However, the relative amounts of these phases are determined by the alloying composition as well as the solidification rate [18].

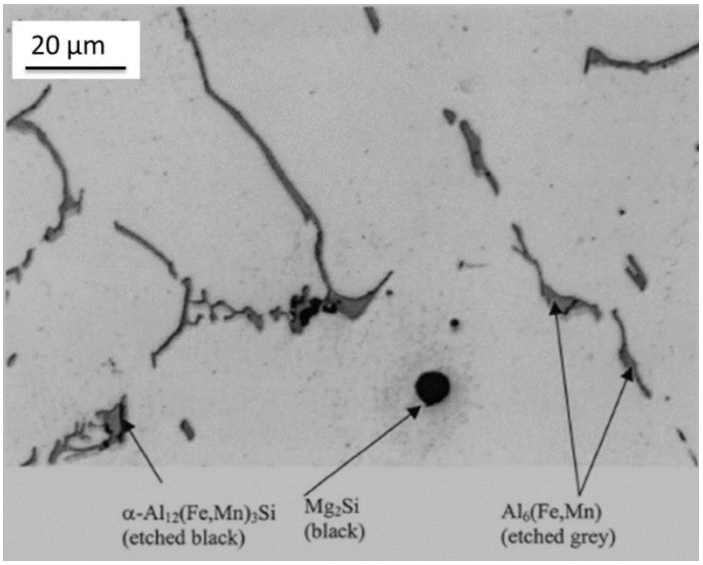

Figure 2.8: Light micrograph of as-cast microstructure showing various intermetallic particles [18].

During ingot solidification, the freezing rate decreases from the edge to the centre resulting in variation in the morphological features at different ingot locations. Generally, high solidification rates do not promote the development of the α-phase in the as-cast condition [14]. The as-cast microstructure obtained after solidification consists of an Al matrix, dispersoids within the Al matrix and intermetallic particles at the grain and cell boundaries. Figure 2.9 (a) shows that microstructure near the ingot edge has a higher proportion of finer particles, whereas Figure 2.9 (b) has a fewer proportion of coarser particles at the centre. Figure 2.9 (a) and (b) is explained by the fact that the dendritic cell size decreases while the particles become finer (thinner) as the freezing rate increases during ingot casting [18]. Kamat observed a significant particle size difference between the edge and centre of as-cast microstructures [19]. It was observed that particles at the edge appear as narrow and thin platelets compared to the centre particles that are two to three times larger on average and are block-like in shape [19]. This is because of the faster heat extraction from three surfaces (one narrow and the two wide faces) at the edge compared to the two wide faces only at the centre.

Additionally, the grain size increases from the edge towards the centre due to the decrease in the cooling rate. Observations made by Kamat shows that average as-cast particle area % was estimated to be 2.88±0.36 at the edge and 2.42±0.29 at the centre [19]. The understanding of as-cast solidification is important because the formed size and shape of the intermetallic particles in the ingot is observed to influence the size and distribution of intermetallic particles in the final gauge sheet.

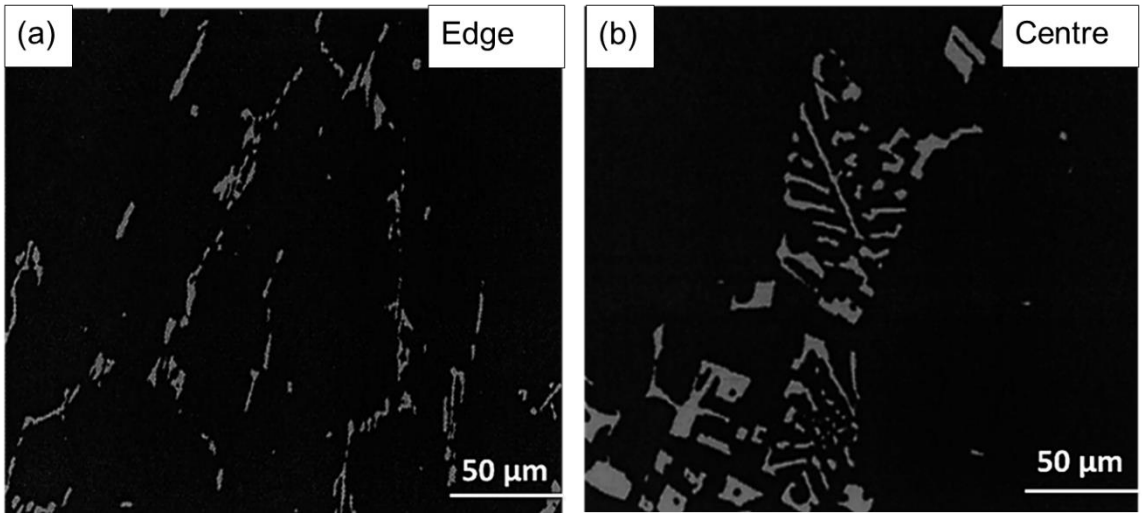

Figure 2.9: Micrographs showing size and shape of particles in as-cast ingot (a) near the edge and (b) at the centre [18].

Two-dimensional analysis by optical microscopy shows intermetallic particles as either Chinese script or needle-like, as well as fine and discrete. Whereas, three-dimensional analysis shows that the particles are petal and comb-like or dendritic, as well as coarse and well interconnected. The interconnectivity suggests that the particles grow along the grain boundaries in the final stages of solidification and connect with each other [26]. This is observed on AA6063 Al alloy, however it is applicable to Al alloys bearing Fe intermetallic particles.

2.4 Homogenised microstructure

Homogenisation of the ingot significantly minimizes or possibly eliminates micro-segregation due to chemical uniformity, whereas macro-segregation is hardly altered [14 and 19]. Homogenisation of AA3XXX DC-cast ingot results in some microstructural changes. These changes include even distribution across grains and dendrites, as well as Mn in solid solution supplying growth of existing intermetallic particles. Alexander and Greer established that during homogenisation treatment of AA3XXX alloys, there is an initial transformation of $Al_6(Fe,Mn)$ into α-Al(Fe,Mn)Si phase as a result of an eutectoid transformation [14]. The transformation proceeds with possible particle spheroidisation and coarsening [22]. There is also a subsequent transformation of intracellular precipitation of dispersoids on the dislocation cells which are often identified as finer α-Al(Fe,Mn)Si [24 and 28].

Gandhi and Kamat suggested/concluded that the grain size plays an important role in the equilibration process of the alloying elements and the spatial arrangement of the precipitating dispersoids during homogenisation. Therefore, homogenisation occurs quickly at the edges mainly because the grains are finer, hence elements have a smaller distance to travel within the cells [18 and 19]. The secondary dendrite arm spacing (SDAS) increases with the distance from the edge to the centre due to a decrease in solidification rate. SDAS plays an important role during homogenisation of ingots, where the degree of homogenisation can be related to SDAS using a simple one-dimensional (1-D) diffusion approach. Different researchers report different forms of α-phase within this alloy, as seen in Table 2.6. The different α-phase forms are dependent on the alloy's composition and homogenisation temperature as well as time.

Table 2.6: Different α-phase forms found in AA3104 alloy.

α-phase form/type	Researcher(s)	Homogenisation condition	Fe + Si content (wt%)
α-Al(Fe,Mn)Si	[29]	580°C for 3 hrs	0.2Fe + 0.4Si
α-$Al_{12}(Fe,Mn)_3Si$	[14, 19, 18, 30 and 31]	550-610°C for 0-10 hrs	0.33-0.4Fe + 0.20-2.4Si
α-$Al_{15}(Fe,Mn)_3Si_2$	[15, 31 and 32]	600°C for 15 mins (partial transformation)	0.22-0.4Fe + 0.08-1.2Si

2.5 Phase transformation during homogenisation

It is confirmed that phase transformation from β-Al_6(Fe,Mn) to α preferentially nucleates at the matrix grain boundaries. This nucleation theory suggests that the nucleation behaviour results from the ability of the boundaries to relieve volume changes associated with nucleation [33 and 34]. Figure 2.10 (a) and (b) shows a bright-field Transmission Electron Microscopy (BF TEM) image and a labelled schematic of a duplex particle in an Al-0.5wt%Fe-1.0wt%Mn-0.2wt%Si alloy heat-treated for 2 minutes at 500°C.

The partially transformed particle shows clear coincidence of the intergranular boundary with the transformed region of the particle as seen on both (a) and (b). Figure 2.10 (b) shows that the transformed regions within the heat-treated specimen are small relative to the particle size and that the transformation appears to have spread out from the grain boundaries. This indicates that transformation initiates at the grain boundaries, and then spreads along the particle-matrix interface to facilitate access to the silicon [34]. This is because grain boundaries are fast diffusion paths for Si supplying the transformation. The boundaries reduce the net surface energy needed to form a nucleus, thus accommodating the strain of nucleation. The function of these boundaries is to relieve stresses induced by the volume change associated with the initial transformation to α-phase from the β-Al_6(Fe,Mn) phase [34].

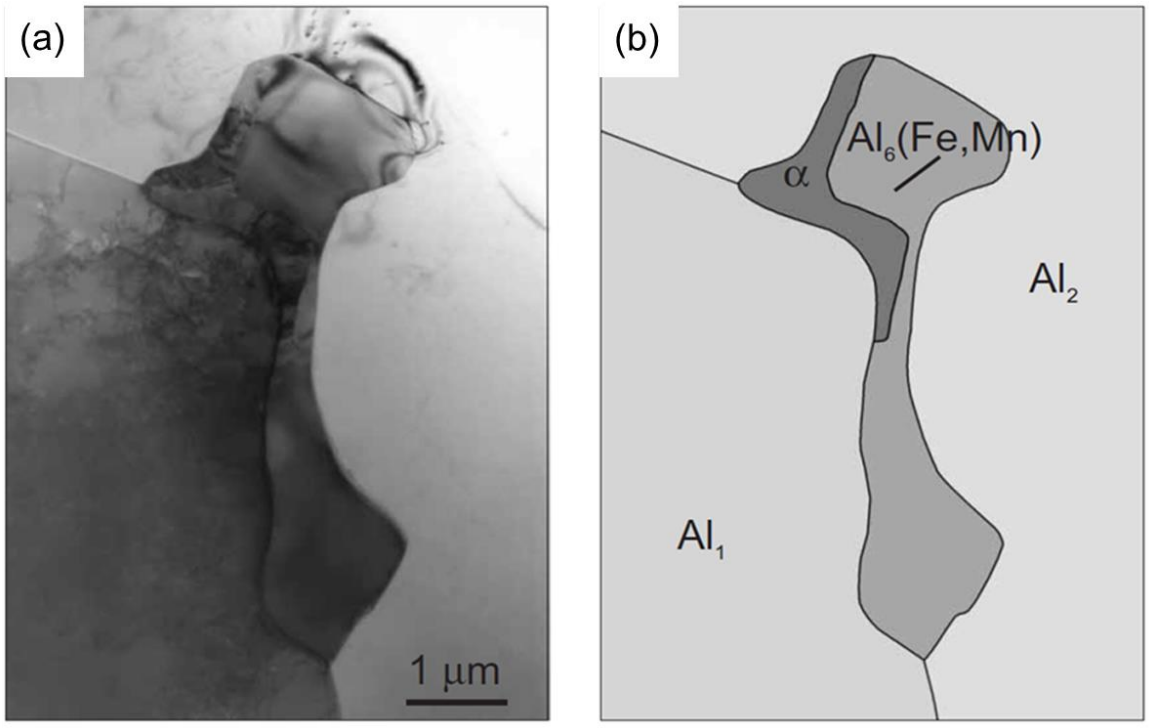

Figure 2.10: (a) BF TEM image of a duplex particle in an Al-0.5wt% Fe-1.0wt% Mn-0.2wt% Si alloy heat treated for 2 min at 500°C, (b) labelled schematic diagram [34].

Investigation of the Al-0.5wt%Fe-1.0wt%Mn-0.2wt%Si phase model shows that, the kinetics of a transformation of intermetallic particles within a homogenised DC ingot occurs through a eutectoid process [33]. Initial transformation involves a rapid diffusion of Si from the significantly Si supersaturated Al matrix. In DC-cast 3XXX alloys, the Al_6(Fe,Mn)-to-α transformation may nucleate at small incipient regions of α-phase in or on Al_6(Fe,Mn) particles. Alexander and Greer suggest that the Al_6(Fe,Mn) phase is consumed by a eutectoid intergrowth of α-phase and Al which has a fast growth rate [33 and 34]. Si diffusion drives the phase transformation as the Si diffuses from the matrix and Mg_2Si particles into the β-Al_6(Fe,Mn) phase particles. Therefore, though the eutectoid growth is fast, it is limited by the supply of Si. However, α-phase nucleation is mostly known as the overall rate-controlling factor [33 and 34].

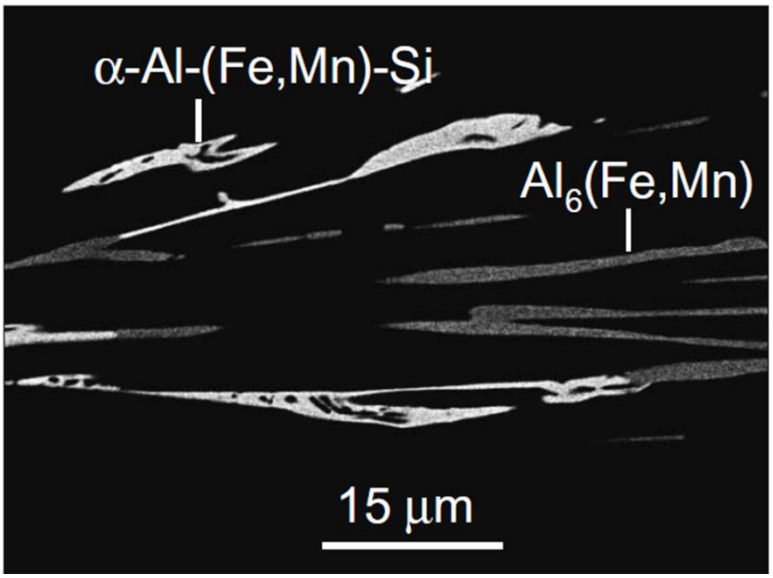

Figure 2.11: BE SEM image of a polished specimen made from an alloy heat-treated for 1 h at 500 °C [21].

In DC-cast alloys, the β- to α-phase transformation competes with the dispersoids, for the Si in the matrix solid solution, which precipitate within the Al grains. However, the dispersoids dissolve within processing time scales at high homogenisation temperatures (about 570°-600°C), causing particles to coarsen [33 and 34]. There is also a chance that particles are partially transformed. The partially transformed particles result from localised Si depletion. This is explained by the fact that the transformation is thermodynamically favourable when Si is present. Figure 2.11 shows an example of such a two-phase (duplex) particle, where the Al eutectoid has spread around most of the perimeter of the particle as well as penetrated to the particle centre. Alexander and Greer describe the Al spots within the α-phase particles as fingered appearance instead of spherical. This is explained by the fact that the specimen was

heat treated for 15 min at 600°C, which means that the particles are caught in the early stages of transformation, thus resulting in eutectoid intergrowth [33].

2.6 Compositional effect on both as-cast and homogenised microstructure

AA3104 contains a variety of alloying that influence the alloy's microstructure. Table 2.4 and Table 2.5 in Section 2.1.2 shows the chemical composition of AA33104 and how the alloying elements affect the properties of the alloy. The information on how the elements significantly affect the microstructure is explained thereafter.

2.6.1 Magnesium (Mg)

Mg, along with Cu, influences the freezing rate during AA3104 solidification. This then influences the formation of the surface segregated layer in the as-cast condition [12]. Al-Mn alloys containing Mg consists of a precipitate of Mg_2Si which precipitates during heating at industrial heat-up rates. These precipitates are aligned with their habit plane along $<100>_{Al}$ in the Al matrix. During higher homogenisation temperature, the α-Al(Fe,Mn)Si particles nucleate on the pre precipitated Mg_2Si which lead to the dissolution of this Mg_2Si phase. In line with the review by Li *et al.*, Kamat *et al.* also studied the precipitation of α-Al(Fe,Mn)Si phase in a hot rolled 3004 alloy during annealing and found that the α-precipitates can also nucleate on the primary Al_6(Fe,Mn) particles [25 and 35].

2.6.2 Manganese (Mn)

During solidification, 25-30% Mn precipitates out of solid solution in the form of intermetallic particles, while the rest of the Mn (~70-75%) remains in solid solution. Mn precipitation during homogenisation depends on the Fe- and Si-contents within the alloy [36]. Thus, an as-cast microstructure in a supersaturated metastable solid solution condition is produced [18]. The Mn in supersaturated solid solution decomposes by the precipitation of particles during heat treatment. Mn is a slow diffusing element in Al, which interferes with recrystallisation [14].

Generally, Mn retained in solid solution hinders recrystallization kinetics during annealing after hot rolling, which makes this condition undesirable from ingot casting. However, it is favourable in can-body stock as it provides large, hard particles for die cleaning and to impart some strength to the final gauge through solution hardening. If Mn exceeds the upper limit, too many dispersoids are formed during the rolling of the cast strip. This prevents adequate recrystallisation during annealing which results in problems occasioned by earing [12]. Mn in solid solution is also favourable because it has a stronger effect on the electrical conductivity than any other element in CBS [18].

The variation in composition of both phases [i.e. Al_6(Fe,Mn) and α-Al(Fe,Mn)Si of the primary particle] at higher temperatures is controlled by long range diffusion of Mn. This implies that the electrical resistivity variation is principally associated with the evolution of the primary precipitates composition and the further eutectoid transformation [37]. The evolution of electrical conductivity is used to estimate the concentration of Mn in solid solution. This provides an indication of supersaturated solid solution decomposition. It is seen that Mn solid solution continues to decompose from 300-530°C as electrical conductivity increases. Furthermore, the decrease in electrical conductivity after 530°C is due to the increase of Mn solubility in the matrix, thus dissolving dispersoids into the matrix.

The presence of Mn exceeding the maximum required content results in too many particles which cause earing in the final product [12]. Due to faster cooling rates at the ingot edge, the edge shows a higher amount of Mn in solid solution compared to the ingot centre [19]. This partially explains why the edge has a higher degree of homogenisation.

Mn also makes the alloy ductile; while in combination with iron it improves the castability of the alloy and reduces shrinkage during metal solidification. Up to 2wt%, Mn fine precipitates (dispersoids) also stabilise grain size during high annealing temperature which improves strength and formability. However, Mn is less effective than copper or magnesium. In some of the 3XXX alloys, the strengthening effect of added Mn is supplemented by additions of magnesium which offers further solid solution strengthening.

2.6.3 Copper (Cu)

Cu, like Fe, promotes Mn precipitation in Al alloys, however it has a milder effect than Fe [18]. The Cu contained in the alloy also strongly affects the alloy's corrosion resistance. Mg and Cu are the main solid solution strengthening elements in Al CBS [18]. Cu with Mg also contributes to the freezing rate and controls the surface segregation zone during solidification of the alloy [12].

2.6.4 Iron (Fe)

Fe is a major impurity element in Al alloys that influences detrimental secondary phase formation, which is frequently acquired at Fe levels of 0.4-0.8wt% from Al scrap during the recycling process. Any kind of Fe addition in 3XXX series alloys has a significant effect on the number of constituent particles in the microstructure thus controlling the volume fraction (VF) of intermetallic particles. Figure 2.12 below shows an example of microstructural change due to Fe content variation. It is seen that constituent particles increase as Fe content in alloy 3004 increases. The formation of intermetallic particles promotes Mn precipitation and prevents the formation of the ternary metastable phases ($Al_xMn_yFe_2$) that usually form in Al-Mn-Fe alloys. Instead of ternary precipitation phase appearing, Fe atoms substitute for Mn atoms in Al_6Mn.

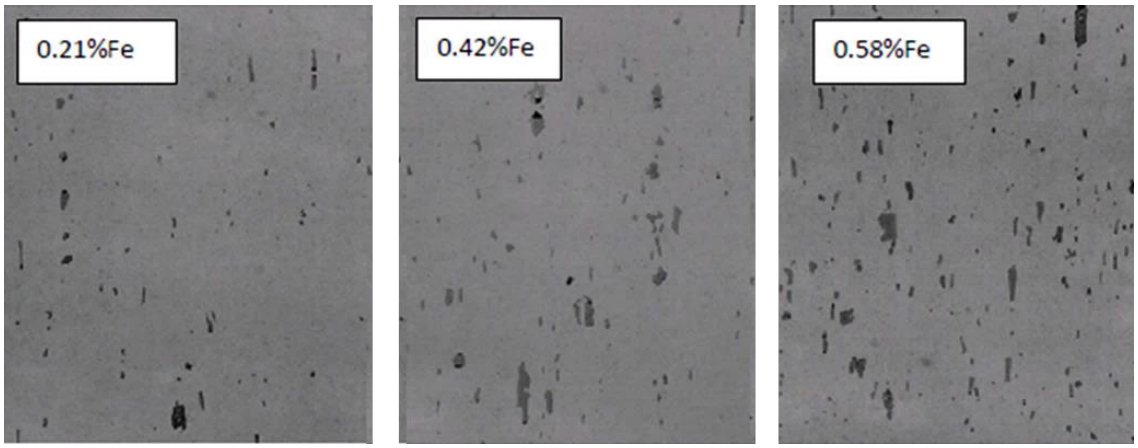

Figure 2.12: Images showing microstructure of AA3004 as Fe content increases [15].

Jin *et al.* states that it is preferred that the intermetallic particles have a size and shape characteristic of the Mn based particles because if Fe dominates the particles become finer and less desirable [12]. Therefore, the Mn to Fe ratio should preferably exceed 1.0 and most preferably exceed 2.0 [12]. Fe is also said to provide control of the cast grain structure [12]. During solidification, large Fe levels may lead to the formation of highly faceted plate-like Al_5FeSi intermetallic particles. However, Fe favours the precipitation of $Al_6(Fe,Mn)$ [35].

The addition of Fe and Si to AA3XXX alloy reduces the solubility of Mn in the Al matrix and speeds up the precipitation of Mn containing particles. Fe may substitute for Mn in both Al_6Mn and α-$Al_xMn_3Si_2$ phase. When the Mn/Fe ratio is high, α-$Al_x(Fe,Mn)_3Si_2$ phase has a cubic crystal structure. However, it changes to a body centred cubic structure when Fe content is higher. Furthermore, Fe is an alloying element giving a polishing effect in fast deep drawing/ironing operations [21].

2.6.5 Silicon (Si)

Silicon (Si) favours the precipitation of cubic α-phase, $Al_x(Fe,Mn)_3Si_2$ in the AA3104 alloy. Dehmas *et al.* observed and argued that β-phase to α-phase transformation occurs by Si diffusion [37], where the α-Al(Fe,Mn)Si phase inherits the Fe and Mn contents from the previous $Al_6(Fe,Mn)$. This means that the high diffusivity of Si allows the phase transformation of $Al_6(Fe,Mn)$ into α-Al(Fe,Mn)Si to occur [37]. The amount of Si present is believed to affect the number of α-phase particles formed. The desired amount of Si is 0.17-0.23wt%, which is necessary to provide increased phase transformation [14]. Si amount lower than 0.12% prevents the transformation to the α-phase [15]. Furthermore, high Si content gives a high fraction of α-phase particles but also high density of dispersoids such as $Al_{12}Mn_3Si$ and α-Al(Mn,Fe)Si [35]. Magnesium silicide (Mg_2Si) is believed to form if the Si exceeds 0.3% [13].

2.7 Parameters affecting microstructural changes during homogenisation

2.7.1 Si level content

During casting with sufficiently low heat flux, Si at less than 0.15wt% ensures that the principal intermetallic formed is the Al_6(Fe,Mn) phase, with only minor amounts of α- Al(Fe,Mn)Si phase present. If Si exceeds 0.15wt% the α-phase tends to dominate even at low cooling rates [12 and 35]. The amount of Si content available within the AA3104 alloy determines the degree of α-phase transformation achieved in the material during homogenisation. Whereby, if Si levels are less than 0.12% there is prevention of transformation. Whereas, if Si levels are greater than 0.4% then about 100% α-phase transformation is forced very quickly. Figure 2.13 shows the α-phase transformation measured in final gauge commercial CBS as a function of Si level, where 0.19wt%Si yields a desired α-phase particle percentage of 50% (In circle).

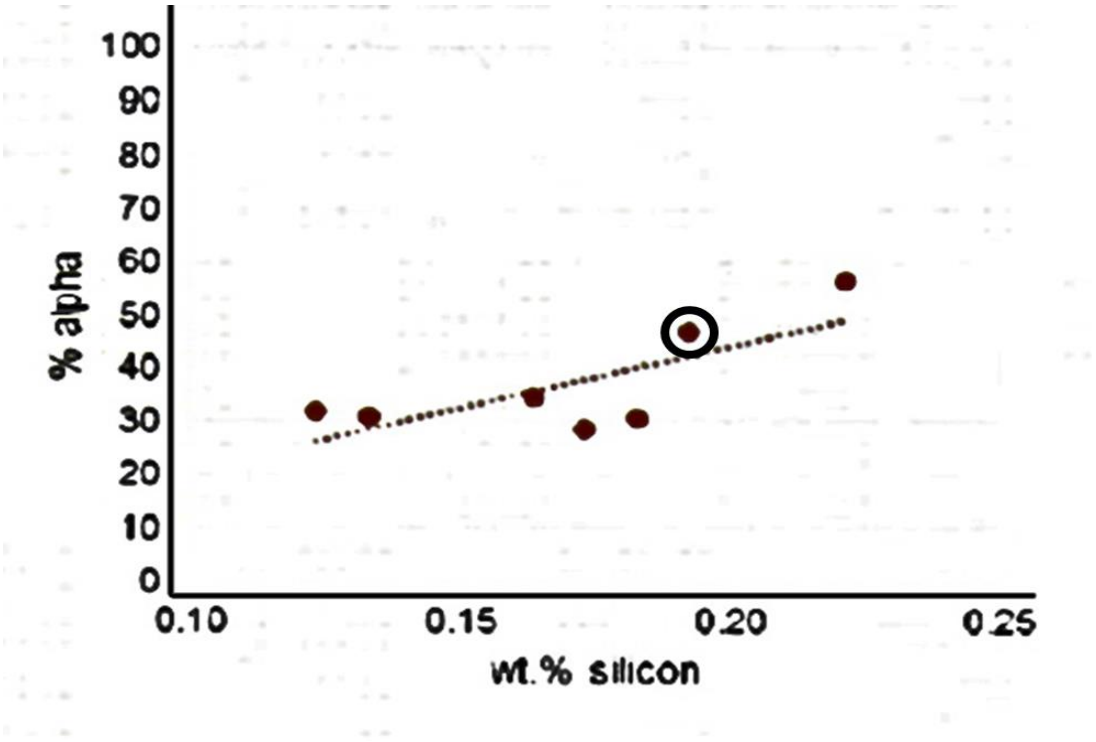

Figure 2.13: Showing α-phase transformation measured in final gauge commercial CBS as a function of Si level [15].

2.7.2 Heating and cooling rate

The heating up and cooling rate should not exceed 50°C per hour [15]. This is to allow the intermetallic particles and grains to grow, as well as stabilise.

2.7.3 Homogenisation temperature

There seems to be some confusion as to whether α% increases or decreases with the homogenisation temperature [15]. Figure 2.14 shows how the α-phase behaves with the change in homogenisation temperature. The graph indicates that α decreases at high homogenisation temperature (575→600→630°C), shown by the blue arrow, and decreases with temperature at lower temperature (575→450°C), shown by the green arrow. Hulamin and Technology Strategy Consultants used this information to recommend homogenisation temperatures that yield the desired β-to-α-phase ratio. Additionally, the average particle size increased as the homogenisation temperature increased. However, particle fragmentation during homogenisation treatment may be the cause of variation in particles size [24].

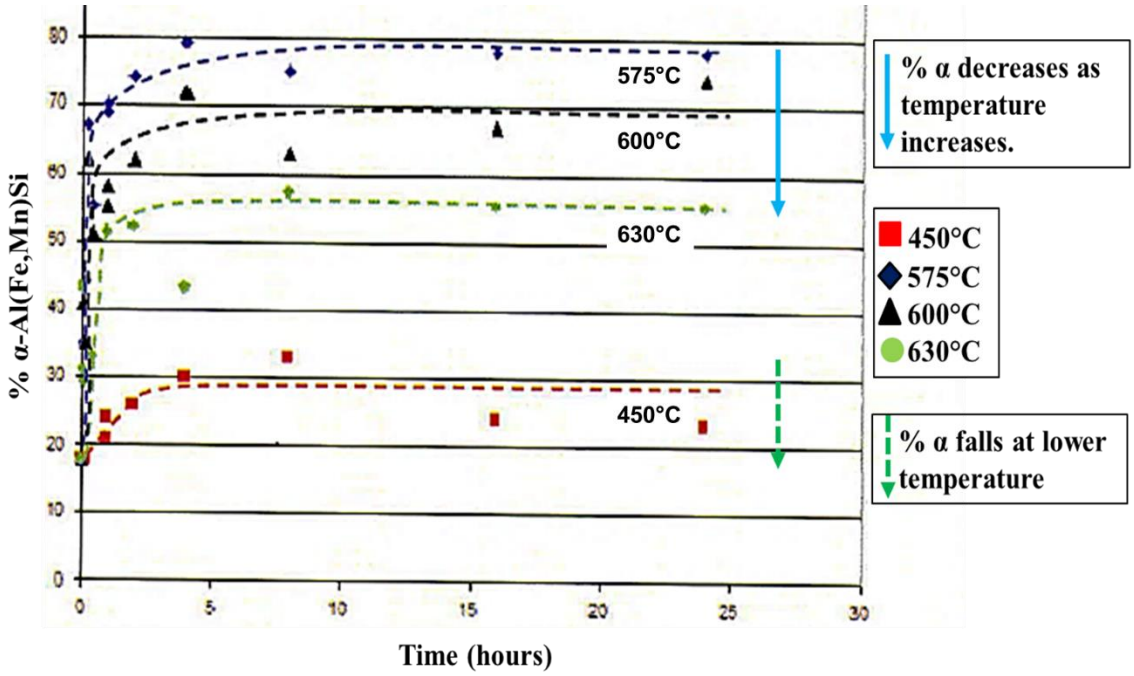

Figure 2.14: Graph predicting the behaviour of α-phase with change in homogenisation temperature [15].

2.7.4 Homogenisation time and soak time

Section 2.4 mentions that SDAS plays an important role during homogenisation of ingots, where the degree of homogenisation can be related to SDAS using a simple 1-D diffusion approach. Kamat reviewed that the necessary homogenisation time decreased with increasing temperature. Furthermore, homogenisation times for a given temperature decreases as SDAS decreases because alloying elements combine at a shorter diffusion distance. Therefore, the homogenisation times vary with SDAS such that a decrease in SDAS by one-half decreases the homogenisation times four-fold [19]. Increase in homogenisation time results in spheroidisation of “Al spots” and particles which lead to the lath-shaped particles breaking up [21]. Particle and dispersoid sizes also increases with soaking time during homogenisation.

2.7.5 Second stage soak

A typical homogenisation treatment for microstructural evolution in the ingot consists of a single soak stage. Researchers have investigated the merit of altering homogenisation cycles to include a second soak period at a lower temperature. Gandhi refers to a two-step homogenisation treatment that consists of heat-up, hold at high temperature (560°C-610°C) followed by control cooling to a lower temperature (450°C-500°C) and then soak at this temperature prior to hot rolling [18]. The difference between a microstructure obtained during one-stage and two-step homogenisation treatments is that the second stage treatment has lower Mn in solid solution. This occurs because during the second stage cool, Mn precipitation occurs in a controlled manner such that Mn wt% in solid solution is lower and at the same time the number of intermetallic particles is not increased [18]. Therefore, the reason for second stage soak is to promote Mn precipitation without increasing the number of particles. This homogenisation treatment generates a required particles structure required for galling resistance, to control recrystallisation during hot rolling and subsequent crystallographic texture after annealing.

2.8 Thermodynamic calculations

Many researchers have used thermodynamic calculations (modelling) pertaining to equilibrium conditions for valuable information that can be gained for practical applications. CALPHAD and JMatPro are multi-platform software programs that use thermodynamic high quality calculations of phase formations in numerous types of Al-alloys by incorporating various theoretical materials and properties database.

Saunders *et al.* observed an agreement between calculated results (using CALPHAD and JMatPro) and experimental results presented by a few authors [19, 20, 22, 38 and 39]. These results showed an agreement in particle phase evolution from as-cast through to homogenisation. Figure 2.15 shows the equilibrium phases in AA3104, whereby $Al_6(Fe,Mn)$ is the predominant phase formed during casting/solidification. Mg_2Si is said to form at an expense of α which is expected because of the strong affinity of Mg_2Si for Si during solidification however, it is not plotted in this graph. The α-phase then predominates during solution treatment with sufficient time over a significant temperature range. It is also important to note that the degree to which α predominates is sensitive to the alloy's composition, particularly to Si. Furthermore, Figure 2.14 correlate with Figure 2.15 where α-phase initially increases with temperature but decreases as temperature exceeds 600°C. Additional phases present that are not indicated in the graph are Al_3Mg_2, T_AlCuMgZn and S_Al_2CuMg [36]. This information shows/confirms the phases that are to be expected within alloy AA3104 in the as-cast condition and after homogenisation.

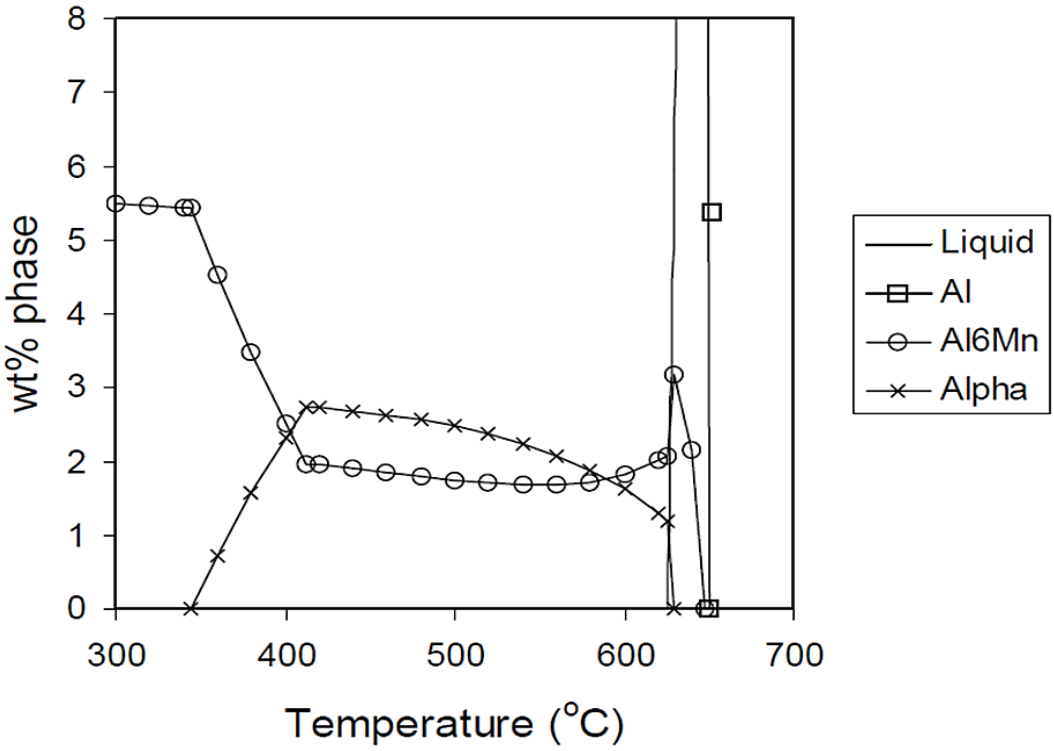

Figure 2.15: Calculated phase % vs. temperature plot for an AA3104 alloy [39].

2.9 Image analysis

Image analysis involves processing an image into fundamental components in order to extract statistical data. Image analysis can include such tasks as finding shapes, detecting edges, removing noise, counting objects, and measuring region and image properties of an object [40]. Few authors used the image analysis method to quantify intermetallic particles [33, 35, 37 and 41 - 45]. However, information on the image analysis method and the amount of intermetallic particles it yields is not well documented. Most authors mention the image analysis tool used, however the results do not necessarily quantify the particles. Discussion mainly highlights the trend of intermetallic evolution during homogenisation.

2.10 Particle extraction technique

It has been shown that 2-D microstructural particle analysis can be misleading and that techniques suitable for quantification of 3-D structures can provide more reliable information [41]. The SINTEF group of Norway developed a technology for particle extraction by matrix dissolution within Al alloys. The technique is called the SIBUT process and it entails extracting intermetallic particles from the Al matrix using dry butanol. The name is an abbreviation of SINTEF and Butanol (SI-But).

The basic principle of operation is to dissolve the Al-matrix in dry butanol in an inert gas environment, while leaving the intermetallic particles unaffected. Particle extraction is necessary for intermetallic particle volume fractions (VF) examination because dilute alloys have relatively small VF of intermetallic phases, which results in X-ray diffraction plots showing the matrix contribution and not the intermetallic contribution [27, 29, 46 and 47]. The process also permits determination of elements that exist in solid solution in the matrix [24]. The SEM is typically coupled with EDS, as well as X-ray diffraction to analyse and identify the extracted intermetallic particles.

2.11 Quantification of intermetallic particles

Quantification of intermetallic particles is very challenging and the minimal available literature reflects this [27, 29 and 46 - 48]. Most often, image analysis software is used to quantify the particles in 2-D analysis. Whereas, some authors use both 2-D and extraction analyses for particle quantification [33, 35, 42, 49 and 50]. Simensen *et al.* [29], Kumar *et al.* [46] and Marie *et al.* [50] all agree that particle extraction through the dissolution of Al-matrix makes 3-D observation of the outer shape of certain particles possible without any bias from mechanical polishing. The authors also used XRD for phase identification, however, there is not enough information on AA3104 intermetallic particle quantification. Therefore, this thesis investigated techniques on how to qualitatively and quantitatively analyse these intermetallic particles.

2.12 Summary of possible investigation within thesis

This research aims to investigate the following:

- The effects of homogenisation on the evolution of intermetallic particles.
- The comparison of techniques used to quantitatively and qualitatively analyse the intermetallic particles
- Which homogenisation temperature yields the desired intermetallic VF and ratio of β and α
- Whether the desired VF of intermetallics (1-3% ideal) is achieved
- Whether the desired ratio of β and α (50% ideal) is achieved

3 EXPERIMENTAL PROCEDURE: QUALITATIVE ANALYSIS

3.1 Material preparation

DC as-cast AA3104 ingot was supplied to UCT Centre of Materials Engineering Department by Hulamin rolled product in Pietermaritzburg South Africa. The chemical composition of the specimens used is listed in Table 3.1. The table also shows the Mn:Fe = 2.1, which is >2.0 as mentioned in section 2.6.4. Specimens were extracted from the ingot for experimental analysis. Due to the variation of the freezing rate during solidification of the ingot, specimens were extracted near the edge (E) and at the centre (C) of the ingot, as seen in Figure 3.1 below. This was done to examine and characterise the microstructural changes within the alloy during homogenisation, whilst taking inhomogenities due to solidification into account. For consistency, material was analysed in the transverse direction with respect to ingot solidification.

Table 3.1: AA3104 chemical composition.

Alloying element	**Si**	**Mn**	**Fe**	**Ti**	**Mg**	**Cu**	**Zn**	**Cr**
Wt%	0.197	0.99	0.477	0.01	1.22	0.197	0.007	0.007

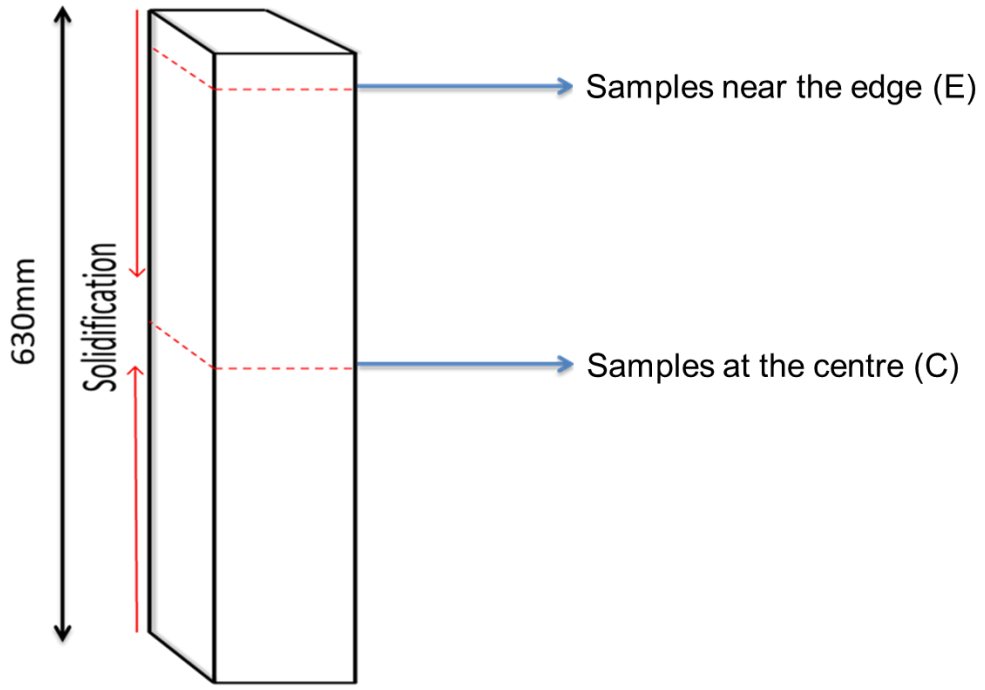

Figure 3.1: Specimen from AA3104 ingot showing locations of interest.

3.2 Homogenisation

Homogenisation is a heat treatment used to eliminate segregation. It is a process that promotes phase transformation as well as even particle size and distribution in AA3104. Homogenisation affects the evolution of the intermetallic particles within the alloy's microstructure. Therefore, experiments were conducted to homogenise the AA3104 material. 10x1.95x1.1 cm^3 specimens were placed in a heat programmable furnace at room temperature (24°C) for homogenisation.

Literature shows that a two-step homogenisation treatment promotes nucleation of the intermetallic particles while preventing too much particle growth [51]. It also generates the required particle structure needed to control recrystallisation during hot rolling and the subsequent crystallographic texture after annealing. However, a homogenisation temperature associated with the required intermetallic particle VF and β-to-α ratio is uncertain. The TSC group conducted research for Hulamin on this alloy and they concluded that homogenisation between 560/520°C and 580°C/520°C yielded desired intermetallic particle and quantities [15]. Therefore, a two-step homogenisation treatment using two different homogenisation temperatures for the first stage, as seen on the graph illustrated in Figure 3.2 has been investigated in this research.

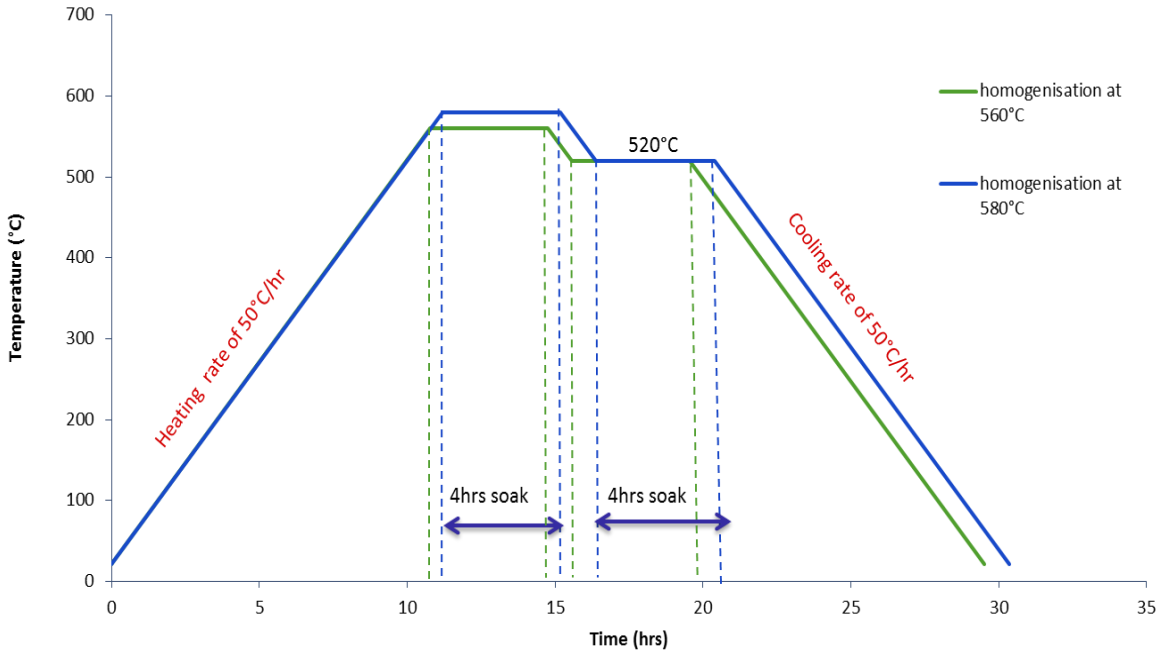

Figure 3.2: Homogenisation treatment used.

Figure 3.2 shows the homogenisation treatments used. The specimens were heated up to 560°C (first stage) at a heating rate of 50°C/hr in a furnace. Followed by a soak 560°C for 4 hours (hrs). The furnace was then cooled to 520°C (second stage) at a cooling rate of 50°C/hr. The specimens were then soaked 520°C for 4 hrs. The specimens were cooled down to room temperature at a cooling rate of 50°C/hr. Due to the Si diffusion rate decreasing dramatically immediately as temperature starts dropping below 580°C, air cooling (faster than 50°C/hr) and furnace cooling do not result in major microstructural differences [15 and 19]. The same homogenisation treatment was repeated on the same alloy using a temperature of 580°C for the first stage. It is important to note that heating/cooling rates do not exceed 50°C/hr, mainly to simulate industrial homogenisation furnace conditions [15].

3.3 Metallography

Both the as-cast and the homogenised specimens were first hot mounted using a Struers labopress-3 hot mounter. The mounted specimens were then metallographically prepared for microscopic analysis using the procedures seen in Table 3.2. The last step, (v), is repeated so as to ensure that the final polished surface is Op-suspension free and the particles are exposed. Steps (iii) to (v) were repeated if the specimen appeared rough or if there were scratches. Specimens used for the Scanning Electron Microscopy (SEM) coupled with Energy Dispersive Spectrometry (EDS) analysis were only prepared using the same procedures from (i) to (v) for a perfectly polished finish. After obtaining a perfectly polished surface finish, three types of etchants were used to determine which best exposed the intermetallic particles as well as differentiate between the phases within the intermetallic particles. The etchants used were warm water as a lubricant during the last polishing step, 10% H_3PO_4 at 50°C for 8 minutes [19] and 20% NaOH at 70°C for 5-10 seconds [52].

Table 3.2: AA3104 metallographic preparation procedure.

	Papers/Pads	Suspension	Time
(i)	New 1200 grit paper	Water	1 minute
(ii)	Old & smooth 1200 grit paper	Water	30seconds/1 minute
(iii)	Mol pad	3µm-suspension	6 minutes
(iv)	Nap pad	Op-suspension	4 minutes
(v)	Nap pad	Warm water	2 minutes

3.4 Effect of etchants

As-cast and homogenised specimens were metallographically prepared and etched using three different etchants, namely: warm water, 20% NaOH and 10% H_3PO_4. Etching with warm water only exposed the intermetallic particles, while excluding grains and grain boundaries, as well as dispersoids within the matrix, as seen in Figure 3.3 (a). However, this form of etchant does not distinguish between the α-phase particles and the β-phase particles.

Etching with 20% NaOH at 70°C on the other hand exposes grains with grain boundaries, as well as intermetallic particles and dispersoids within the matrix. The 20% NaOH attacks the β-phase, hence showing the β-phase particles as dark and α-phase particles as light grey, as seen in Figure 3.3 (b). Etching with 10% H_3PO_4 at 50°C exposes the intermetallic particles as well as fewer dispersoids compared to specimens etched with 20% NaOH. The 10% H_3PO_4 reacts with the Si within the particles thus turning the α-phase particles dark and β-phase particles light grey, as seen in Figure 3.3 (c). The Al matrix appears as a lighter grey colour contrast within the microstructure when etched with all three different etchants.

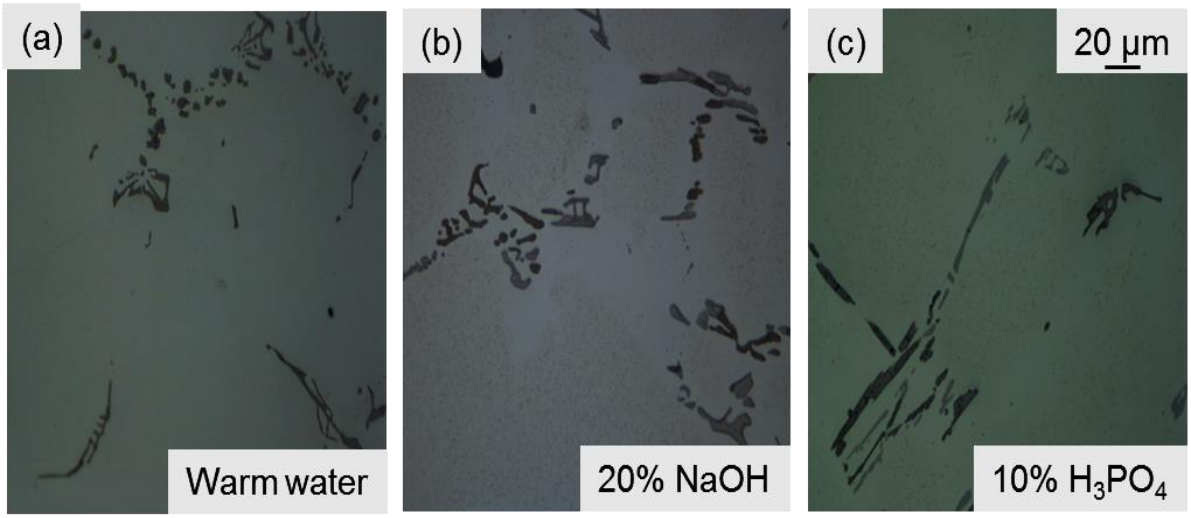

Figure 3.3: Micrographs showing how different etchants expose the AA3104 intermetallic particles within the microstructure, etched with (a) warm water, (b) 20% NaOH and (c) 10% H_3PO_4.

3.5 Microstructural analysis using light microscopy and SEM coupled with EDS

A Nikon Eclipse MA200 light microscope was used to analyse the microstructures of the specimen in order to distinguish the α-phase particles from the β-phase particles. For more detailed investigation, Nova NanoSEM 230 coupled with EDS at an acceleration voltage of 20keV, was also used for intermetallic particle morphology and compositional analysis on both as-cast and homogenised solid specimens. The α-phase particles were compositionally distinguishable from β-phase particles using the presence of Si within the intermetallics as the identifier.

3.6 Extracted intermetallic particle analysis using SEM coupled with EDS

The Nova NanoSEM 230 coupled with EDS at an accelerated voltage of 20keV, was used to morphologically and compositionally analyse, and distinguish the extracted intermetallic particles on both as-cast and homogenised samples.

4 EXPERIMENTAL PROCEDURE: QUANTITATIVE ANALYSIS

4.1 Intermetallic particle volume fraction estimation using 2-D technique

Literature on image analysis shows that $\frac{A}{A_{tot}} = \frac{V}{V_{tot}}$ on a 0% interaction plane, therefore percentage area (A%) can be reported as volume fraction (VF) [53]. However, optical microscopy (OM) images are used instead of SEM images. This is because a greater surface area is covered at lower magnification using OM. Freeware ImageJ and MATLAB R2013b programs are used to quantify the intermetallic particles contained in AA3104 by estimating particles A% using pixel count on a greyscale range. The analysis was conducted on specimen in the as-cast condition and after different homogenisation treatments (for both Edge (E) and Centre (C) specimens). The analysis involves firstly using optical microscopy to acquire micrographs at 20x and 50x magnification. Micrographs at 20x magnification tend to not show the Al-spots within the α-phase particles and thus lead to errors. 50x magnification micrographs were used for particle VF estimation as the error was decreased with increased magnification. Approximately 250 micrographs were randomly acquired at 50x magnification to remove bias error. These micrographs were then analysed using the two programs as described in section 4.1.1 and 4.1.2.

4.1.1 ImageJ

ImageJ is described as a public domain Java image processing and analysis program inspired by NH Image for the Macintosh. The program works by counting the number of pixels that lie within a greyscale range. This program was used mainly to determine the Al-matrix and intermetallic threshold values within the AA3104 micrographs. The threshold values were then used in MATLAB to estimate the intermetallic particle VF. Details of how the program works can be viewed in Appendix 1 and 2.

Firstly, an image to be analysed was opened via the program. A scale was set to calibrate an image against known values (μm, cm, etc.). The image was then changed to greyscale so as to emphasize the difference in the microstructure contrast. The matrix appears as light grey, β-phase particles as medium grey and α-phase particles as dark grey. The image was then thresholded according to the greyscale pixel intensity and the threshold number (ranging from 0 to 255) was recorded. When estimating the threshold number, 45 images at 50X magnification were analysed for each specimen. Each image was thresholded and the number was recorded. A mean threshold value was then calculated using these results. The mean threshold value for each specimen was then used to estimate intermetallic particles VF using MATLAB.

The program was not used to its full capacity because it tends not to recognise irregular intermetallic particle shapes. This means that the program actually includes Al-spots within the α-phase particles, which are of a different contrast to the α-phase particles. This then yields higher A% results. Another error occurs due to the presence of dispersoids within the matrix containing the same greyscale contrast as the intermetallic particles. Thresholding tends to include these dispersoids, hence resulting in a slightly larger particle VF. Human errors arise due to this analysis being conducted at different conditions. For example, different mind-sets tend to report a slightly different threshold value, resulting in slightly different VF. Also, the change in light micrograph settings changes the thresholding value. Therefore, one ought to be careful. Finally, it is important to take note of the intermetallic particle pull-out on the specimen, which leads to particle VF variation when comparing specimen analysed under the same conditions.

4.1.2 MATLAB R2013b

MATLAB (matrix laboratory) is a multi-paradigm numerical computing environment and fourth-generation programming language. Most use of MATLAB involves typing MATLAB code into the Command Window (as an interactive mathematical shell), or executing text files containing MATLAB code, including scripts and/or functions. This image processing software was used to estimate intermetallic particle VF (Area%) within AA3104 micrographs. Steps on how particle VF was estimated are seen in Appendix 3.

MATLAB was firstly opened and two windows containing the script code and command are visible. File names of images were entered on the script code window. The image threshold values estimated using ImageJ were then entered into the script code window corresponding with the image file name for each specimen. The script was then saved and run. Excel spreadsheets containing data are produced as outputs and then saved in the directory (path) folder. This analysis is conducted on overall particles, α-phase particle as well as Mg_2Si particles within the microstructure of the alloy. Therefore, the same MATLAB steps were run while using the appropriate threshold value according to the particles of interest. The excel spreadsheets were then opened for statistical analysis and calculation of the particle VF estimation was conducted. Images that showed a dirty surface as well as evidence of particle pull-out on the microstructure were removed as a way to keep the analysis consistent and accurate.

4.2 Statistical analysis

The number of fields of view (F.O.V) necessary to report a meaningful intermetallic particle VF after image analysis is unknown. This is due to the fact that VF estimation error is associated with the average number of intercepted features per area, the number images (fields of view) and the desired confidence interval. Therefore, several statistical approaches were used to evaluate the number of fields of view necessary for particle VF estimation. This was achieved by using the following tests, described below.

4.2.1 Average intermetallic particle VF as n changes

After conducting image analysis, graphs of particle VF average vs number of F.O.V = n were plotted, seen in Figure 4.1. The graph shows how the average VF per specimen slightly varies with respect to the number of fields of view acquired, however the graph tends towards a straight line after a number of fields of view have been analysed. The straight line shows a constant average particle VF, hence n should be where the straight line begins. The value of n is estimated for all specimens and then an average of those n's is used to report the final particle VF results after image analysis.

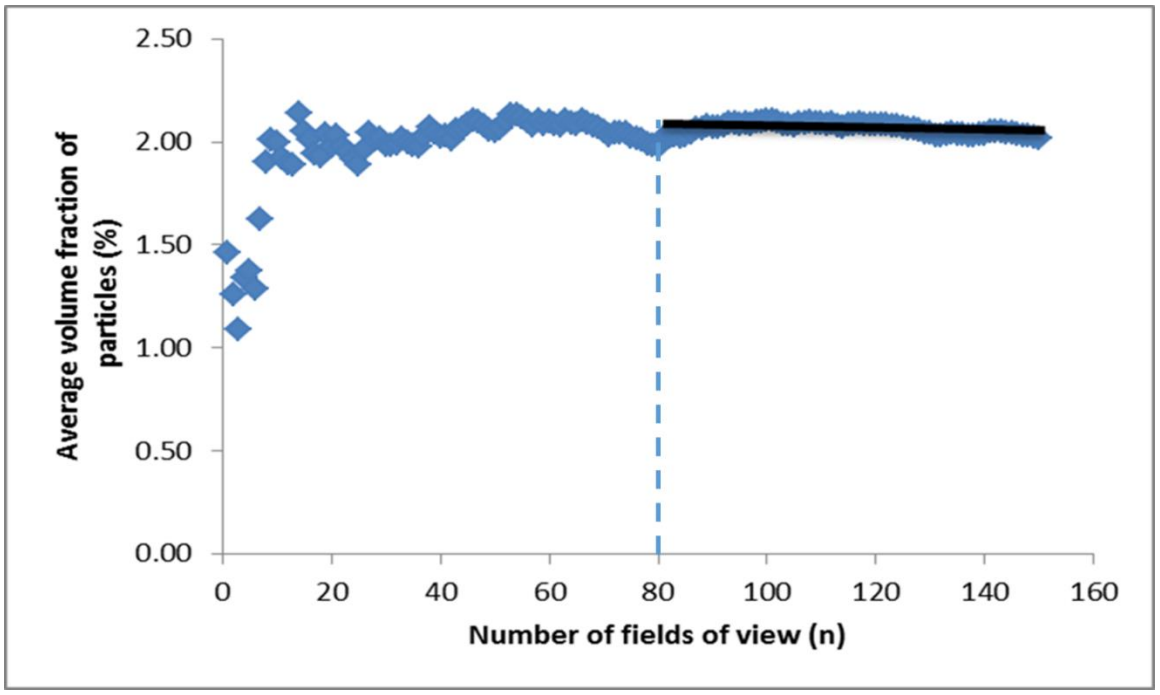

Figure 4.1: Graph showing the number of fields of view necessary to obtain a meaningful volume fraction.

4.2.2 Normal distribution

A Gaussian distribution test was conducted on the results obtained from ImageJ and MATLAB. This test was necessary to analyse if the VF estimation data is normally distributed in order for further statistical analysis, such as confidence interval, to be determined.

4.2.3 Relative accuracy of necessary numbers of fields of view using confidence intervals

A relative accuracy method developed by Van der Voort was also used to further evaluate the number of fields of view necessary to estimate a meaningful particle VF [54]. Van der Voort states that a 10% relative accuracy (RA) is generally satisfactory for most measurements. However, a higher %RA value is generally accepted because it is difficult to obtain a level of confidence when dealing with measurements of inclusions/second phase particles. Therefore, from a practical viewpoint, n values between 100 and 300 are necessary [54]. The evaluation was conducted using Equation 1 and $\%RA=\frac{100(95CI)}{\mu}$ Equation 2 within 99.5%, 99% and 95% confidence intervals. Where 95CI represents 95% confidence intervals, z is the statistical critical z-value, s is the standard deviation, n is the number of fields of view and μ is the mean value. The CI critical z-value used for this analysis are found in Appendix 4.

$$95CI = \pm \frac{zs}{\sqrt{n}} \quad \text{Equation 1}$$

$$\%RA = \frac{100(95CI)}{\mu} \quad \text{Equation 2}$$

4.3 Thermodynamic calculations using JMatPro

Thermodynamic calculation was conducted under equilibrium using JMatPro software. The software was used to predict phase equilibria present within AA3104 alloy. The predicted phases and their quantity were then used to estimate the phases expected when conducting X-ray diffraction (XRD) on as-cast and homogenised AA3104 specimens. The software was also used to get an idea of how much of each phase is present within the alloy before and after homogenisation.

4.4 Particle extraction

The Intermetallic particle extraction process used for this research was adapted from The SiBut Method [29, 46 and 48]. This is a technique used to extract intermetallic particles from the aluminium matrix for identification and analysis purposes. The technique was developed by the SINTEF Group of Norway. The name was abbreviated as 'Si' from SINTEF the organisation and 'But' from butanol, the solvent used. The basic principle of this process is to dissolve the aluminium matrix in dry butanol under an inert gas environment while leaving the intermetallic particles unaffected. Below are the details of how the experiment is conducted.

4.4.1 Drying butanol

Analar (of pure standard) butanol contains very low water (H_2O) of about 0.01wt%, however the H_2O content is too high for this process/application. Consequently, a still, seen in Figure 4.2, was used to dry the butanol further. The still works by heating the butanol to its boiling temperature, 121°C, under pure argon (Ar) gas using a heating mantle. This reaction is quite sensitive to water, the atmosphere and takes a long time to complete. Three pure Al (AA1200 series) specimens added in the round bottom flask speed up the drying process by reacting with water in the butanol. As the liquid boils, the butanol and any water not reacting with the pure aluminium will evaporate.

Furthermore, a gas adapter was inserted at the top of the still to introduce Ar (inert) gas that prevents any oxidation of the aluminium specimen. The gas adapter has a vacuum port that keeps out airborne water vapour. The water cooled coiled condenser allows water vapour and hydrogen gas (evolved in the butanol/aluminium reaction) to escape through the vacuum port while the butanol vapour condenses and drips back into the collecting flask/vessel. The round bottom flask and evaporation tube (connected to the collecting vessel) are covered with cotton and foil for insulation, thus making the evaporation process happen faster. Lastly, a silicon tube is fitted on the collection vessel tap to transfer dry butanol.

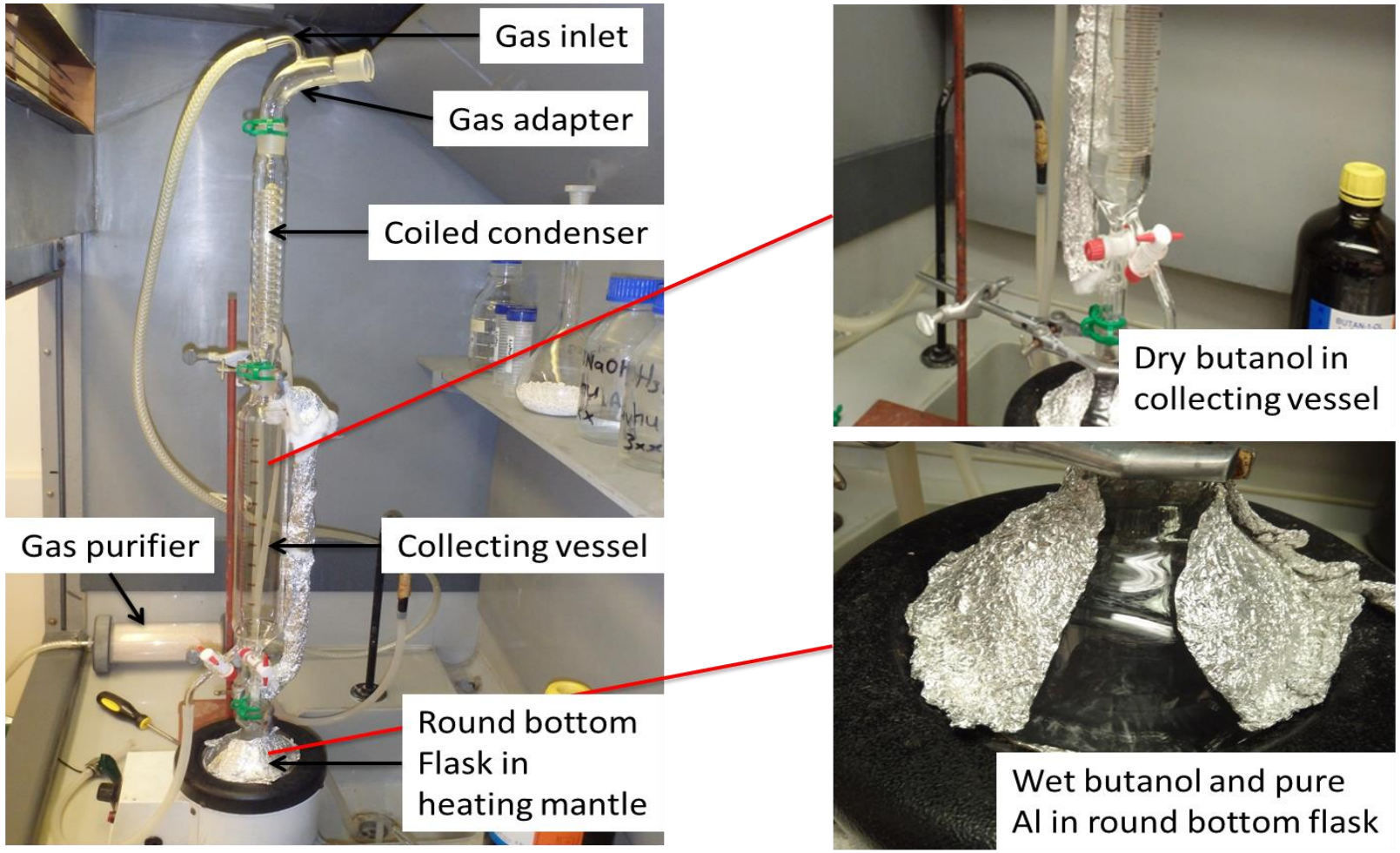

Figure 4.2: Image showing the setup used for drying butanol.

The drying process time is depended on the purity of the Ar gas. A gas purifier, designed by Mudindivhathu Tshivhombela, a fourth-year Mechanical Engineering student was used to remove any moisture from the Ar gas used. The drying time ranged from 2 hours to 8 hours, with 2-3 hours being the most common time.

Different amounts of wet butanol were distilled to see what amount yields more dry butanol. Table 4.1 shows that 225ml wet butanol yields more dry butanol of 150ml compared to the 400ml yielding 250ml dry butanol in a 500ml round bottom flask at a shorter time. However, mass drying for mass dissolution would be ideal. The minimum drying time is influenced by the purity of the Ar bottle, the amount of butanol dried at a time, as well as how often the equipment is used. Therefore, the dirtier the Ar bottle and the longer it takes to re-use the equipment, the longer the drying process takes.

Table 4.1: Time taken and yield acquired when drying/distilling a certain amount of butanol.

Wet butanol in flask (ml)	Dry butanol yielded (ml)	Distillation/drying time
220	110	2-3 hrs
225	150	2-3 hrs
250	150	2 hrs 30 min-5 hrs
400	250	8 hrs 45 min

4.4.2 Preparing specimen and autoclave

1.0g specimens were cut from as-cast and homogenised specimens, at edge and centre ingot locations. The specimens were cleaned first with acetone and then with ethanol. The dissolution of the matrix took place in a stainless steel autoclave. The autoclave was prepared by first putting it in a bucket full of tap water. The bucket full of water plus the autoclave was then put in an ultrasonic bath for 10 minutes. After that, the autoclave was rinsed with distilled water, followed by de-ionised water and then dried with acetone. The cleaned autoclave is then placed in the oven at 135°C for 1 hour before drying butanol is complete. After running a few experiments, the autoclave bottom valve tends to get blocked. Therefore, filling the bottom valve piece with acetone then placing it in the ultrasonic bath for longer dissolves the gel blocking it.

4.4.3 Dissolution

During dissolution of the Al matrix, a stainless steel autoclave, seen in Figure 4.3, was fitted with a 0.1µm grade Teflon filter, stainless steel mesh and stainless steel ring to hold the filter paper down in the base.

Firstly, the autoclave was put in the oven for one hour before the butanol drying process was complete. The pre-weighed PTFE filter was then inserted into the autoclave straight from the oven. Whilst still warm, the autoclave was evacuated and purged with Ar gas which passes through a stainless steel pipe, shown by the red arrows in Figure 4.3, connected to a vacuum port and pressure gauge. The evacuation and purging was repeated twice before the weighed specimen was inserted through the top of the autoclave (which was still under an Ar purge so that there was a positive Ar pressure ensuring that no air could enter).

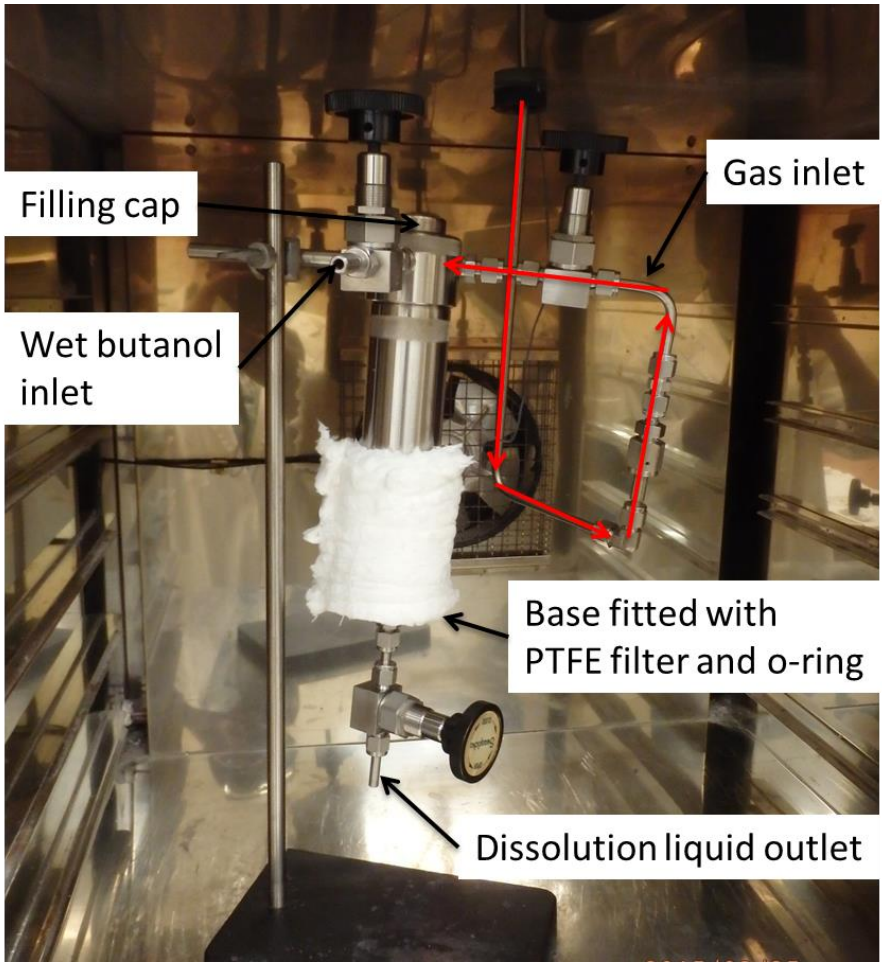

Figure 4.3: Illustration showing the setup of the stainless steel autoclave used for particle extraction.

A quantity (100ml) of dry butanol, obtained from the still was transferred into the autoclave via the top inlet valve, which was subsequently sealed and placed in an oven at 135°C. An insulation blanket was placed on the autoclave to speed up the process. The dissolution process takes approximately 6 to 12 hours to complete, during which at that time the pressure rises from 3.7 to 5.5 bars depending on how dry the butanol is. The pressure rise in the autoclave results from the superheating of the butanol and the evolution of hydrogen gas as a by-product of the aluminium/butanol reaction.

Once the dissolution is finished, the oven is opened and the bottom seal is opened allowing the internal pressure to force the liquid out of the autoclave, where the intermetallic particles, suspended in the liquid are collected by the Teflon filter. When the autoclave has reached atmospheric pressure, 15ml ethanol was poured from the top of the autoclave to rinse any excess powder. This step was repeated once to ensure that the powder is properly cleaned. After rinsing, the bottom valve was loosened. Then the filter paper, together with intermetallic particles, metal mesh and ring were collected into a pre-weighed petri dish. The petri dish and its contents were then weighed. Intermetallic weight% was then estimated from the weighed material. Extensive experimentation showed that dissolution of a specimen $\geq$ 2.0g leads to a rise in pressure of up to 5.5 bars which results in the PTFE melting, thus contaminating the extracted particles.

The same technique was used to partially dissolve the upper surface of some AA3104 specimens, thus exposing intermetallic particles whilst still in position (grain and cell boundaries) in the upper surface. This topographical surface was then analysed using SEM coupled with EDS. This was achieved by making sure that the dissolution step did not reach completion, meaning that the dissolution step was only run on 0.6g specimens for 4.5 hours instead of the full 6 hours.

Figure 4.4 shows the specimen before dissolution and extracted particles sample collected after dissolution. After particle extraction was complete, the particles were collected and then analysed using light microscopy for morphological analysis, SEM coupled with EDS for morphological and elemental analysis, as well as using X-ray diffraction for phase identification and analysis.

Figure 4.4: Images showing the process of dissolution from a solid AA3104 specimen to powder sample (extracted particles).

4.5 X-ray diffraction

X-ray diffraction (XRD) technique was performed at the UCT Chemical Engineering Department. A Bruker D8 advanced with a Vantec position sensitive detector was run on both solid and powder samples that were extracted using a Cobalt (Co) anode, a step time of 900.7 and a step size of 0.0123322. Both the as-cast and the homogenised samples were analysed in solid and powder form. The solid specimens analysed were between 3-4 mm in height, which is the restricted height. It was difficult to recognise/match peaks of Fe-bearing intermetallic particles on solid specimens due to the matrix interference. It was also difficult to identify phases on the extracted particles powder because they contained a lot of amorphous material that is considered as contamination. However, phase recognition and quantification of the extracted intermetallic particles was possible.

After conducting XRD, a spectrum was generated and MDI Jade 5.0 software was then used to match the peaks thus identifying the phases within the extracted particles. This was achieved by manually indexing the peaks for each specimen using the phase's crystallographic information. Figure 4.5 shows a XRD spectrum/pattern highlighting the phases expected. Given the fact that VF analysis was conducted using image analysis and XRD with the Rietveld method, it was taken into account that the 2-D method shows 3 phases, whereas the particle extraction technique shows more phases in detail. Thus, the methods complement each other.

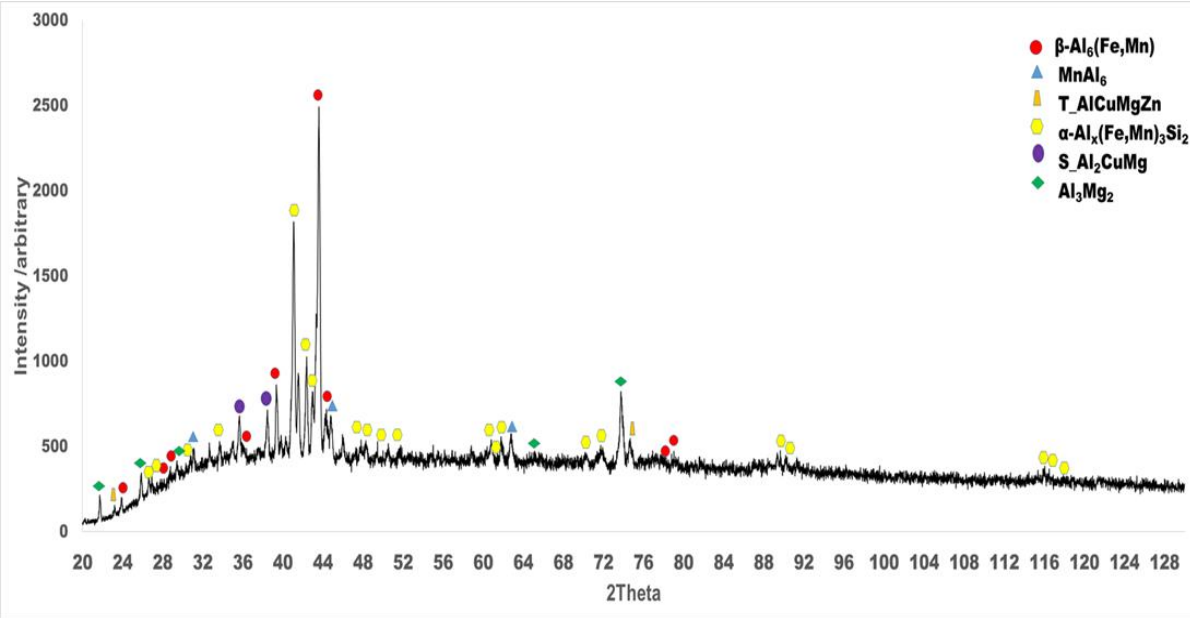

Figure 4.5: XRD spectrum/pattern generated from the extracted particles after homogenisation showing the phases expected.

4.6 The Rietveld method

This method was used to estimate the percentage of each phase contained within the extracted particle. This was achieved using Topas software that automatically calculates the area under each peak. The software then generates a text file which is then opened using Excel. Firstly, phases and peak positions are identified using MDI Jade 5.0 software. After that the sum of areas under each peak is normalised to 1. Phase percentage is then calculated which then results in particle phase quantification.

4.7 Summary

Figure 4.6 shows a summary of the different testing methods used to analyse/evaluate the evolution of intermetallic particles within AA3104 during homogenisation. Both the as-cast and homogenised samples were analysed using microstructural and particle extraction techniques. The investigation involves areal microstructural analysis using light microscopy, SEM with EDS and image analysis as the 2-D technique. Additionally, particle extraction, SEM with EDS, XRD and the Rietveld method was used as the 3-D technique. These techniques were then compared to see if they agree or if one is more reliable than the other.

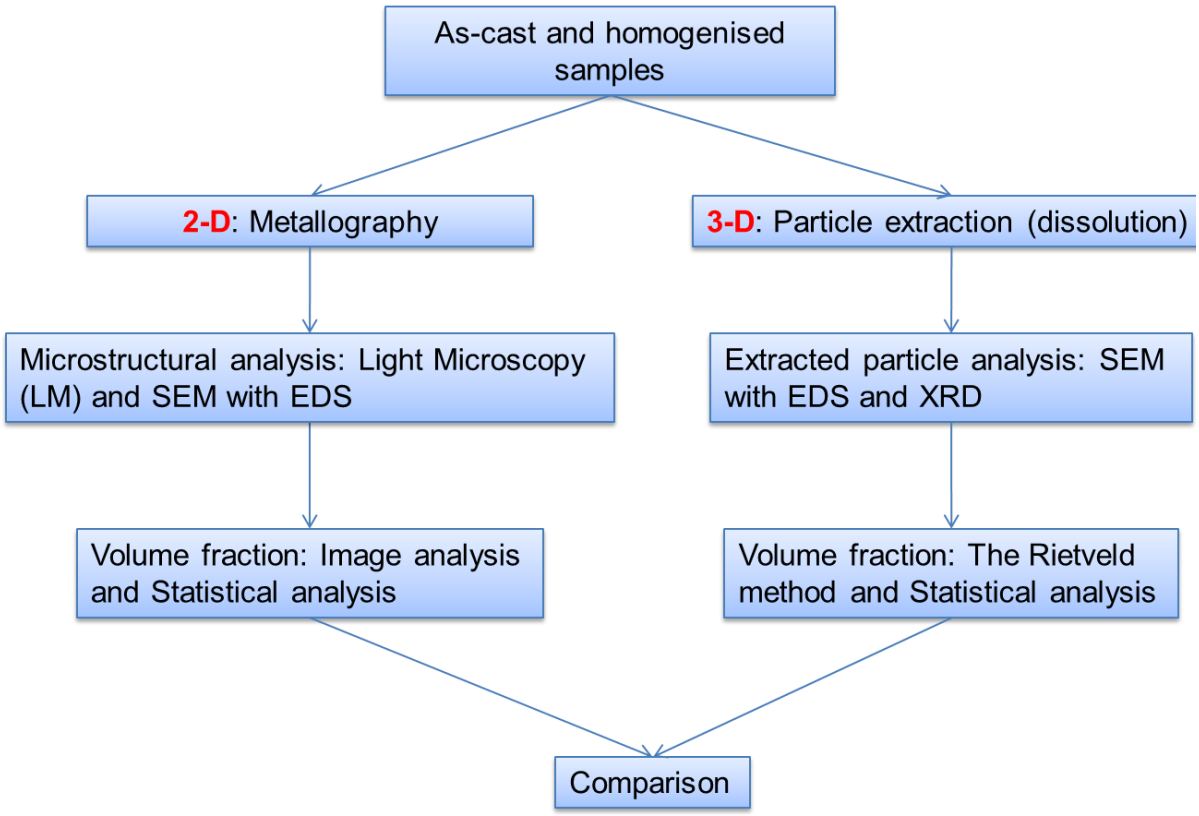

Figure 4.6: Summary of the experimental procedures conducted.

5 RESULTS AND DISCUSSION: MICROSTRUCTURAL EVOLUTION OF AA3104–QUALITATIVE EVALUATION

As-cast and homogenised specimens from near the ingot edge and centre of the ingot were microstructurally analysed using light microscopy, as well as using SEM coupled with EDS for compositional analysis. It is important to note and not confuse the two phases when analysing microstructures using light microscopy and SEM. The α-$Al_x(Fe,Mn)_3Si_2$ phase particles are brighter in SEM backscatter micrographs because α-$Al_x(Fe,Mn)_3Si_2$ particles have a greater atomic number than the β-$Al_6(Fe,Mn)$ particles due to the presence of Si. However, light microscopy shows α-phase particles as darker and β-phase particles are lighter depending on the etchant used. Below are observations and discussions on how the microstructure in AA3104 evolves during homogenisation, both near the edge and at the centre of the ingot.

5.1 As-cast microstructure

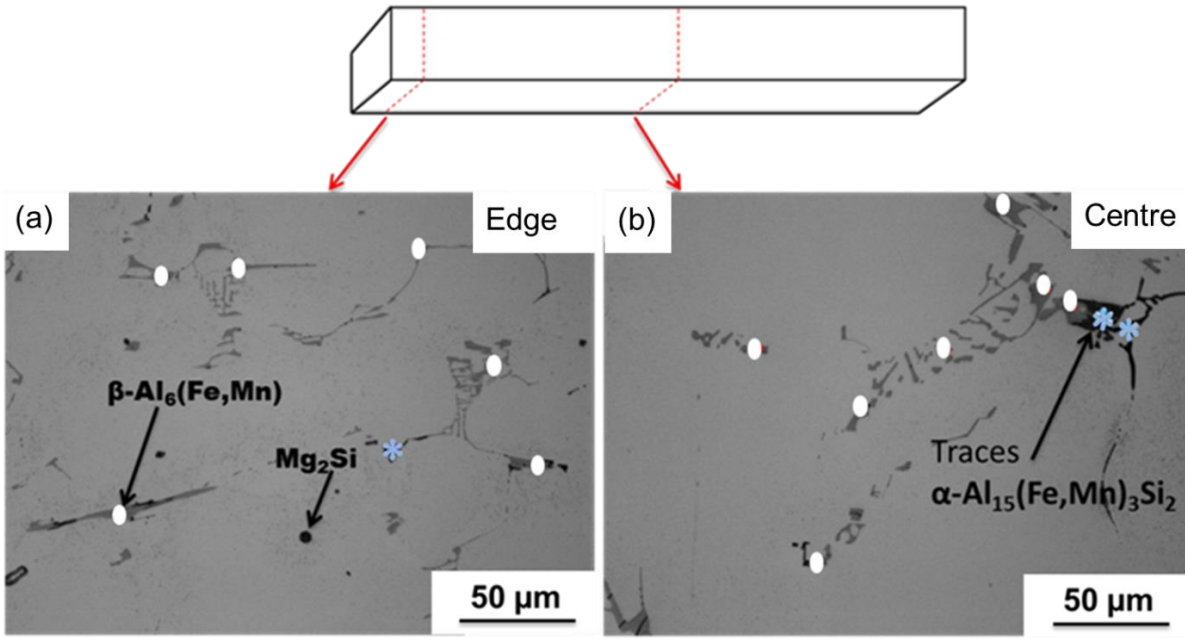

Figure 5.1: Light micrograph of AA3104 showing intermetallic particles (a) near the edge and (b) at the centre of the ingot both in the as-cast condition, etched with 10% H_3PO_4 at 50°C.

Micrographs in Figure 5.1 shows the presence of β-Al_6(Fe,Mn) phase as lighter needle-like particles, Mg_2Si as black spots and the α-Al_x(Fe,Mn)$_3Si_2$ phase as the darker Chinese-script-like particles. There is a low amount of α-phase indicated by blue snow, whereas the β-phase, indicated in white spots, is the predominant phase, as expected from literature [18 - 20]. The cast microstructure shows that the specimens near the edge, seen in Figure 5.1 (a), contain a greater number of finer intermetallic particles compared to the ingot centre, which contains fewer, coarser intermetallic particles, seen in Figure 5.1 (b). This is explained by the change in the solidification rate and growth kinetics that increases from edge to centre of the ingot.

Figure 5.2 shows the major elements present within the intermetallic particles in the as-cast condition. It is seen that the intermetallic particles contain very little Si at this stage. This suggests that the particles consist mostly of β-Al_6(Fe,Mn) phase which does not contain Si. Thus, β is the predominant phase formed during casting. Though Figure 5.2 (a) shows no evidence of Si within the particles, Figure 5.2 (b) does show evidence of this element present within the particles (circled in red), which indicates that the microstructure does consist of traces of α-Al_x(Fe,Mn)$_3Si_2$ phase. Figure 5.1 shows the presence of Mg_2Si with reference to Wycliffe *et al.* [13] and Ricky *et al.* [15] particle identification. The EDS maps also show the presence of Mg, however most of it is seen in the matrix. This suggests that the presence of Mg_2Si was not easy to identify within the microstructure [50].

Elemental analysis was also conducted on partially dissolved specimens however, the results were affected by the topography on the surface of the specimen, and were thus inconclusive. This was owing to the fact that EDS failed to capture all the emitted x-rays during elemental analysis. Notwithstanding these measurement issues, some of the intermetallic particles were able to be identified as β-phase or α-phase using the presence of Si. The particles were also identified morphologically. The β-phase contains a more needle-like shape, circled in black on Figure 5.3 (a) and (b), whereas the α-phase particles were difficult to locate within the as-cast specimens. It is also seen that the intermetallic particles at the centre are coarser than the particles near the edge of the ingot in the as-cast condition.

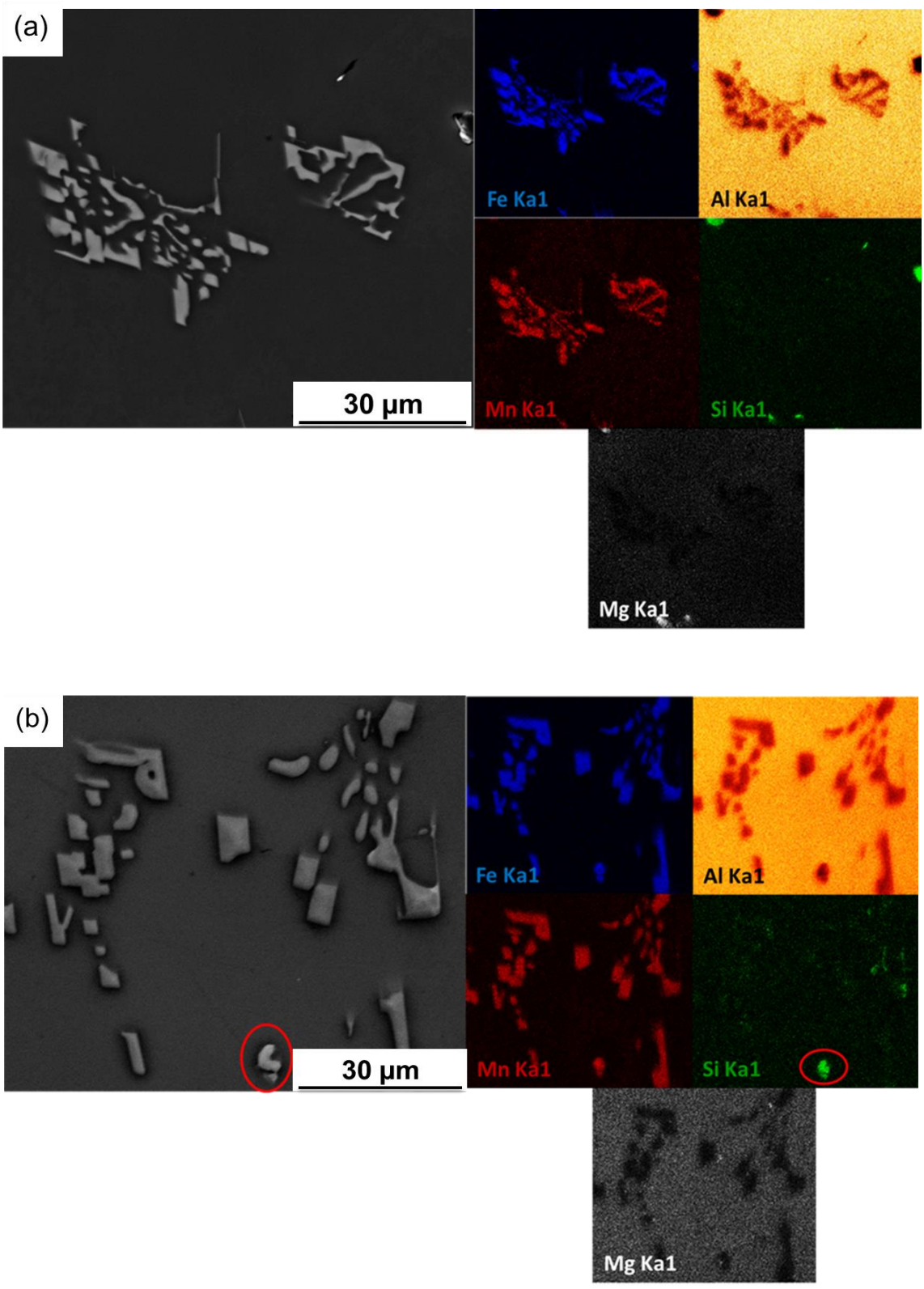

Figure 5.2: SEM Backscatter and secondary electron micrographs, coupled with EDS maps, showing the major elements present within the intermetallic particles. (a) A β-phase particle near the edge and (b) a β-phase particle with a trace of an α-phase particle indicated by red circles at the centre respectively, both in the as-cast condition.

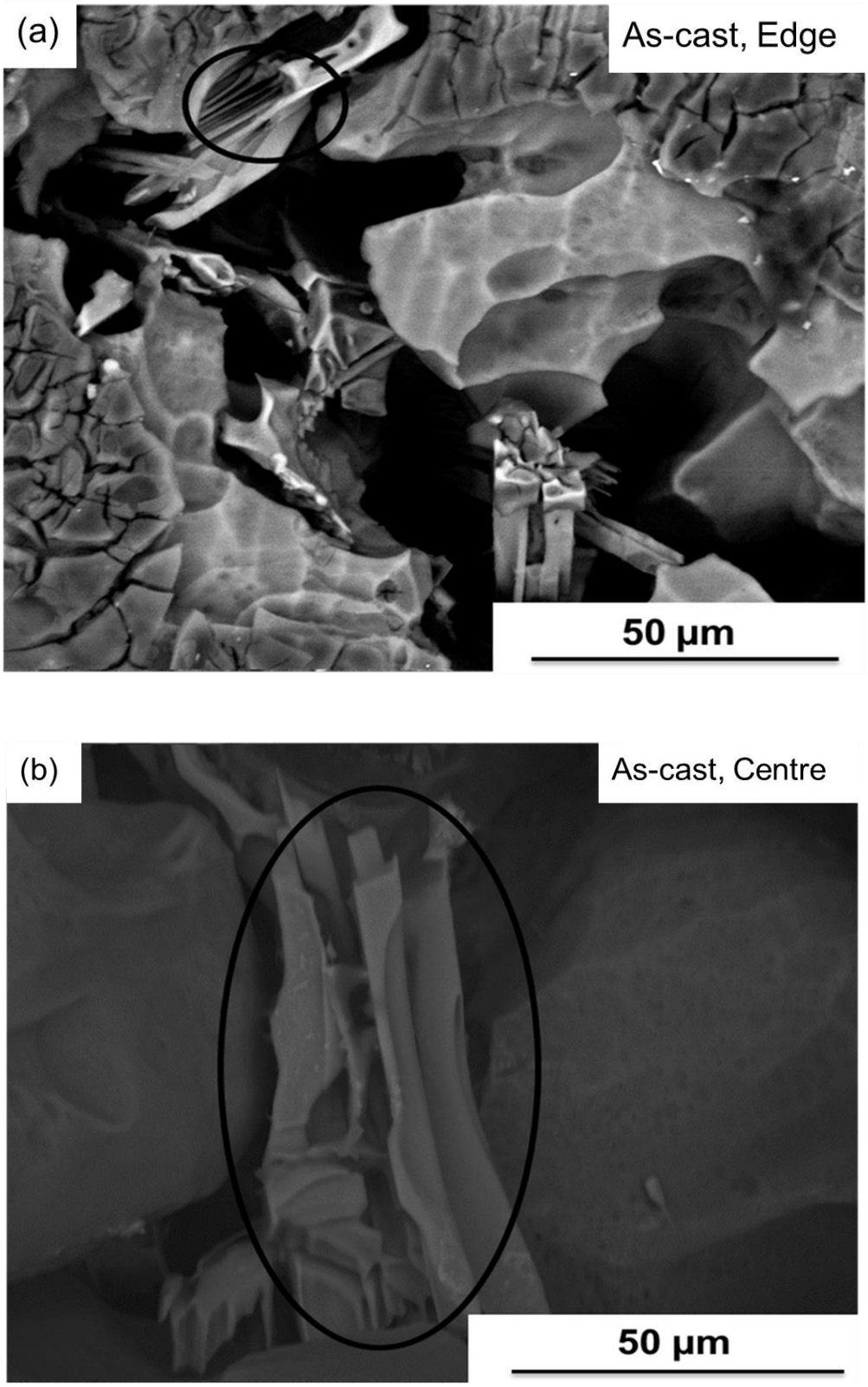

Figure 5.3: SEM Backscatter electron micrographs showing partially dissolved AA3104 specimens exposing the β-phase, needle-like intermetallic particles in situ at the grain boundaries circled in black (a) near the edge and (b) at the centre both in the as-cast condition.

5.2 Intermetallic features after homogenisation of AA3104

The homogenised AA3104 microstructure consists of α-$Al_x(Fe,Mn)_3Si_2$ and β-$Al_6(Fe,Mn)$ as the dominant particle phases. The Mg_2Si particles dissolve as the homogenisation temperature increases, thereby supplying Si to the β-particles resulting in phase transformation through diffusion. The α-phase particles appear brighter than the β-phase particles using backscatter electron imaging (BEI) due to the higher average atomic number of the α-phase. The increase in α-phase during homogenisation occurs through eutectoid phase transformation where some α-phase particles grow through particles from the particle-matrix interfaces, producing duplex particles. These α-phase particles are recognised by the regions containing Al-spots within the particle, which have the same dark contrast as the matrix [21].

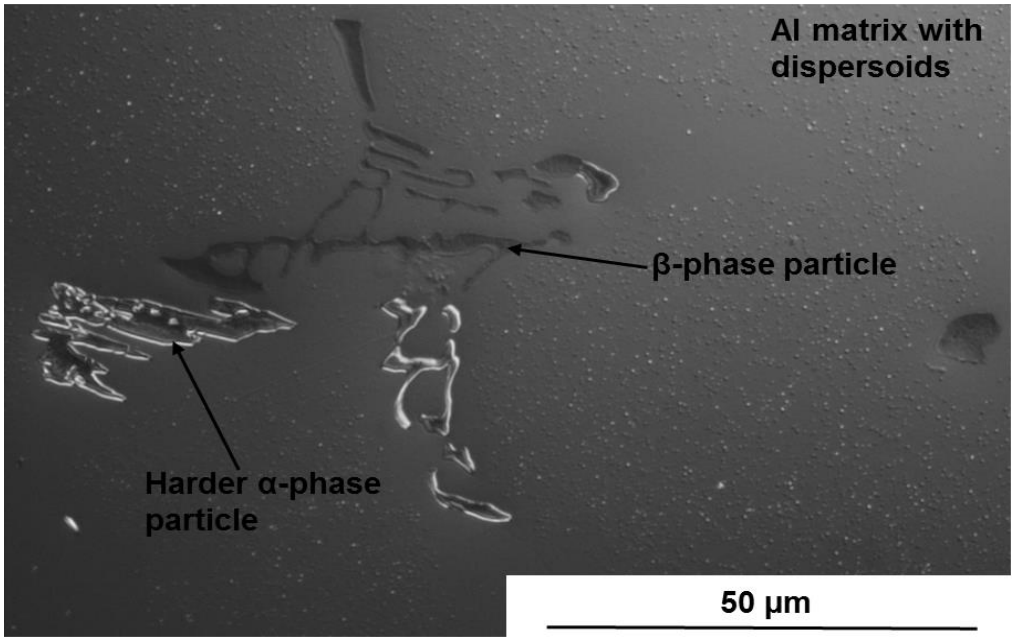

Figure 5.4: Normaski micrograph showing topographical difference between the intermetallic particles within the microstructure of specimen near the edge of the ingot homogenised at 580°C/520°C for 31 hrs. Etched with 10% H_3PO_4 at 50°C.

Light microscopy was used to show how the phases can be differentiated based on their contrast and morphology. Figure 5.4 shows that the β-phase particles are softer than the matrix and that the α-phase particles are harder than the matrix. The figure also shows the presence of dispersoids on the matrix, where most dispersoids has the same colour contrast as the α-phase and few with the β-phase contrast. This is seen by the topographical differences between the intermetallic particles as well as the matrix using the Nomarski lens. Nomarski imaging is a phase imaging technique that gives good rejection of out-of-focus interference by acting as a high-pass filter that emphasises edges and lines.

Figure 5.5 shows a light micrograph containing the Al-matrix with dispersoids, as well as β- and α-phase particles. Particle fragmentation is also seen within the microstructure, which is caused by the homogenisation. The fragmentation of particles that occurs during homogenisation is associated with particle dissolution and phase transformation [8 and 18].

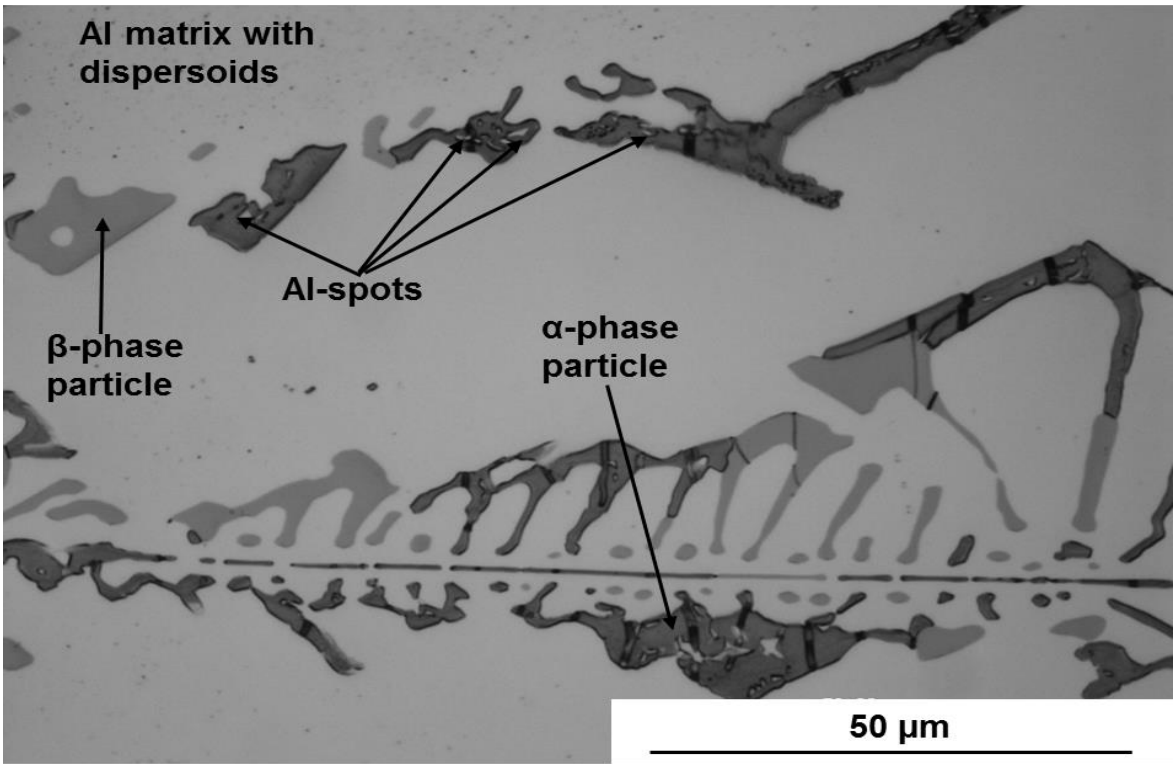

Figure 5.5: Polarised light micrograph showing morphological difference between the β-phase (needle-like or flake-like) and the α-phase (Chinese-script-like) intermetallic particles within specimen at the centre of the ingot homogenised at 580°C/520°C for 31 hrs.

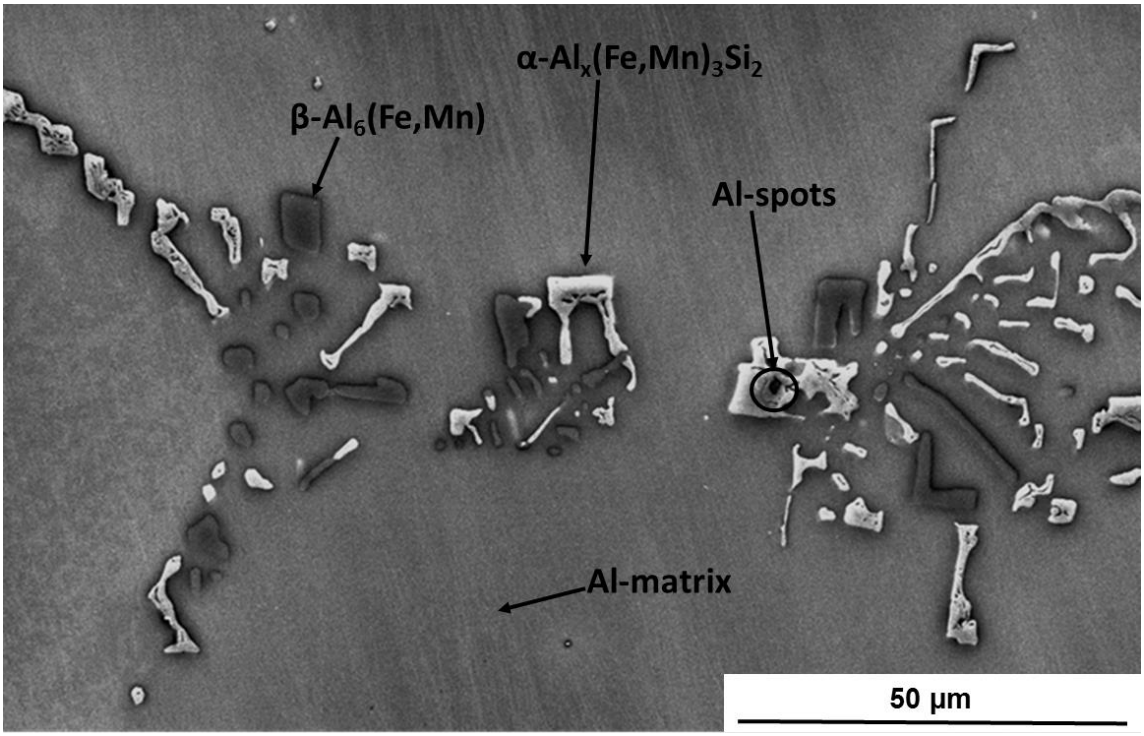

Figure 5.6: SEM Backscatter electron micrograph of specimen at the centre homogenised at 560°C/520°C for 29 hrs distinguishing between the β-phase and the α-phase intermetallic particles through morphology and phase contrast.

It is important to note that particle greyscale contrast differs from light microscopy to SEM micrographs. The β-phase particles are light grey and the α-phase particles are dark grey in contrast with Al-spots containing the matrix contrast within them. While the SEM shows the α-phase particles as light grey and the β-phase particles are darker, as seen in Figure 5.6. The SEM micrograph confirms that the intermetallic particles also differ in morphology depending on phases. The β-phase particles are more needle-like/flake-like and the α-phase particles are more Chinese-script-like with Al-spots within them. Furthermore, the particles differ due to elements present within the phases. Figure 5.7 shows (a) a SEM Secondary electron micrograph with α and β-phase particles, (b) an elemental analysis map highlighting Si in green as the α-phase and the red contours as the β-phase, and (c) an EDS specrum highlighting the major elements within the particle phases. Thus, the Intermetallic particle phases are distinguishable using EDS due to the α-phase containing Si and the β-phase being Si-free.

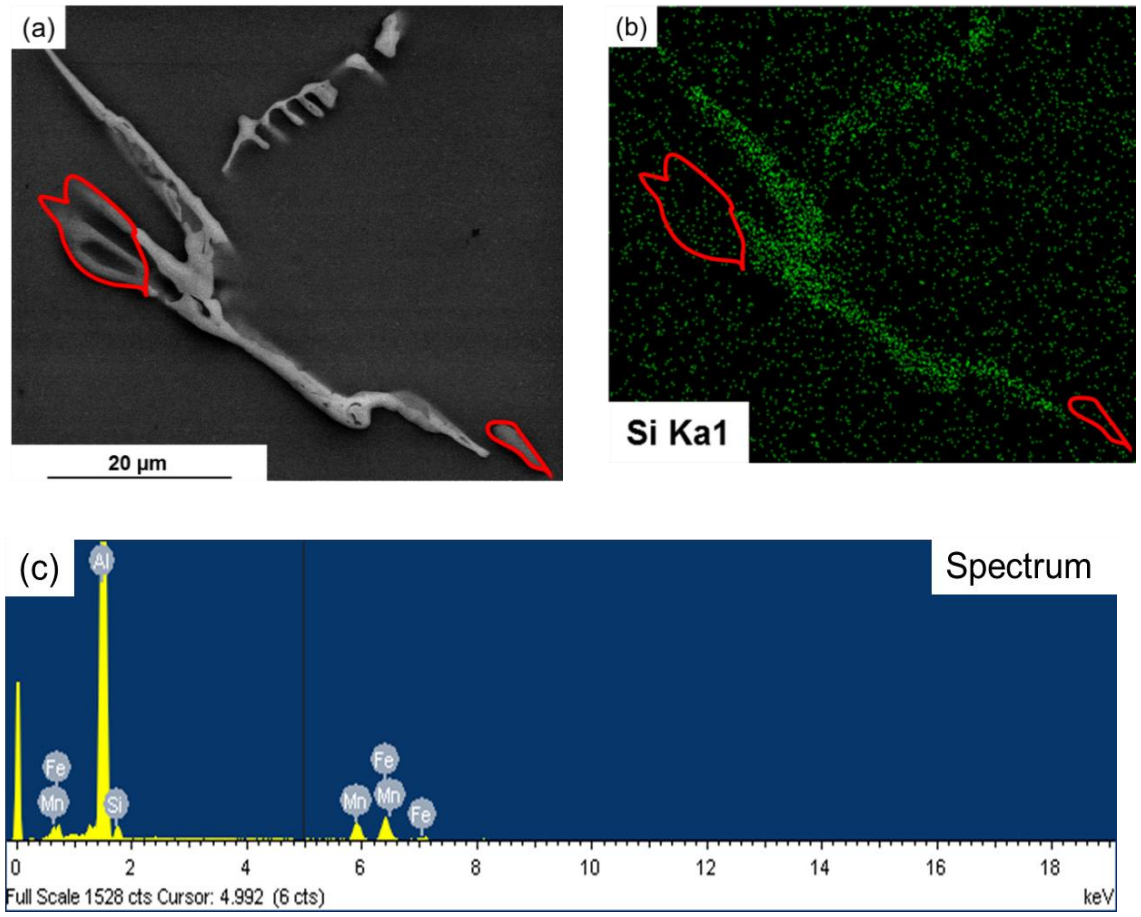

Figure 5.7: Showing (a) SEM Secondary electron micrograph with α and β-phase particles, (b) elemental analysis map highlighting Si in green as the α-phase and the red contours as the β-phase, and (c) EDS specrum highlighting the major elements within the particle phases.

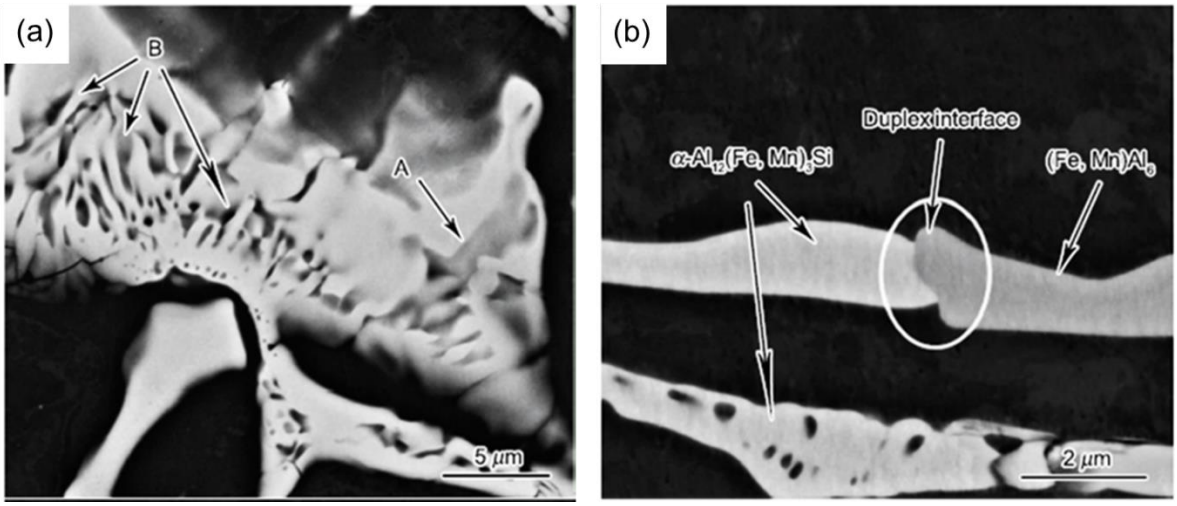

Figure 5.8: SEM micrographs showing α-phase particle morphologies after homogenisation at 550°C/10h. (a) A particle containing Al spots shown as channels indicated by A and B arrows. (b) A particle with a duplex interface differentiating between the two phases [55].

Zhang *et al.* [55] studied the intermetallic particles after homogenisation at 550°C/10h as seen in Figure 5.8. The figure shows micrographs with the morphologies of α-phase particles after homogenisation. The micrographs show Figure 5.8 (a) with Al spots shown as channels indicated by arrows A and B after etching. While Figure 5.8 (b) shows that the α-phase is distinguishable by the Al-spots, as well as the light grey contrast. The micrographs also show a duplex interface as the interface, indicated by a white circle between the two different phases suggesting partial transformation.This interface is also seen in this study as shown in Figure 5.9. The particle phase contrast and morphology difference is also seen on the light micrograph and SEM backscatter micrograph in Figure 5.5 and Figure 5.6. These Al spots are said to disappear by diffusing into the neighbouring matrix also reducing the α-phase particles' size after extended heating times [55].

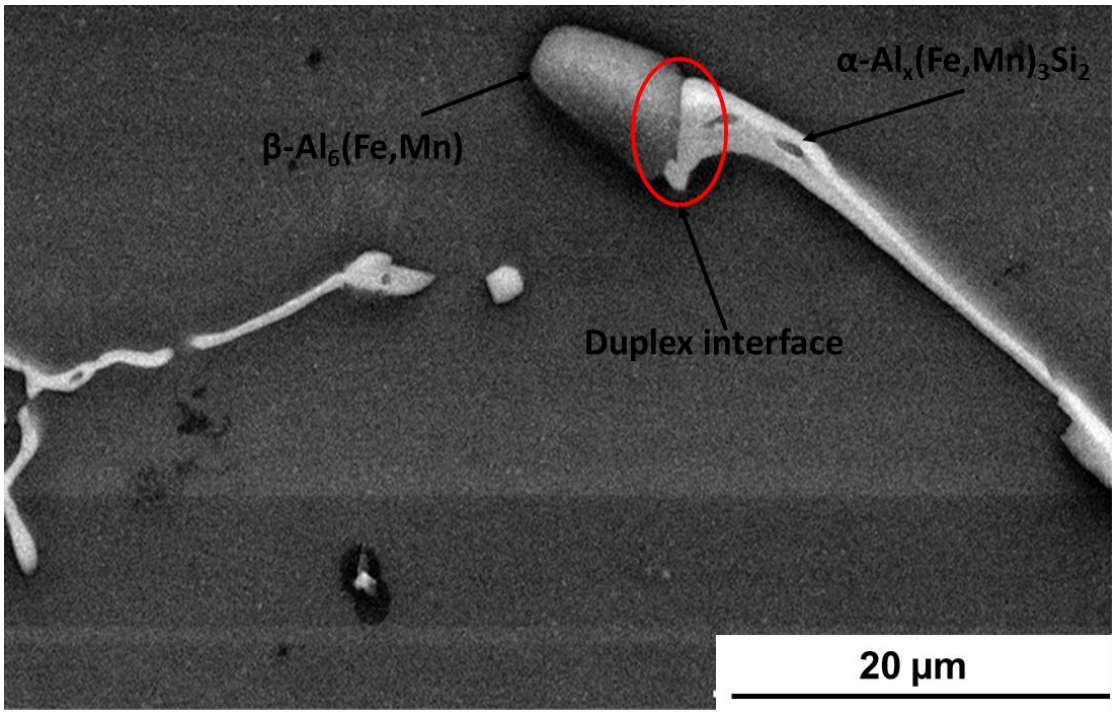

Figure 5.9: SEM secondary electron micrograph showing partial particle phase transformation, circled in red, with a duplex interface showing a transition between the two phases within specimen near the edge homogenised at 580°C/520°C for 31 hrs.

Figure 5.9 shows evidence of partial phase transformation after homogenisation, circled in red, in the AA3104 material. This confirms what Zhang *et al.* observed in Figure 5.8, partial phase transformation, which is said to occur during homogenisation of AA3104 [55]. Furthermore, Alexander and Greer also observed partial phase transformation [33]. The joint between the two partially transformed particles is called a duplex interface as mentioned above. Partial transformation is caused/varies due to Si content, as well as homogenisation time and temperature. For example a higher Si content results in a full particle phase transformation.

Furthermore, longer homogenisation times and higher homogenisation temperatures result in a full transformation, granted there is enough Si content. Therefore, if there is a low incidence of partially transformed particles, it means that the transformation is fast. Additionally, a high homogenisation temperature might not necessarily mean full transformation but particle dissolution, hence the correct homogenisation temperature is needed.

5.3 Homogenised microstructure

During homogenisation of AA3104, there is phase transformation, elimination of micro-segregation, redistribution of Mn from solid solution to coarse particles and dispersoids, as well as the dissolution of Mg_2Si particles. Homogenisation results in phase transformation from the β-$Al_6(Fe,Mn)$ to the harder α-$Al_x(Fe,Mn)_3Si_2$ phase particles. This is seen by the increase in α-phase particle VF and corresponding decrease in the β-phase particles within the micrographs. The phase change is indicated by the increase in blue snowflakes on the micrographs in Figure 5.10 (a) to (d) below, compared to the white dots dominating in Figure 5.1. The evidence of phase transformation is shown by the presence of “aluminium spots” within the α-phase particles, these spots indicate eutectoid β-to-α transformation in DC-cast 3XXX alloy [33]. Figure 5.10 (a) and (b) shows that microstructure at the edge contains a greater number of finer particles, with a denser particle distribution compared to the microstructure at the centre in Figure 5.10 (c) and (d). Furthermore, detailed analysis is required to establish which homogenisation treatment between the 560°C/520°C and the 580°C/520°C yields the correct β- to α-phase ratio, shown in Chapter 6.

Figure 5.11 (a) and (b) shows an increase in the Si content within the intermetallic particles, which suggests a phase transformation from the β-phase to the α-phase during homogenisation at 560°C/520°C. This is indicated by the increase in green colour shading within the Si element map, compared to the as-cast condition Si element map that had traces of green in Figure 5.2. Figure 5.11 (b) shows an α-phase particle, indicated by a red arrow,

and a β-phase particle, indicated by a blue arrow, as well as a duplex interface indicating partial phase transformation at the centre of the ingot.

Elemental analysis show that, after homogenisation at 560°C/520°C there is an increase in the α-phase VF of particles. The particles are also identified morphologically. The β-phase particles have a more needle-like shape compared to the α-phase particles that have a Chinese-script-like shape. This is shown in Figure 5.12, where (a) shows a particle containing α-phase circled in black and β-phase circled in red exposed at the grain boundary near the edge of the ingot while (b) shows a α-phase particle circled in black at the centre of the ingot.

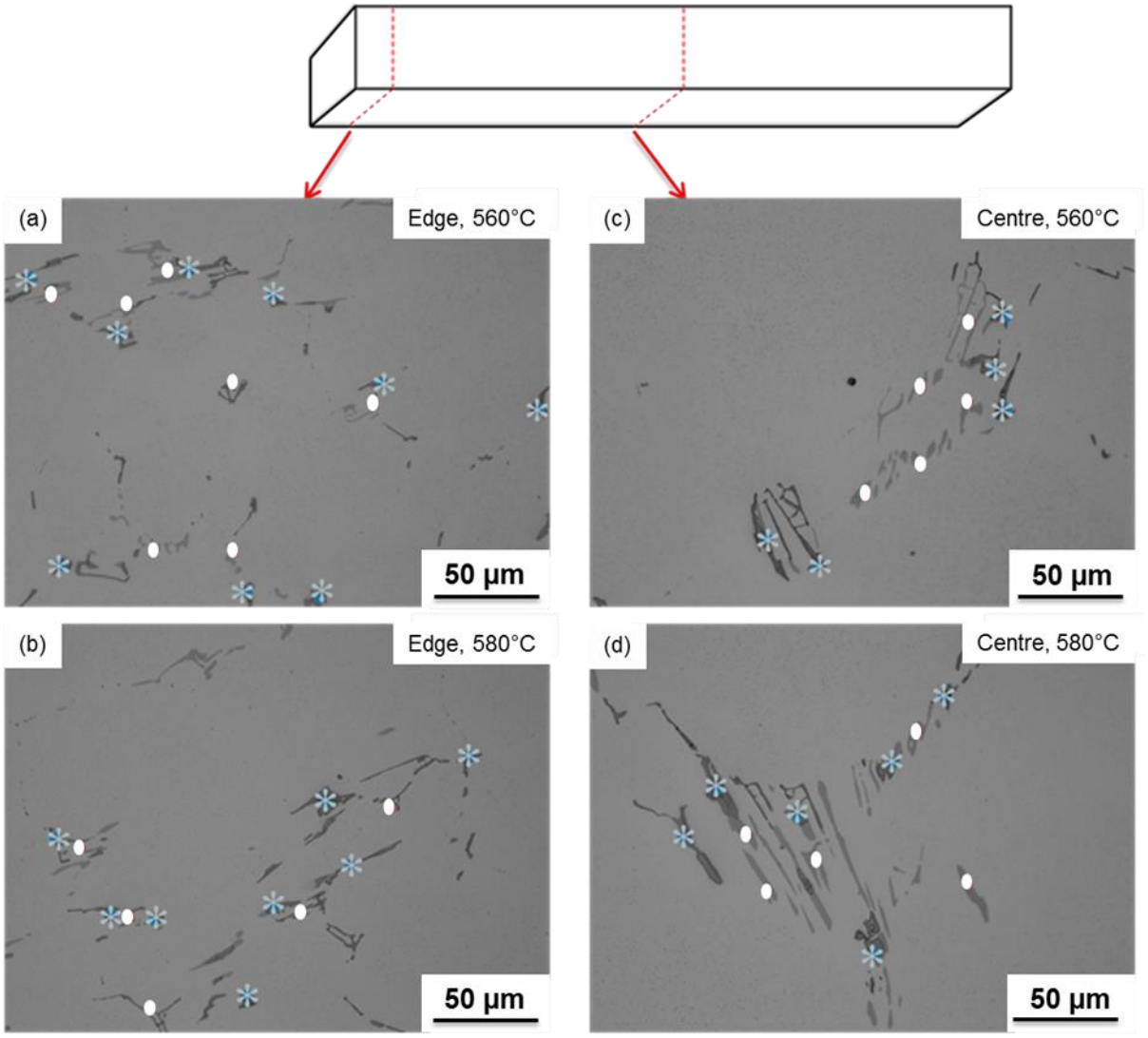

Figure 5.10: Light micrograph of AA3104 showing intermetallic particles near the edge (a) homogenised at 560°C/520°C for 29 hrs, (b) homogenised at 580°C/520°C for 31 hrs, as well as at the centre (c) homogenised at 560°C/520°C for 29 hrs and (d) homogenised at 580°C/520°C for 31 hrs. All etched with 10% H_3PO_4 at 50%.

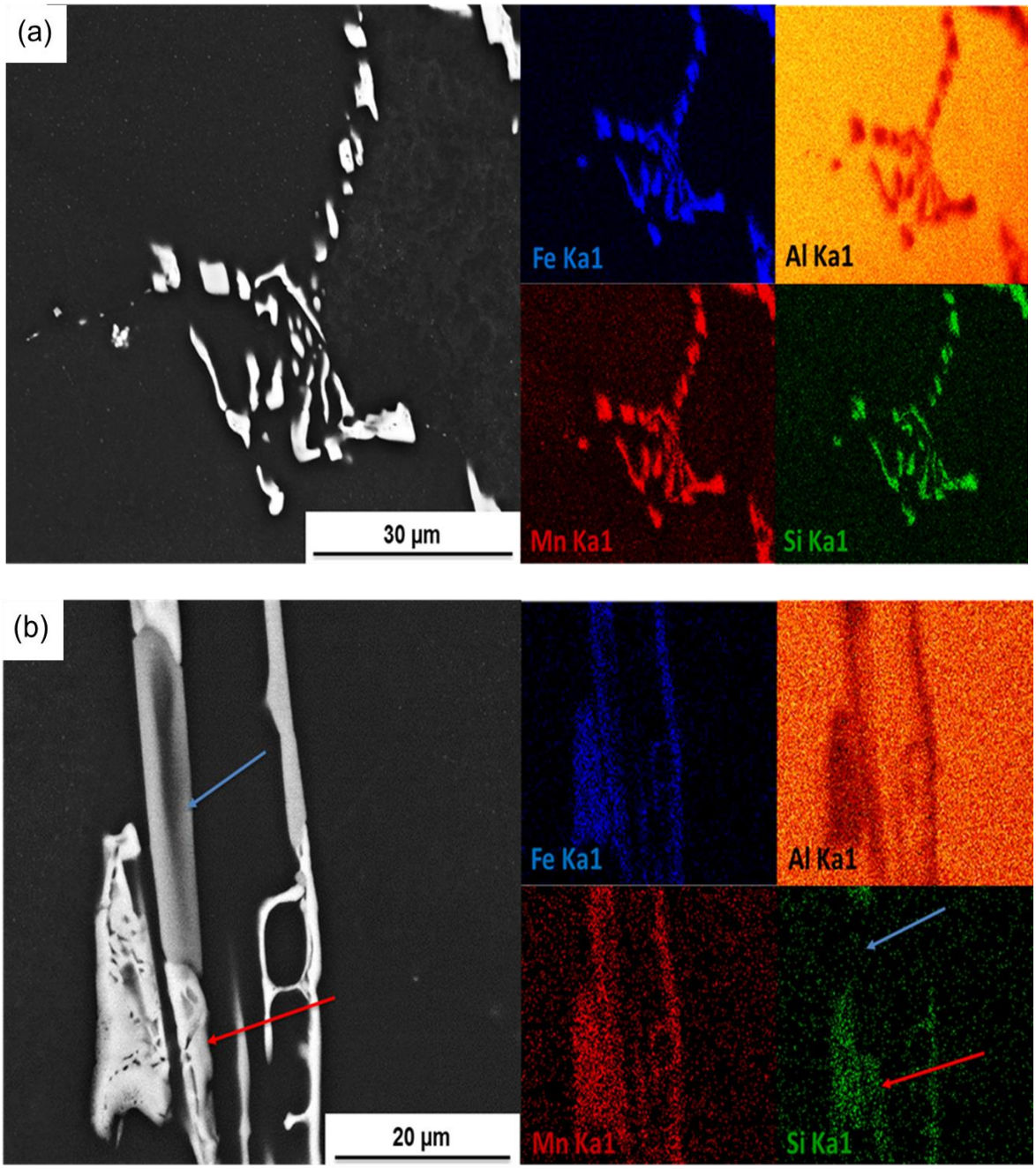

Figure 5.11: SEM Backscatter electron micrographs, coupled with EDS maps, highlighting the major elements present within the intermetallic particles. (a) An α-phase particle near the edge and (b) A duplex interface with α indicated by the red arrow and β indicated by blue arrow at the centre of the ingot, both after homogenisation at 560°C/520°C for 29 hrs.

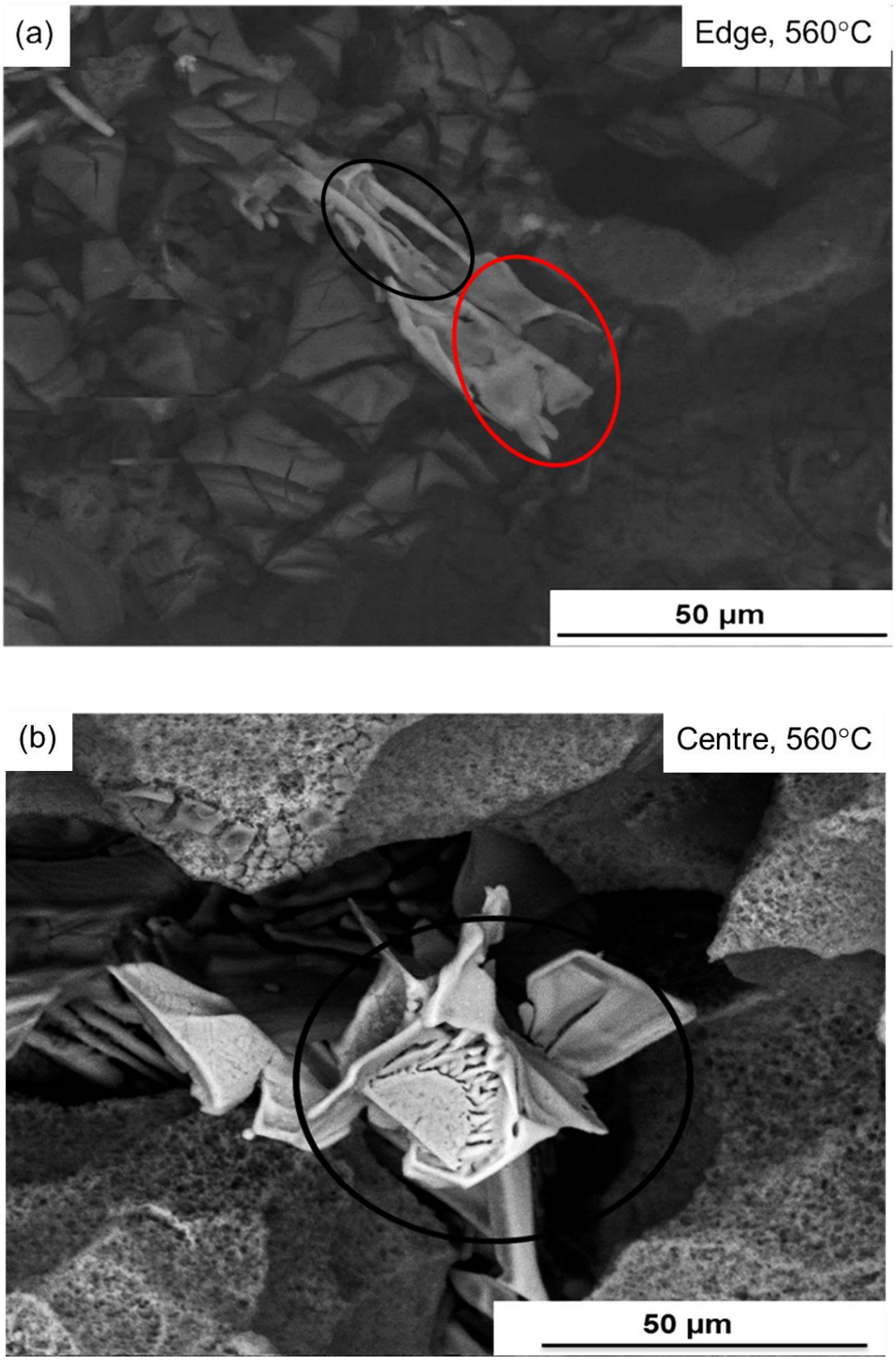

Figure 5.12: SEM Backscatter micrographs of partially dissolved AA3104 specimens (a) showing a particle containing α-phase circled in black and β-phase circled in red exposed at the grain boundary near the edge of the ingot as well as (b) showing a circled α-phase particle at the centre, both after homogenisation at 560°C/520°C for 29 hrs.

Figure 5.13 (a) and (b) shows an increase in the Si content within the intermetallic particles, which then suggests phase transformation from the β-phase to the α-phase during homogenisation at 580°C/520°C. This is also seen by the increase in green colour shading within the Si element map compared to the as-cast condition Si element map that had traces of green in Figure 5.2. The red contours show the β-phase particles which do not contain the Si element, thus there is no green shading that correspond with these particles within the Si map.

After homogenisation at 580°C/520°C there is also an increase in the α-phase VF of the particles, as seen during homogenisation at 560°C/520°C. Furthermore, it is still difficult to identify the intermetallic particles using elemental analysis. However, the particles differ morphologically. The β-phase particles have a more needle-like shape compared to the α-phase particles that have a rosette or Chinese-script-like shape, as seen in Figure 5.14 (a) and (b).

Figure 5.14 (a) shows intermetallic particles exposed at the grain boundary near the edge of the ingot and (b) shows an α particle circled in black and a β particle at the centre, both after homogenisation at 580°C/520°C. Phase quantification on two-dimensional (2-D) microstructural analysis at this stage is inconclusive. Therefore, no comments could be made as to whether the presence of α-phase particles is greater in specimens homogenised at 560°C/520°C or 580°C/520°C. Hence, quantification of the particle phases was conducted using other techniques.

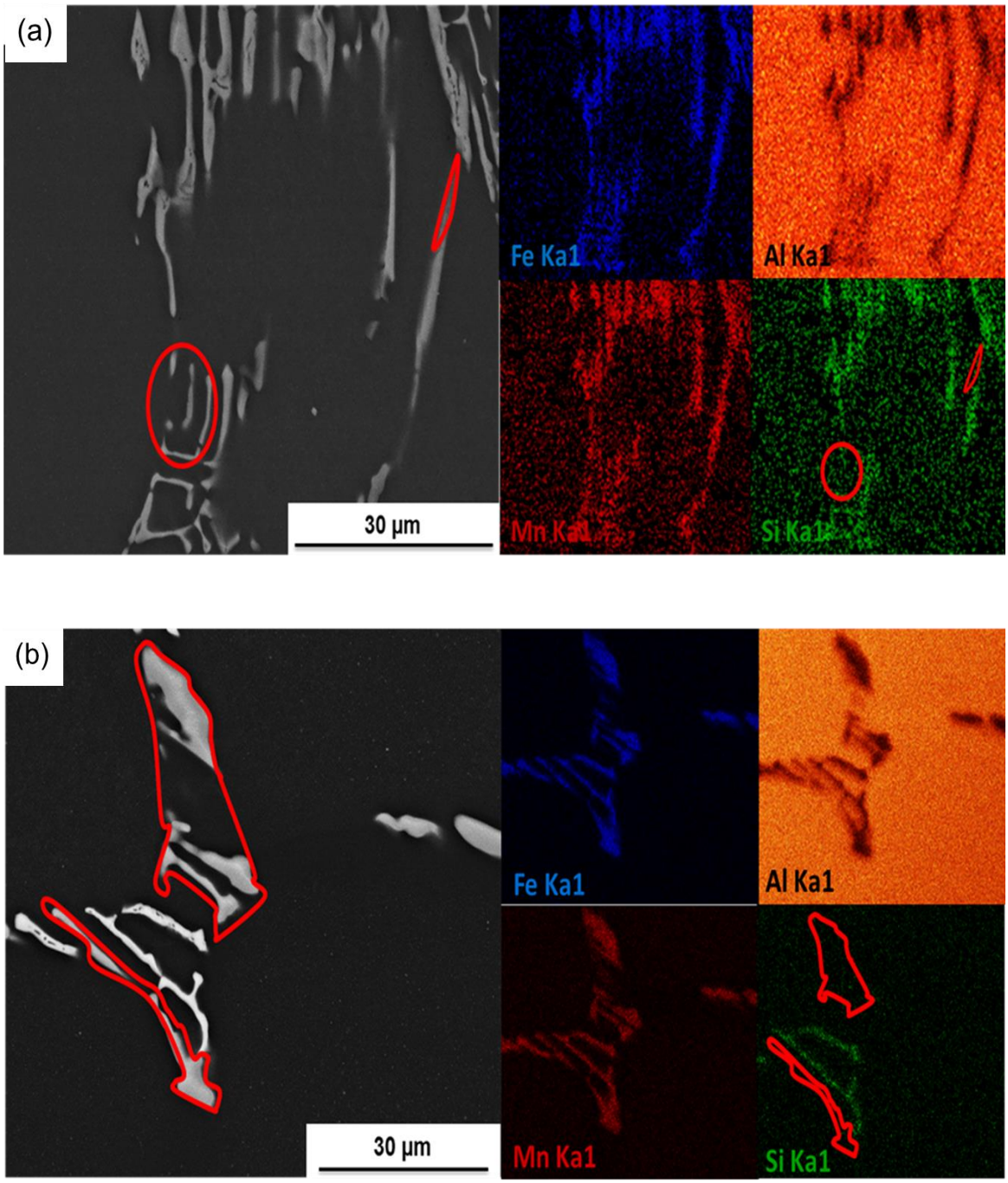

Figure 5.13: SEM Backscatter electron micrographs, coupled with EDS maps, highlighting the major elements present within the cluster of intermetallic particles containing both α-phase particles and β-phase areas. The β-phase areas are contoured in red and identified by their lack of Si. (a) Near the edge and (b) at the centre, both after homogenisation at 580°C/520°C for 31 hrs.

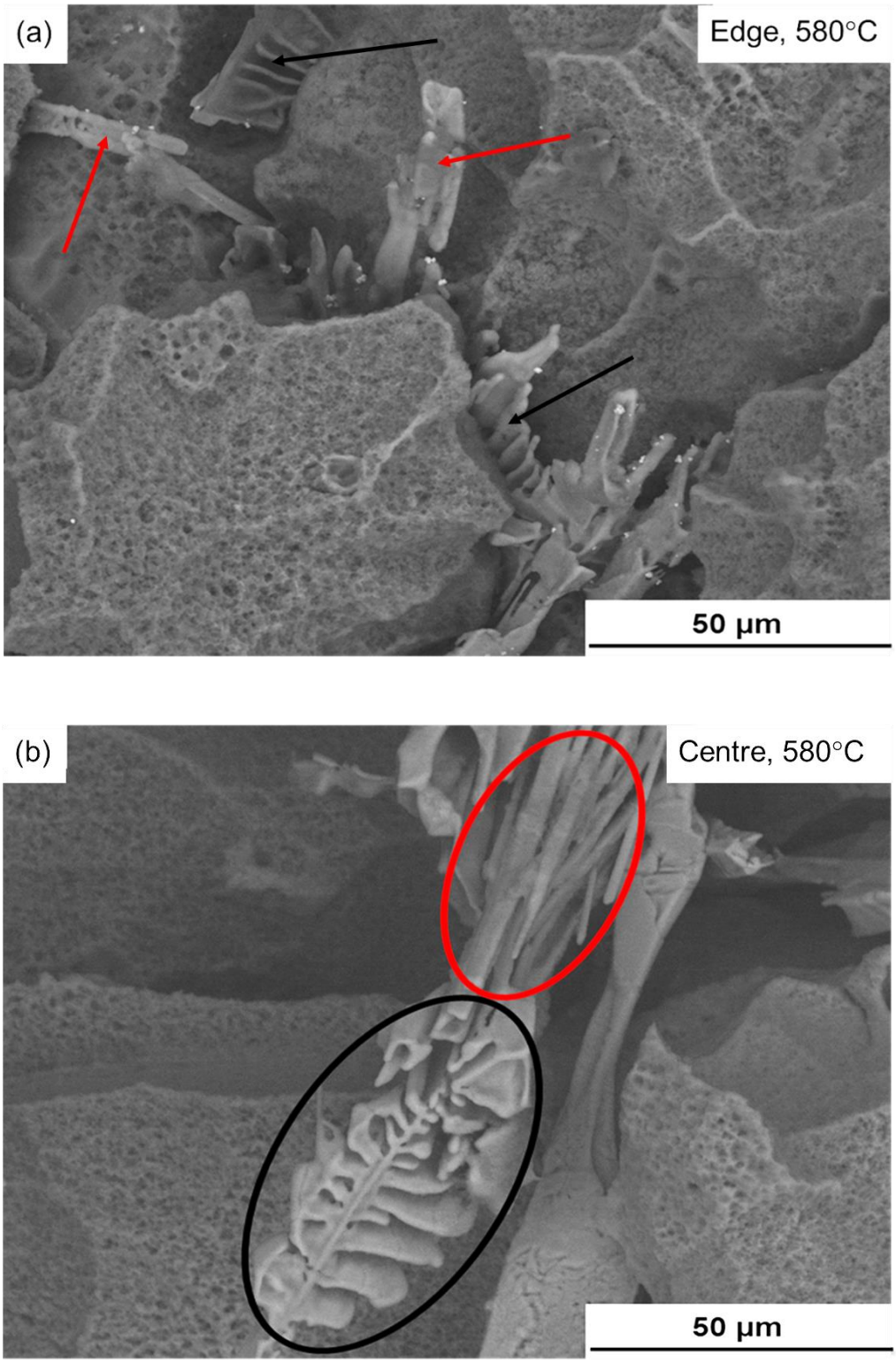

Figure 5.14: SEM Backscatter electron micrographs of partially dissolved AA3104 specimens, (a) contains black arrows showing α-phase particles and red arrows showing β-phase particles exposed at the grain boundary near the edge of the ingot and (b) showing an α particle circled in black and a β particle at the centre circled in red, both after homogenisation at 580°C for 31 hrs.

5.4 Extracted particle characterisation

Particle extraction was achieved using the particle extraction technique based on the SiBut method/technique, where the Al-matrix of the specimen is dissolved in dry butanol within a stainless steel autoclave/pressure vessel, leaving the intermetallic particles unaffected. This results in collected powder intermetallic particles, which can then be easily analysed. The method was used in order to understand the 3-D nature of the intermetallic particles. The sizes of the extracted particles near the ingot edge appeared to be finer than those at the centre, when viewed with the naked eye. After particle extraction was complete, the particles were collected and then analysed using SEM coupled with EDS for morphological and elemental analysis. The particles were then analysed using X-ray diffraction for phase identification and quantification.

5.4.1 Analysis of extracted intermetallic particles using SEM

After intermetallic particle extraction, the size of the extracted particles near the ingot edge appeared to be finer compared to the particles at the centre that appear to be coarser and shinier when viewed with the naked eye. SEM was used to analyse the intermetallic particles in 3-D. Figure 5.15 shows how the extracted intermetallic particles are morphologically different. Figure 5.15 (a) and (b) show multifaceted intermetallic particles. EDS resulted in inconclusive phase identification of these extracted particles. Figure 5.16 (a) shows smaller and fragmented comb-like extracted particles with ripples near the edge while (b) shows larger solid extracted particles with ripples at the centre of the ingot, both after homogenisation at 560°C/520°C for 29 hrs. Figure 5.17 (a) shows fragmented, comb-like and platelet extracted particles near the edge while (b) shows solid/structured Chinese-script-like extracted particles with ripples at the centre of the ingot, both after homogenisation at 580°C/520°C for 31 hrs. Both these figures give an indication of morphological difference between the α-phase (comb-like/rippled) and the β-phase (needle/flake-like) within the extracted particles.

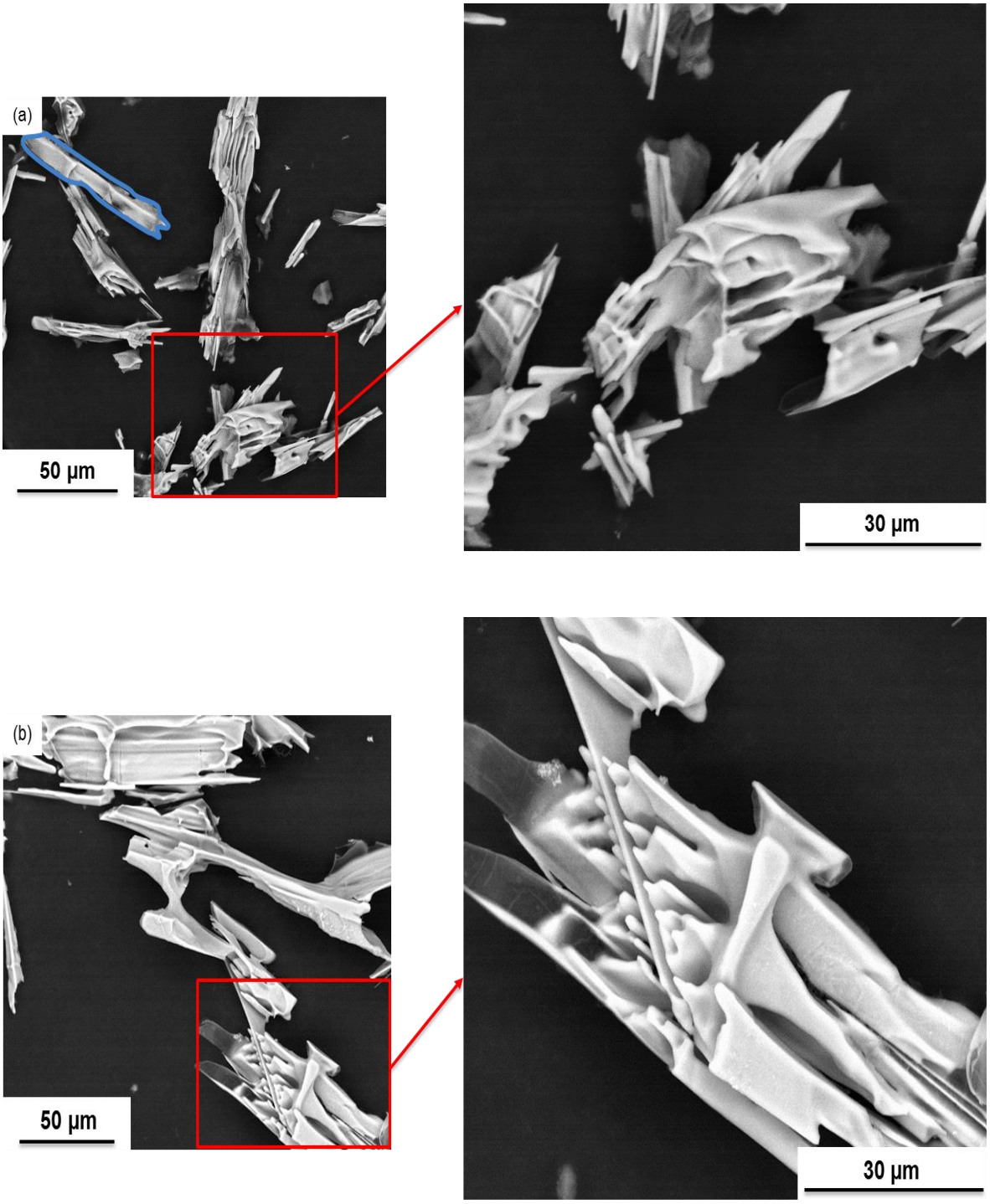

Figure 5.15: SEM Backscatter electron micrographs showing multifaceted (a) smaller fragmented extracted particles near the edge and (b) larger solid extracted particles at the centre of the ingot, both in the as-cast condition.

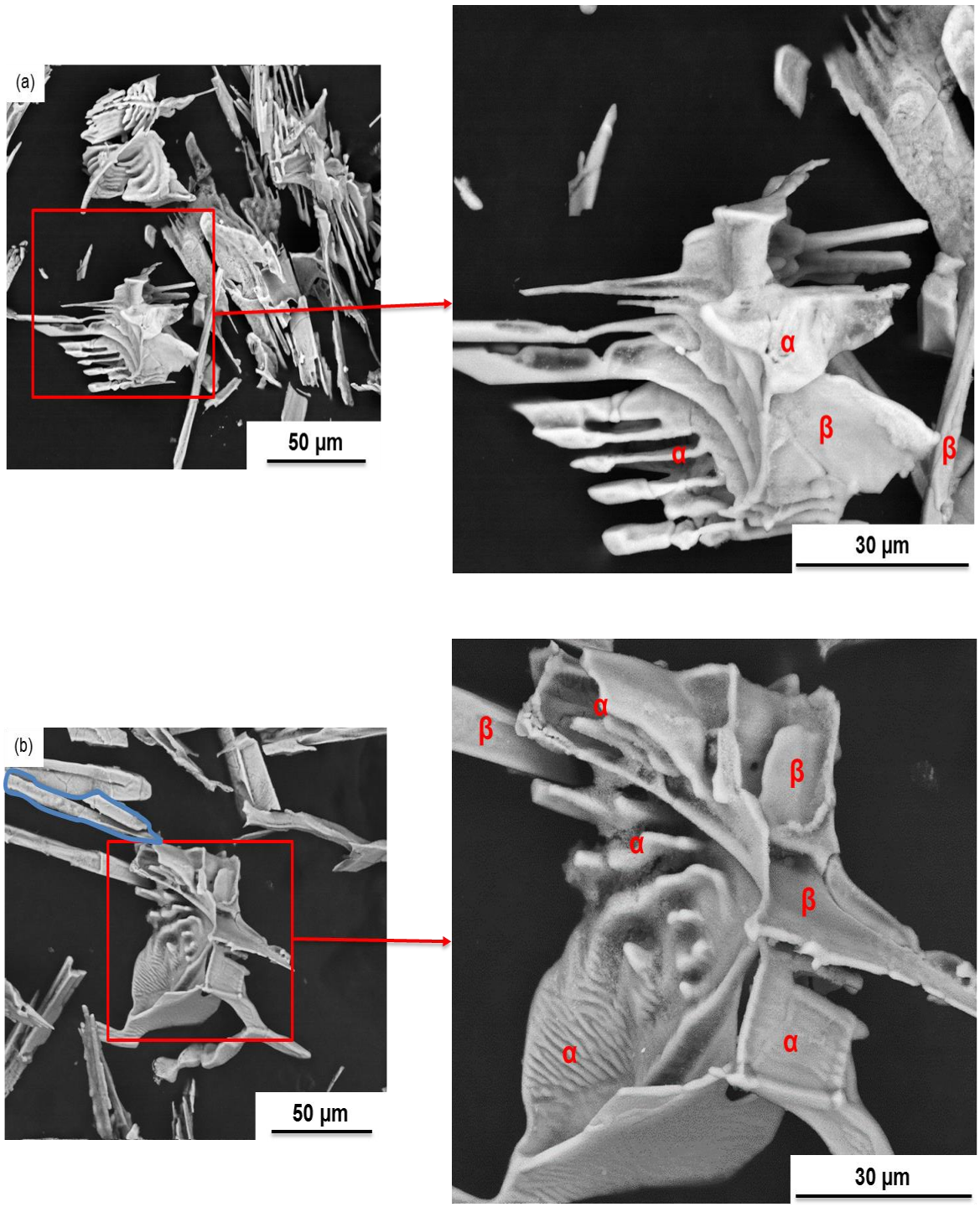

Figure 5.16: SEM Backscatter electron micrographs showing (a) smaller and fragmented comb-like extracted particles with ripples found near the edge of the ingot and (b) larger solid extracted particles with ripples found at the centre of the ingot, both after homogenisation at 560°C/520°C for 29 hrs. (α and β phases indicated in the images).

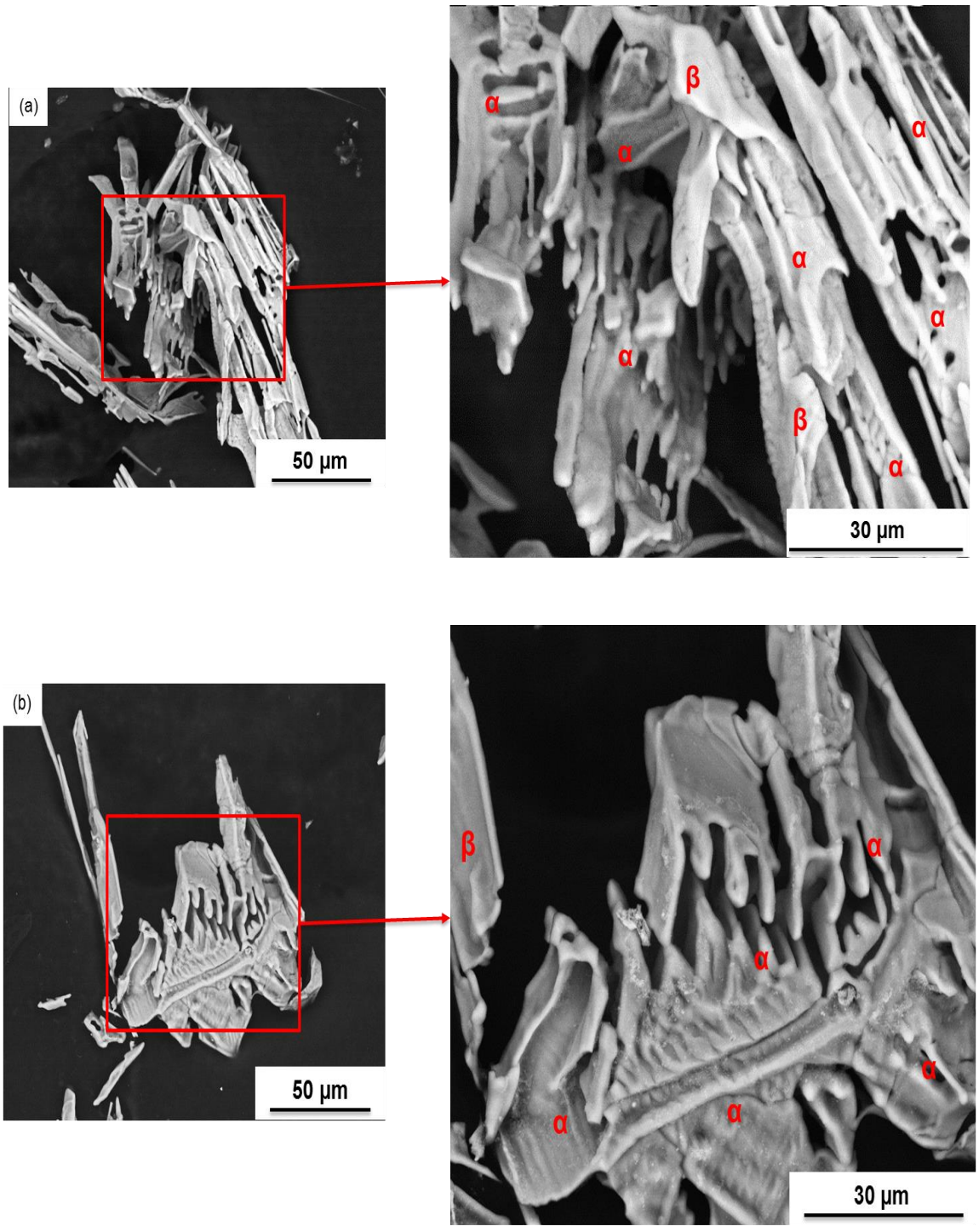

Figure 5.17: SEM Backscatter electron micrographs showing (a) fragmented, comb-like and platelet extracted particles found near the edge of the ingot and (b) solid/structured Chinese-script-like extracted particles with ripples found at the centre of the ingot, both after homogenisation at 580°C/520°C for 31 hrs. (α and β phases indicated in the images).

5.4.2 EDS analysis of extracted intermetallic particles

Elemental analysis, using the SEM coupled with EDS, was conducted on extracted intermetallic particles. The analysis showed that some particles were in α-phase and some were in β-phase. Figure 5.18 shows (a) an SEM Backscatter electron microscopy of specimen near the edge homogenised at 560°C/520°C for 29 hrs indicating β and α-phase within the particles (b) EDS spectrums indicating the presence of Si in α-phase compared to β-phase which helped elementally distinguish between the twi phases.

However, the technique showed errors which are attributed to the extracted particles as well as the topography and electron-particle interaction. EDS analysis indicated that some intermetallic particles contained a higher (Fe,Mn):Si ratio compared to other particles. Nevertheless, phase identification was possible using the presence of Si in α-phase particles (Figure 5.18), together with distinctive morphological differences within the phases (Section 5.1 - 5.3). The errors attributed to topography and particle-electron interaction both near the edge (E) and at the centre (C) of the ingot is shown in Table 5.1. The table shows Fe:Mn ratio as well as Si content with the intermetallic particles. It is seen that the micrographs within figures represented in the table did not contain any detectable Si content on particles that were morphologically distinguished as α-phase. The SEM with EDS setup information indicates variation in the working distance, thus a variation in the (Fe,Mn):Si ratio.

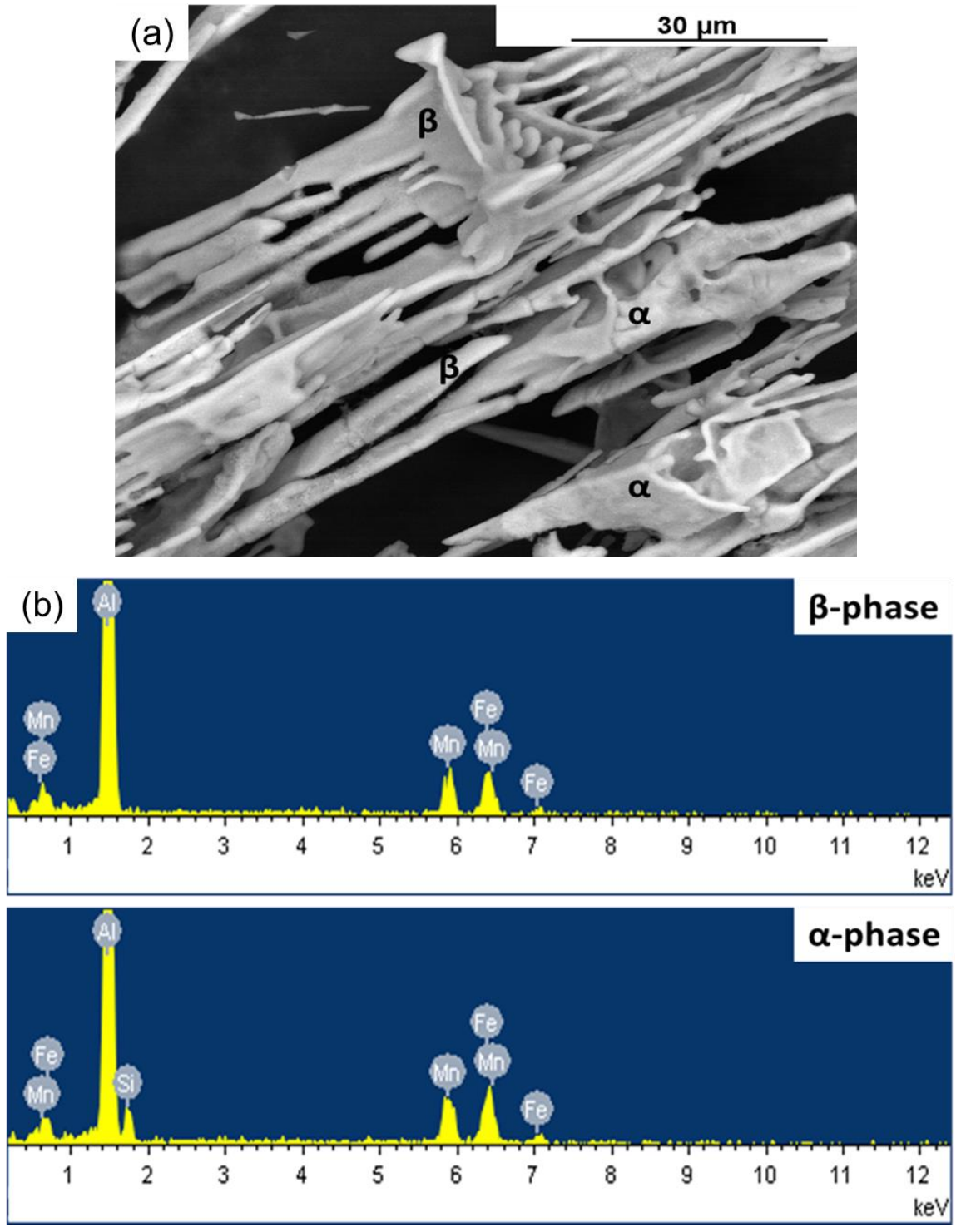

Figure 5.18: Showing (a) SEM Backscatter electron microscopy of specimen near the edge homogenised at 560°C/520°C for 29 hrs indicating β and α-phase within the particles (b) EDS spectrums indicating the presence of Si in α-phase compared to β-phase.

Table 5.1: Showing the variation of (Fe,Mn):Si ratio in EDS results corresponding to extracted particle micrographs in Figure 5.15, Figure 5.16 and Figure 5.17.

Sample/Condition	Position	Spot size (µm)	Working distance (WD) (mm)	Fe:Mn ratio within particles	Si content within particle (wt%)
As-cast, E	Figure 5.15 (a): 1	3.0	6.2	4:2	None
	Figure 5.15 (a): 2			5:3	None
As-cast, C	Figure 5.15 (b): 1	3.0	5.1	8:6	None
	Figure 5.15 (b): 2			8:6	1
Homogenised at 560°C/520°C for 29 hrs, E	Figure 5.16 (a): 1	3.0	6.0	4:3	2
	Figure 5.16 (a): 2			6:5	None
Homogenised at 560°C/520°C for 29 hrs, C	Figure 5.16 (b): 1	3.0	4.9	4:3	None
	Figure 5.16 (b): 2			4:4	1
Homogenised at 580°C/520°C for 31 hrs, E	Figure 5.17 (a): 1	3.0	6.0	3:3	2
	Figure 5.17 (a): 2			3:3	2
Homogenised at 580°C/520°C for 31 hrs, C	Figure 5.17 (b): 1	3.5	4.7	2:2	None
	Figure 5.17 (b): 2			1:1	1

5.5 Thermodynamic calculations using JMatPro

Thermodynamic calculation was conducted using JMatPro to predict the phases that are to be expected within the AA3104 alloy during step homogenisation. These phases are expected to be present within the matrix, dispersoids within the matrix, as well as intermetallic particles along the grain and cell boundaries [18]. Figure 5.19 shows that phases Al_3Mg_2, $Al_3M\_DO_{22}$, T_AlCuMgZn, S_Al_2CuMg, Mg_2Si, Al_6Mn (β) and alpha-$Al_x(Fe,Mn)_3Si_2$ (α) are present within the material during homogenisation. The graph also shows the amount of phases in wt% that are to be expected as temperature varies. Crystallographic information of the phases was collected. No information on $Al_3M\_DO_{22}$ was found in literature, which is indifferent as the phase's wt% is extremely small. Therefore, phase identification and quantification using XRD was conducted based on the predicted phases that had crystallographic information available.

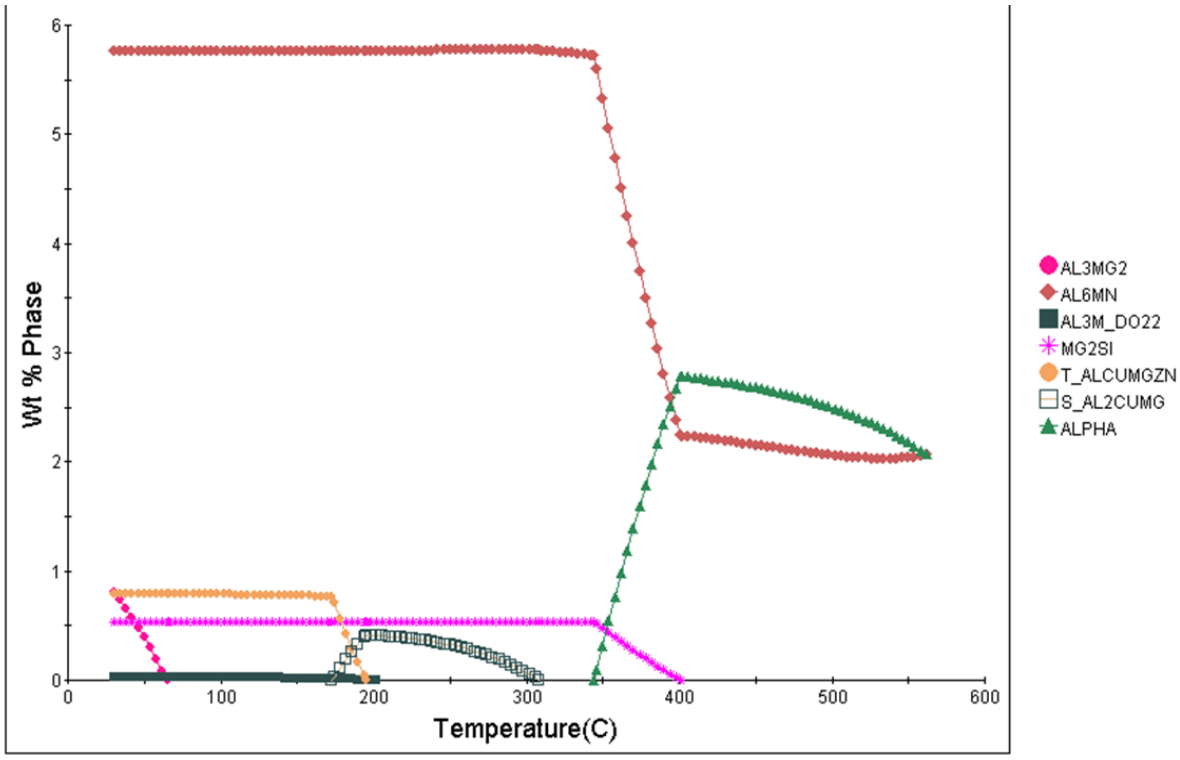

Figure 5.19: Graph showing wt% of phases present within AA3104 as temperature varies.

5.6 Intermetallic phase identification using XRD

Figure 5.20, Figure 5.21 and Figure 5.22 below show the different XRD patterns produced by samples in the as-cast condition and homogenisation condition, both near the edge and at the centre of the AA3104 ingot. These patterns were used for particle phase identification as well as quantification. Literature indicates α-$Al_x(Fe,Mn)_3Si_2$ phase major peaks ranging between 23-27, 36-46 and 60-64 degrees. While the β-$Al_6(Fe,Mn)$ phase major peaks ranges between 23-75 degrees [56, 30, 31, 47 and 57 - 66]. Figure 5.20 shows the phases present within the material after homogenisation, with α and β being the major particle phases. While the other phases (Mg_2Si, Al_3Mg_2, S_Al_2CuMg and T_AlCuMgZn) represent dispersoids. The phases identified agree with 2-D microstructural analysis as well as thermodynamic calculation.

Figure 5.21 and Figure 5.22 shows patterns indicating dotted lines highlighting strong β-phase peaks in the as-cast condition, as well as yellow triangles, that tend to disappear in the homogenised condition. It is also seen that there are α-phase peaks, green circles, which are short and narrow in the as-cast condition but tend to be taller and broader after homogenisation. The peaks also suggest the presence of α-phase particles in the as-cast condition. The decrease in β-phase peaks and increase in α-phase peaks shows that phase transformation occurred within this material during homogenisation. The absence of Mg_2Si in the as-cast condition is not unusual in XRD patterns due to the phase being present below the detection limit of the XRD [46]. However, a trace of this phase is seen during XRD analysis as seen in Figure 5.20.

Further major phases' peak comparison within the XRD patterns show that as-cast samples near the edge contain a higher intensity of peaks compared to peaks at the centre, as seen in Figure 5.21 and Figure 5.22. This suggests that samples near the edge contain more phase particles than samples at the centre. Homogenised samples at the centre show a higher intensity of α-phase peaks compared to samples near the edge of the ingot. This suggests that samples at the centre contain a higher β- to α-phase ratio compared to samples near the edge of the ingot. However, further phase quantification analysis using the Rietveld method is used to conclusively identify which location within the ingot as well as which homogenisation treatment yields the desired β- to α-phase ratio section 6.3.

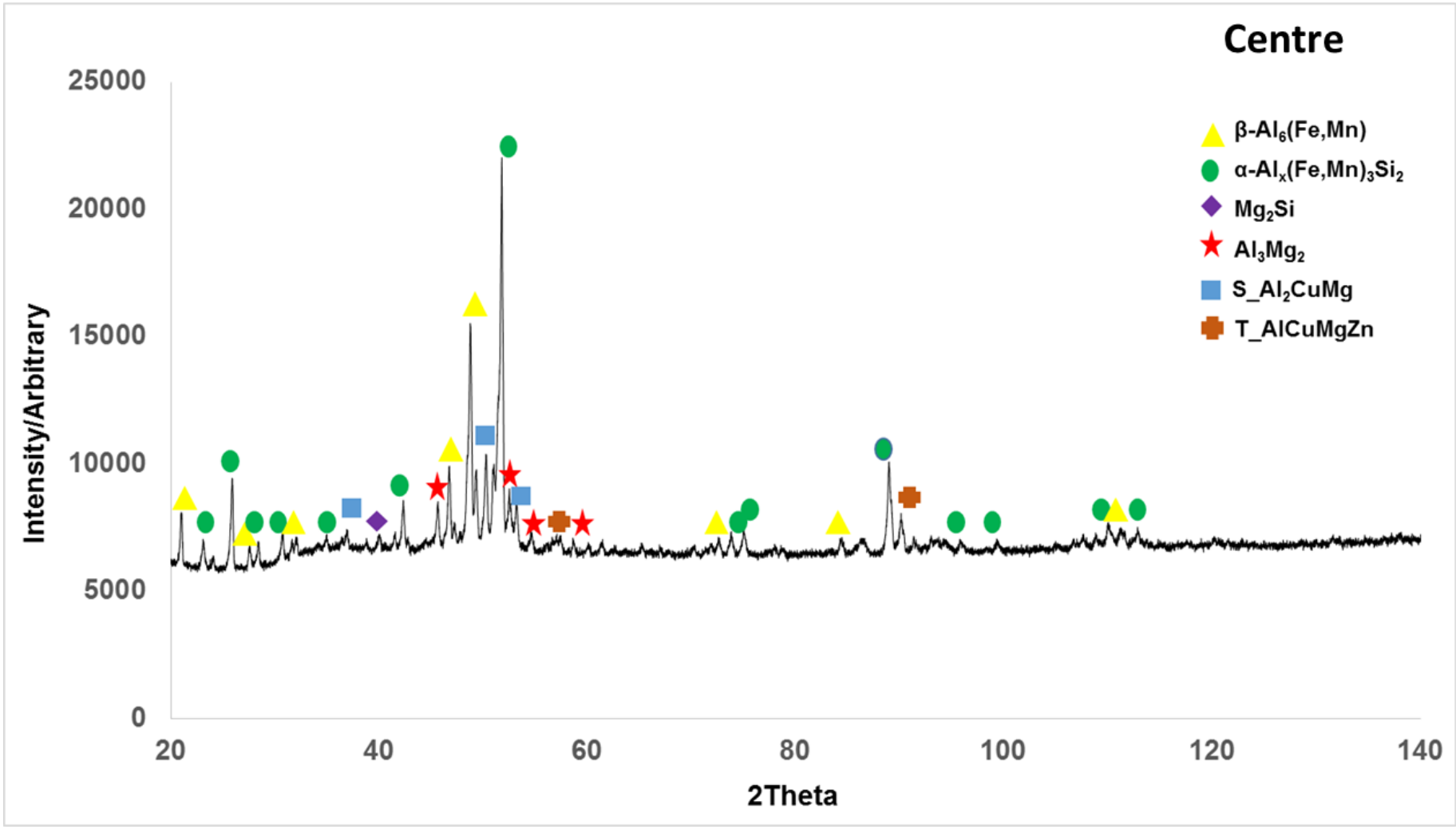

Figure 5.20: XRD pattern showing phases present within the centre of AA3104 ingot homogenised at 580°C/520°C for 31 hrs, with α (green circle) and β (yellow triangle) as the major phases, as well as traces of the other phases.

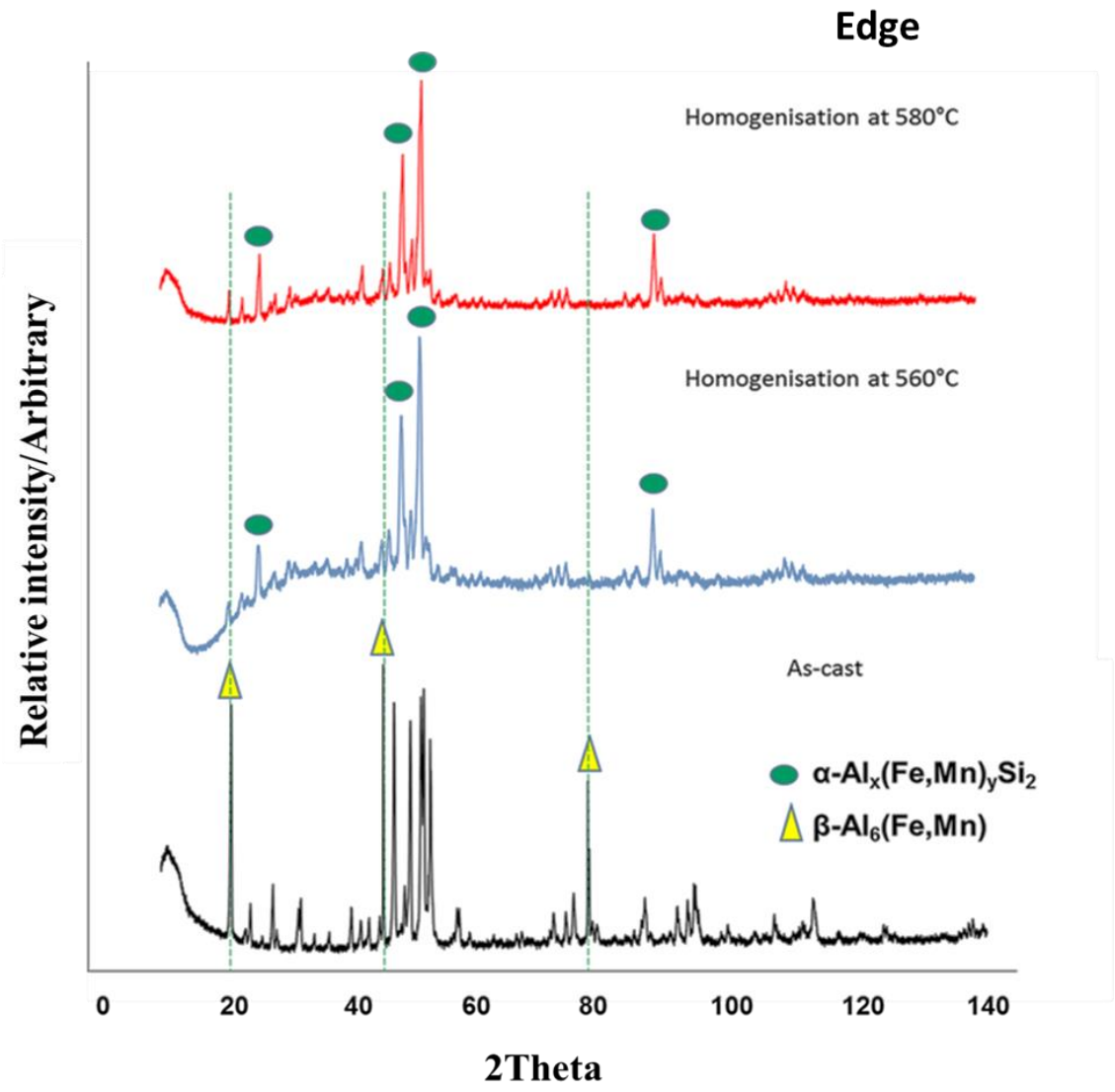

Figure 5.21: XRD pattern showing β-phase in yellow triangles and α-phase in green circles as major phases present within extracted particles in the as-cast condition and after homogenisation.

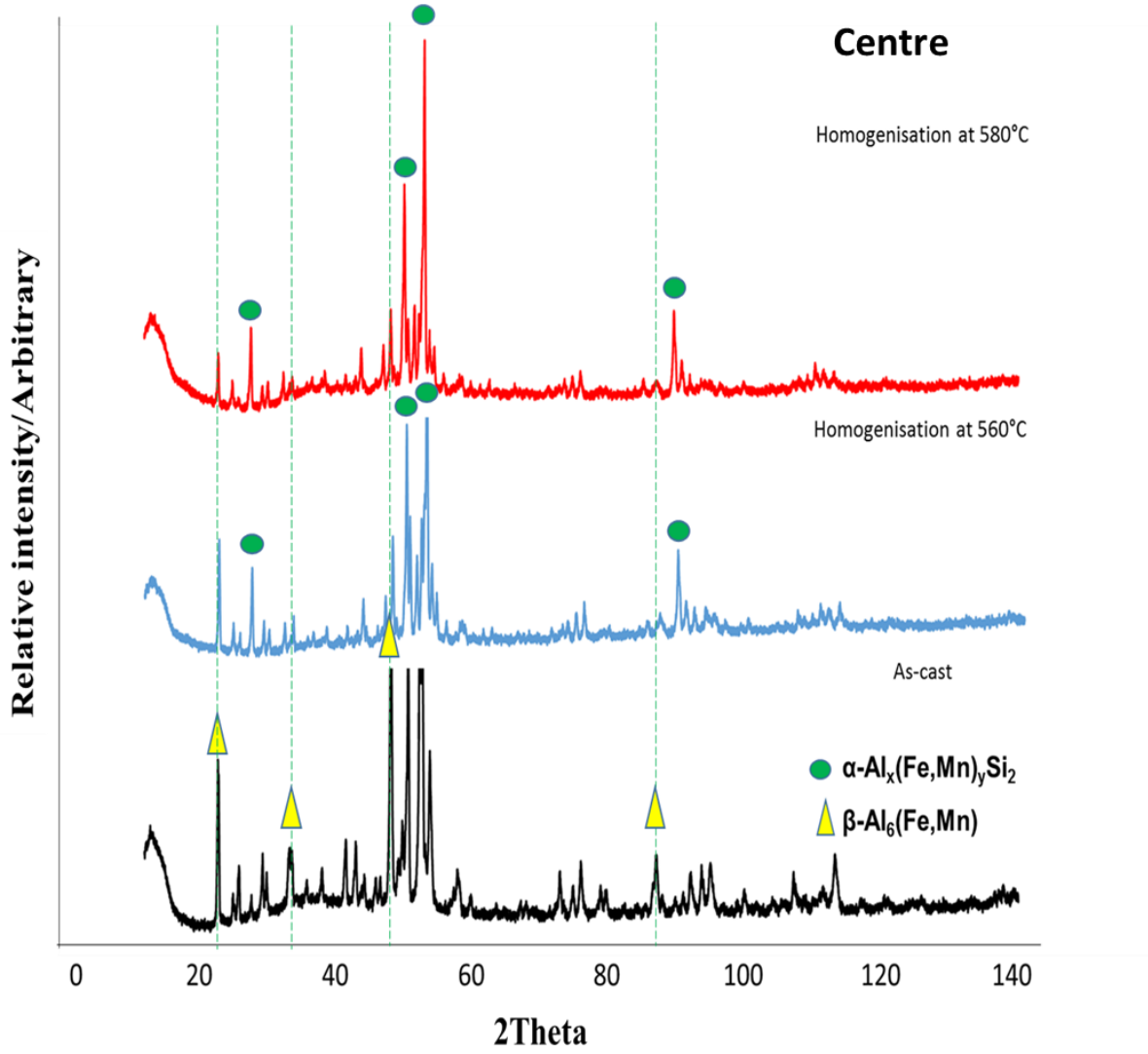

Figure 5.22: XRD pattern showing β-phase in yellow triangles and α-phase in green circles as major phases present within extracted particles in the as-cast condition and after homogenisation.

5.7 Summary

5.7.1 Microstructural analysis before and after homogenisation

Microstructural analysis of both solid specimen and extracted particles show that there are more particles near the edge which are smaller and fragmented when compared to particles at the centre, where there appear to be fewer, coarser and more united/solid particles. Figure 5.23 shows how α and β are morphologically distinguishable using microscopy. The β-phase particles contain a needle-like/flake-like shape and the α-phase particles contain a non-geometric/comb-like/Chinese-script-like shape as seen in Figure 5.23. The Light microscopy images in Figure 5.23 (a), shows α-phase as dark grey and β-phase as grey. SEM images in Figure 5.23 (b) show the α-phase as light grey and the β-phase as grey. Additionally, Figure 5.23 (c) shows extracted intermetallic particles with no phase contrast distinction but morphological difference.

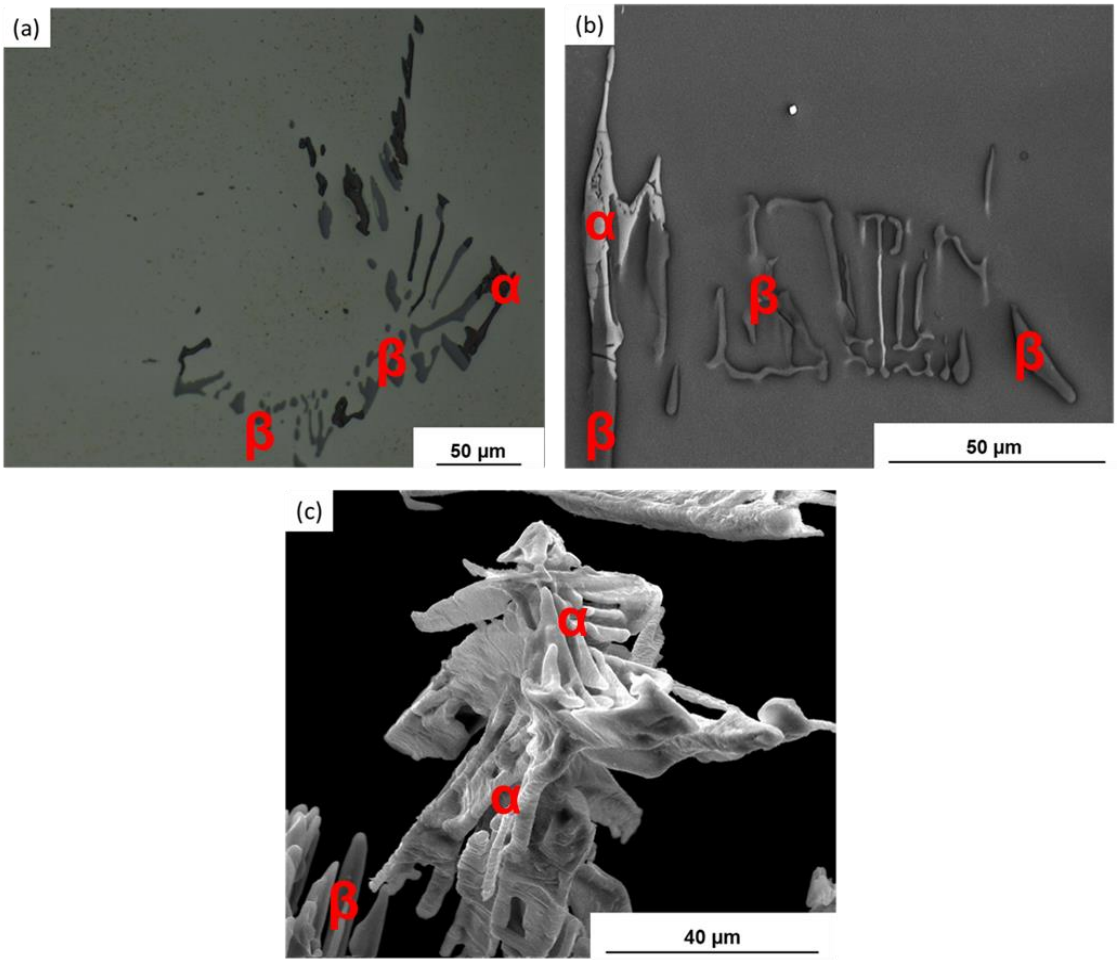

Figure 5.23: Morphological differences between α-and β-phase intermetallic particles seen under (a) Light micrograph of solid specimen, (b) SEM Secondary electron micrograph of solid specimen and (c) SEM Secondary electron micrograph of extracted particles, all from AA3104 specimen homogenised at 580°C/520°C for 31 hrs.

Furthermore, it is observed that as-cast specimens contain β as the predominant phase and traces of the α-phase. Whereas, homogenised specimens shows an increase in α-phase and a decrease in β-phase particles which indicates phase transformation through Si diffusion.

EDS was used to elementally distinguish between α-and β-phase intermetallic particles. Figure 5.24 (a) and (b) confirms that the α-phase, contoured in red, contains Si and the β-phase, not contoured, does not. Thus as-cast specimens [Figure 5.24 (a)] show traces of Si content and homogenised specimens [Figure 5.24 (b)] shows bulk Si present. EDS was also used to distinguish between the two phases, within the extracted particles. However, results were inconclusive due to topographical errors.

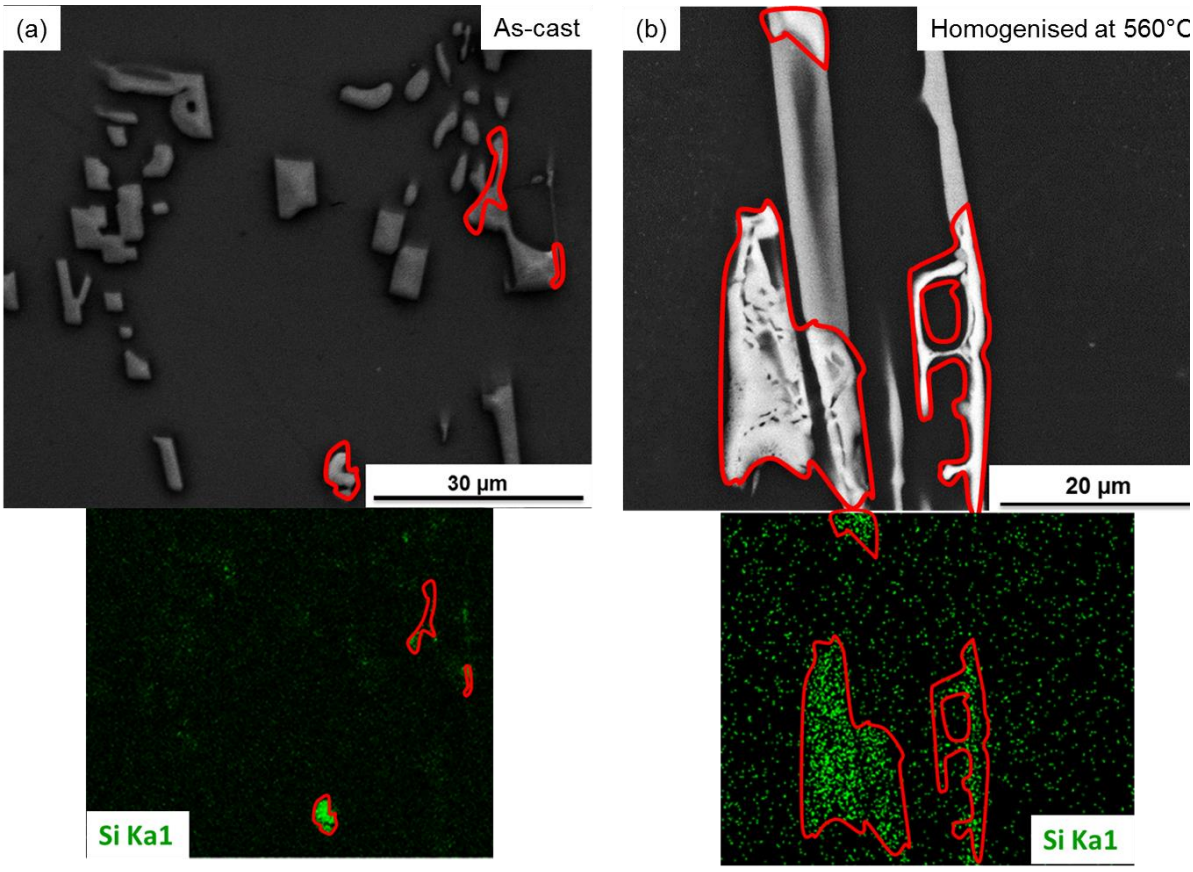

Figure 5.24: SEM micrographs with EDS maps showing the presence of Si within the α-phase particles contoured in red and the absence of Si within the β-phase particles in (a) as-cast specimen and (b) homogenised at 560°C/520°C for 29 hrs specimen.

5.7.2 XRD and Thermodynamic analysis before and after homogenisation

XRD analysis wih the help of JMatPro software was used to predict, identify and distinguish the phases present within AA3104 before and after homogenisation. The techniques shows that Al_3Mg_2, T_AlCuMgZn, S_Al_2CuMg, Mg_2Si, Al_6Mn (β) and alpha-$Al_x(Fe,Mn)_3Si_2$ (α) are the present phase within AA3104 both after homogenisation at 560°C/520°C and 580°C/520°C as seen in Figure 5.19 and Figure 5.20. Where α and β are the major particle phases and the rest are the dispersoid phases. The phases identified also agree with 2-D microstructural analysis.

XRD pattern phase peak comparison shows that as-cast samples near the edge contain high intensity peaks compared to peaks at the centre. This suggests that samples near the edge contain a greater number of phase particles than samples at the centre. Homogenised samples at the centre show stronger α-phase peaks compared to samples near the edge of the ingot, suggesting that samples at the centre contain a higher β- to α-phase ratio compared to samples near the edge of the ingot. However, further phase quantification analysis using the Rietveld method is used to conclusively identify which location within the ingot as well as which homogenisation treatment yields the desired β- to α-phase ratio.

6 RESULTS AND DISCUSSION: MICROSTRUCTURAL EVOLUTION OF AA3104 QUANTITATIVE ANALYSIS

6.1 Image analysis

6.1.1 ImageJ thresholding results

ImageJ was used to threshold light micrograph images according to the image greyscale contrast. The greyscale spectrum describes an incremental range from zero, representing black, to 255, representing white. Firstly, the thresholding values corresponding to the different particle greyscale within the micrographs was estimated. After that the thresholding average value for each specimen was estimated and used to estimate particle VF using MATLAB. It is important to note that the thresholding values differ according to the microscope settings, however this should not make much difference on the intermetallic particle VF estimated. For example, analysis three, four and five in Appendix 2 show higher thresholding values of 163-178 for overall intermetallic particles, 94-138 for α-phase and 24-40 for Mg_2Si phase. While analysis one and two have lower values of 110-115 for overall intermetallic particles, 70-91 for α-phase and 16-30 for Mg_2Si phase. This can be attributed to the variation in the image capture condition settings as well as specimen conditions.

The tables in Appendix 2 show that the different intermetallic particles fall within different values on the greyscale range. The intermetallic particles are in different contrast to the matrix, as well as the α-phase, β-phase and Mg_2Si particles being dark grey, light grey and black respectively. The tables also shows that the intermetallic particles in the as-cast condition are darker than the intermetallic particles in the homogenised condition.

6.1.2 Errors associated with image analysis

Image analysis contains errors that accumulate due to how the morphology of the microstructures evolves after homogenisation. The first error that is observed is due to the presence of dispersoids within the matrix that are of the same greyscale contrast as the intermetallic particles. These dispersoids within the matrix are exposed during etching. This error occurs more on homogenised specimens from the centre of the ingot. This is because the microstructural features appear to be bigger/coarser at the centre compared to the ones near the edge of the ingot, thus resulting in a larger contribution to the particle VF. The presence of these dispersoids then results in a variation of higher and lower β- and α-phase fractions respectively within the estimated particle VF.

Figure 6.1 shows images highlighting errors that emerge when thresholding micrograph images due to the presence/exposure of dispersoids within the matrix. Figure 6.1 (a) shows fewer dispersoids exposed near the ingot edge and (b) shows a greater number of dispersoids exposed at the centre of the ingot. The dispersoids within the matrix are thresholded, along with the other particles.

Specimens near the edge contain a greater number of smaller and fragmented intermetallic particles, seen in Figure 6.2 (a), compared to the centre, which contains fewer, coarser and united intermetallic particles, seen in Figure 6.2 (b). One would expect errors to emerge near the edge as there would be numerous sources of error compared to the centre that has fewer source of error due to the number of particles within the microstructure. However, this is not the case. Particles near the edge are smaller and fragmented however, they have more regular shape than particles at the centre. Thus error is reduced.

The surface topography of the intermetallic particles does not give rise to any errors. Figure 6.3 shows the topographical difference between the two phases, where (a) shows a polarised light micrograph that indicates flat β- and α-phase particles, while (b) shows Nomarski micrograph indicating the topography of the β-phase particles “coming out” of the page and α-phase particles “going into” the page. One would expect the harder α-phase particles to have shadows outlining them thus also forming part of the thresholded area resulting in overestimated particle VF and particle phase fraction.

Lastly, error is observed due to the presence of Al-spots within the α-phase particles. Figure 6.4 (a) shows a light micrograph containing Al-spots (A and B) and (b) contains light micrograph image when thresholding included Al-spots (A and B) within the α-phase particles, as well as over-thresholding of particles (seen in C).The error arises when the Al-spots are small thus containing the same greyscale contrast as either β-phase particles or α-phase particles instead of that of the matrix. This then also results in over/underestimation of intermetallic particle VF, as well as particle phase fraction.

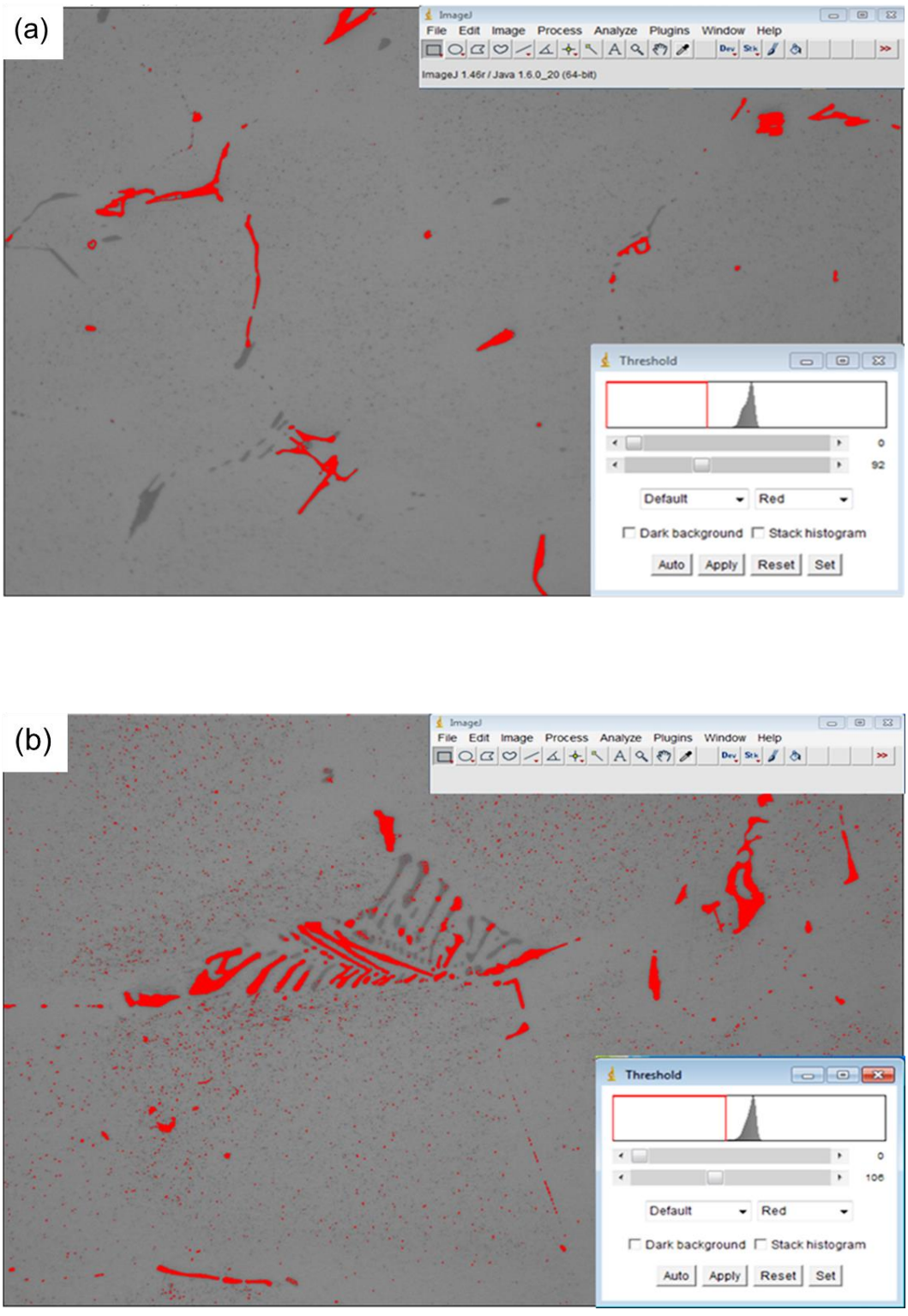

Figure 6.1: Light micrograph images showing errors that emerge during thresholding due to the presence/exposure of dispersoids within the matrix. (a) Shows fewer dispersoids exposed near the ingot edge and (b) shows fewer number of dispersoids exposed at the centre of the ingot.

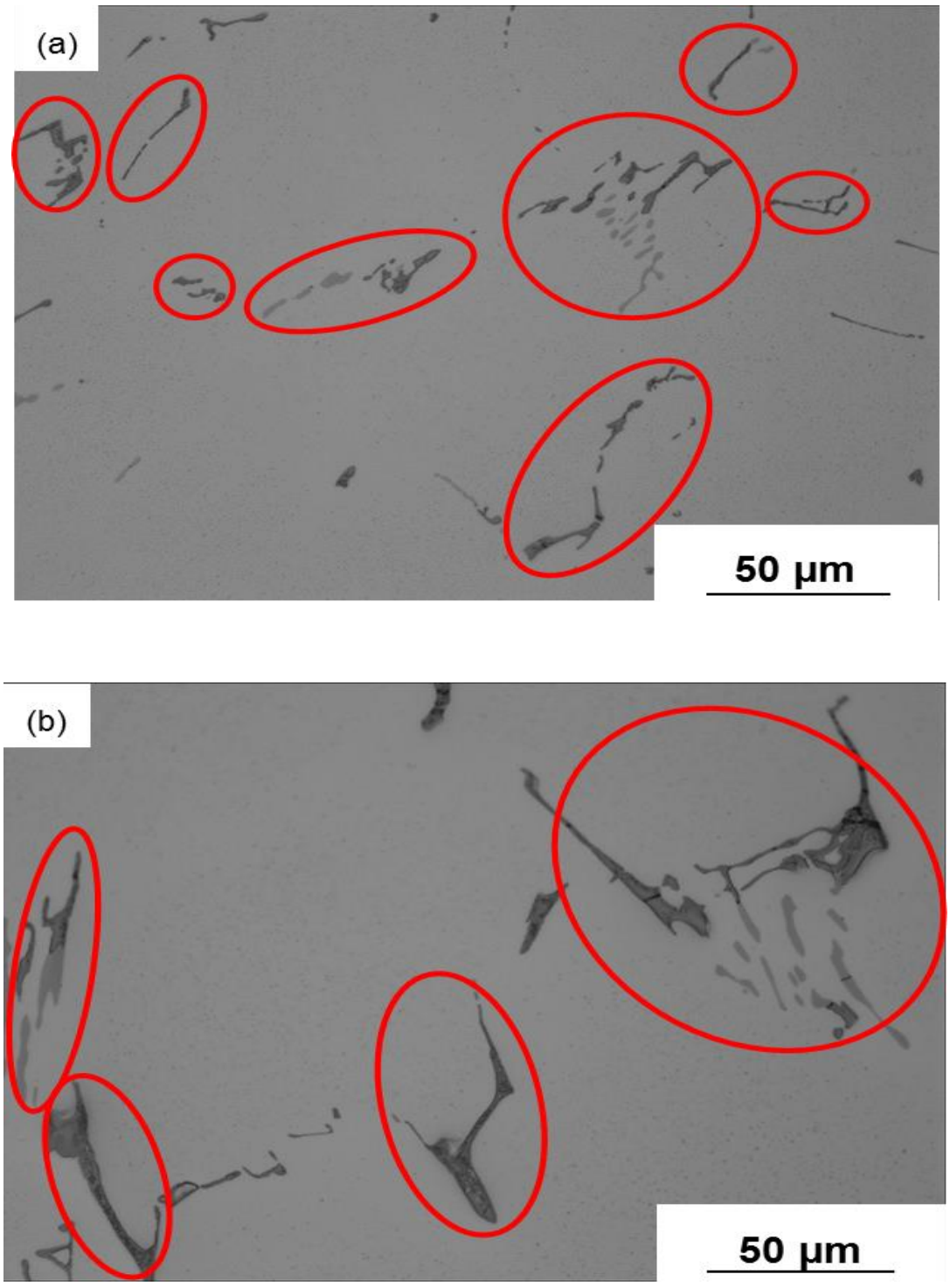

Figure 6.2: Light micrographs showing particle distribution within the microstructure after homogenisation. (a) Contains a greater number of smaller particles near the edge compare to (b) which contains fewer and coarser particles at the centre.

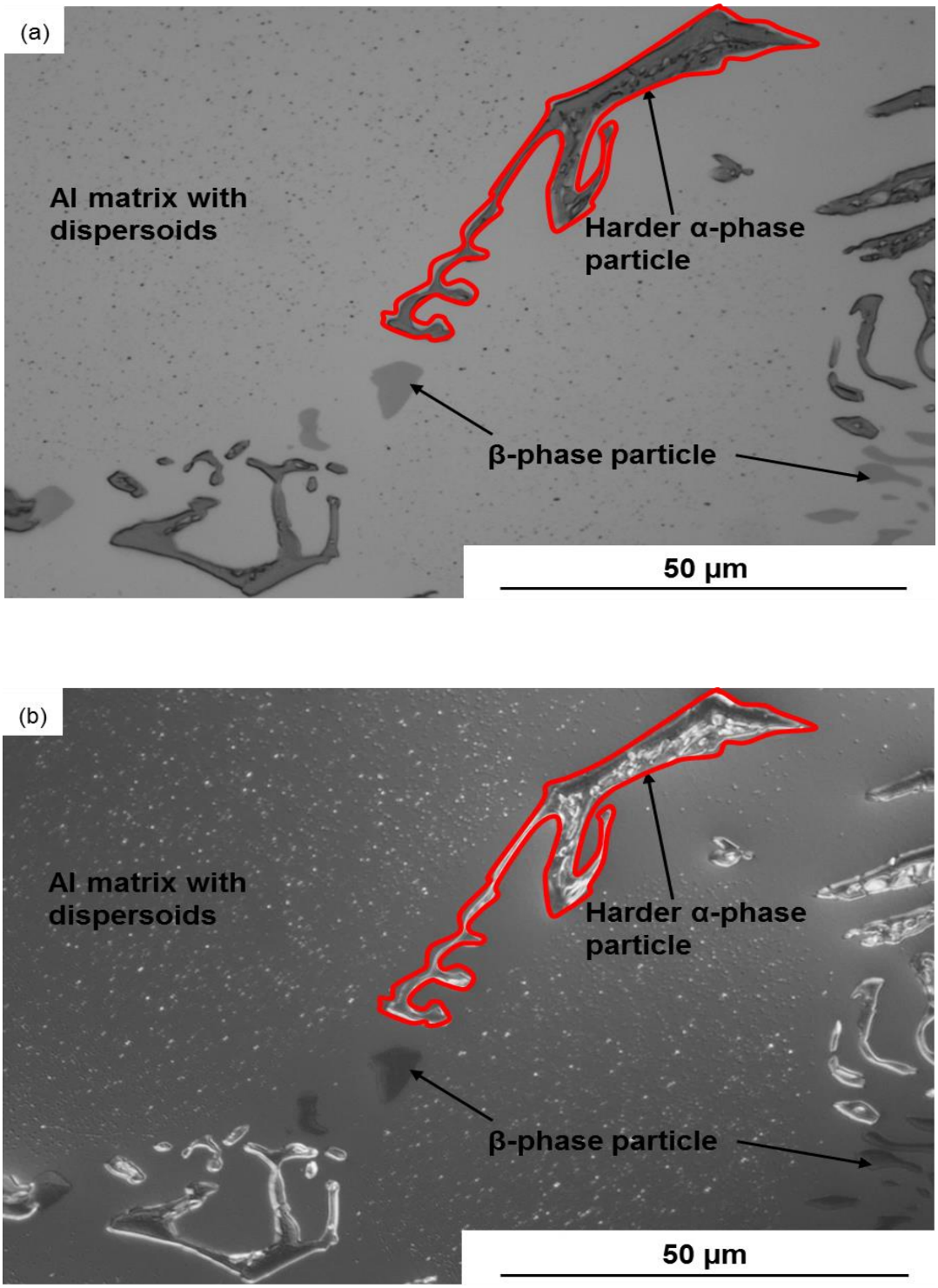

Figure 6.3: (a) Shows a polarised light micrograph indicating the minimal topographical differences between the β- and α-phase particles. (b) Shows topographical effects created when using Nomarski lens, where the α-phase particles are ‘coming out of’ the page and β-phase particles are ‘going into’ the page.

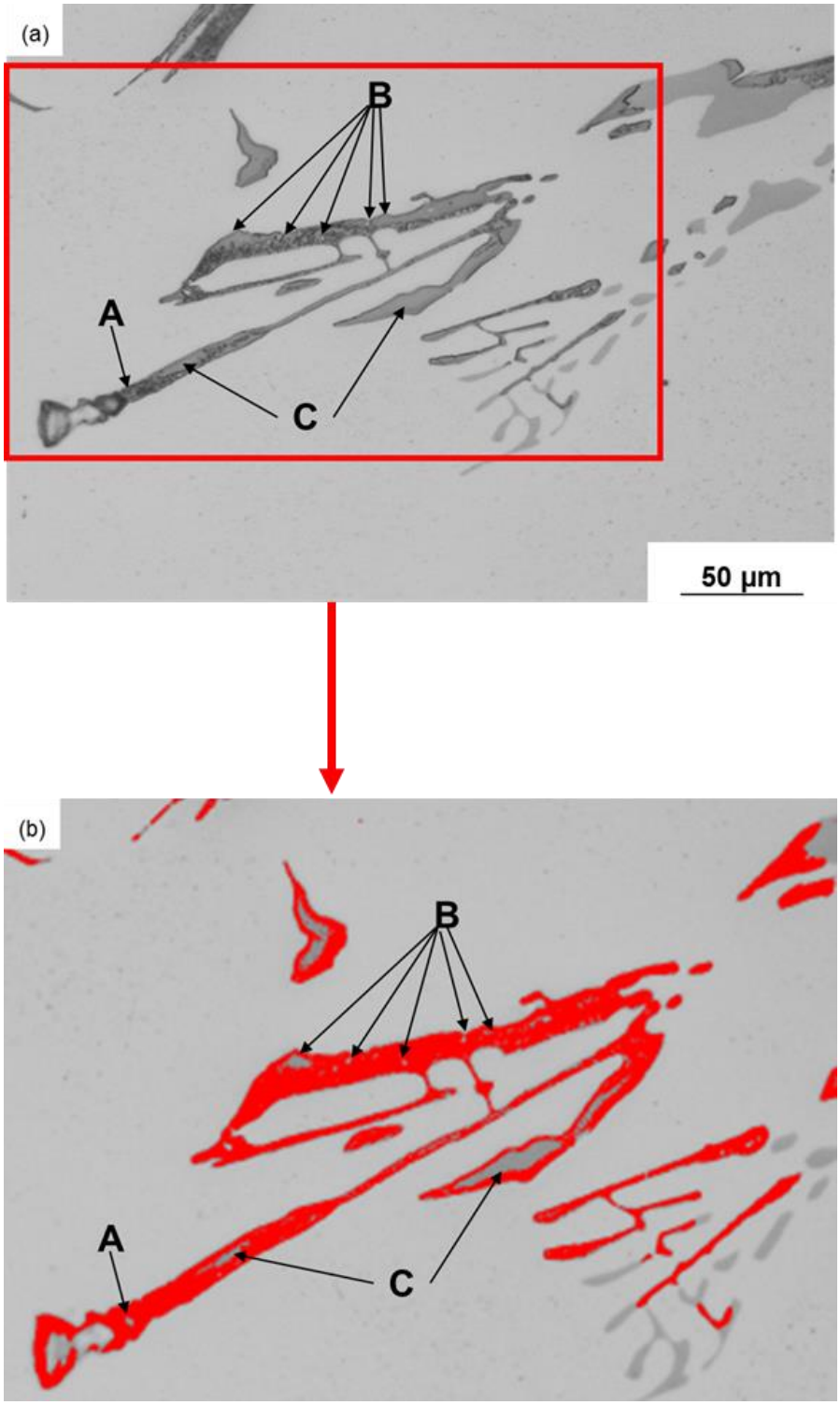

Figure 6.4: (a) Shows a light micrograph image indicating Al-spots (A and B arrows) within the intermetallic particles and (b) contains a light micrograph image where thresholding included Al-spots (A and B arrows) within the α-phase particles, as well as over-thresholding of particles in arrow C.

6.1.3 Creation of statistically meaningful data

A statistical approach was conducted to determine the number of fields of view necessary for meaningful intermetallic particle VF estimation. The graphs below show the average intermetallic particle volume fraction plotted against the number of fields of view per specimen. It is seen that specimens near the edge are more precise, as seen in Figure 6.5, Figure 6.7 and Figure 6.9, whereas specimens at the centre contain more errors, as seen in Figure 6.6, Figure 6.8 and Figure 6.10. This could be due to the higher thresholding errors that emerge within images at the centre. These images contain a higher occurrence of the dispersoids thus varying the analysis values, as seen in Figure 6.1 (b).

These graphs show that after at least 70 to 80 fields of view (on average) have been analysed the overall intermetallic particle volume fraction plateaus, hence there is no need to analyse a greater number of images.

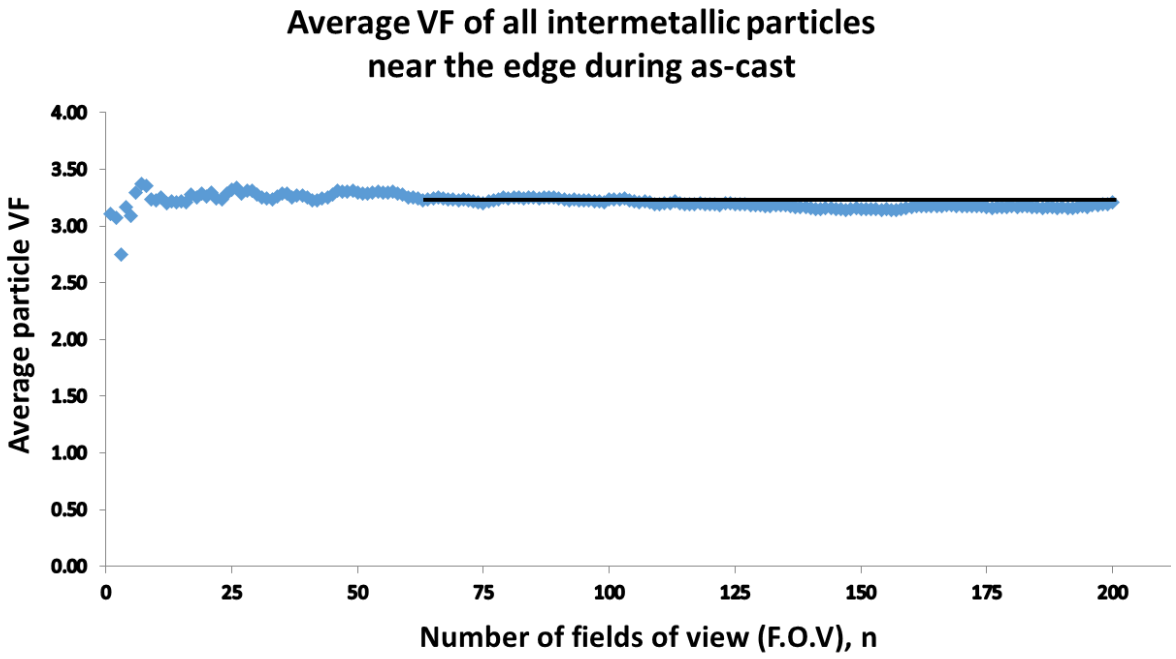

Figure 6.5: Graph showing the number of fields of view (n) necessary to obtain a meaningful volume fraction near the ingot edge in the as-cast condition.

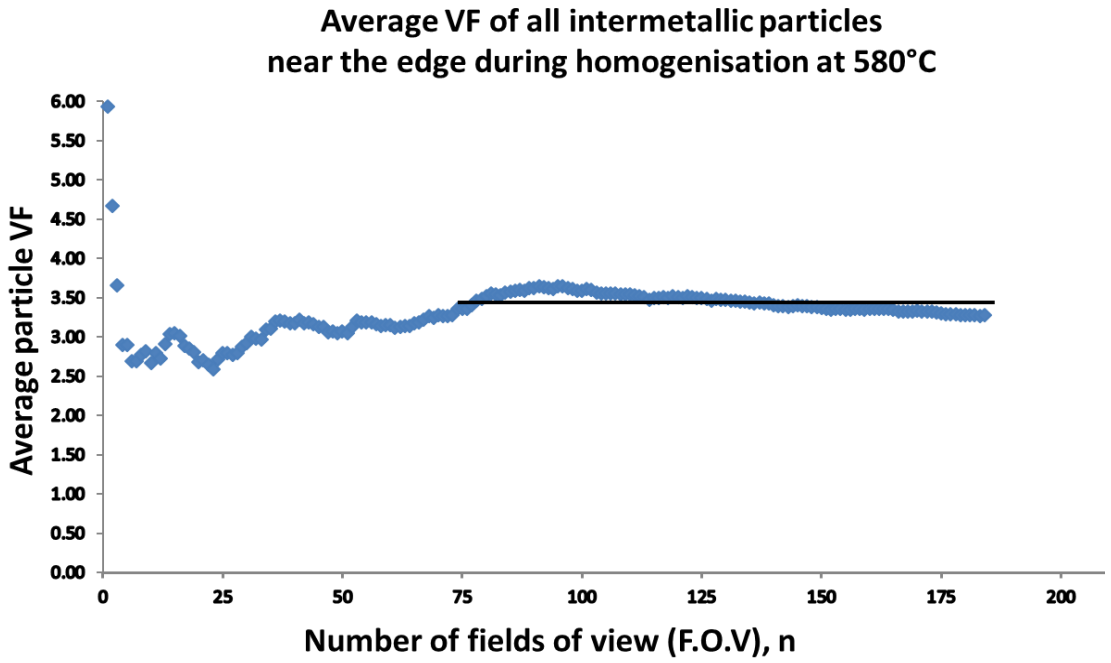

Figure 6.6: Graph showing the number of fields of view necessary to obtain a meaningful volume fraction at the ingot centre in the as-cast condition.

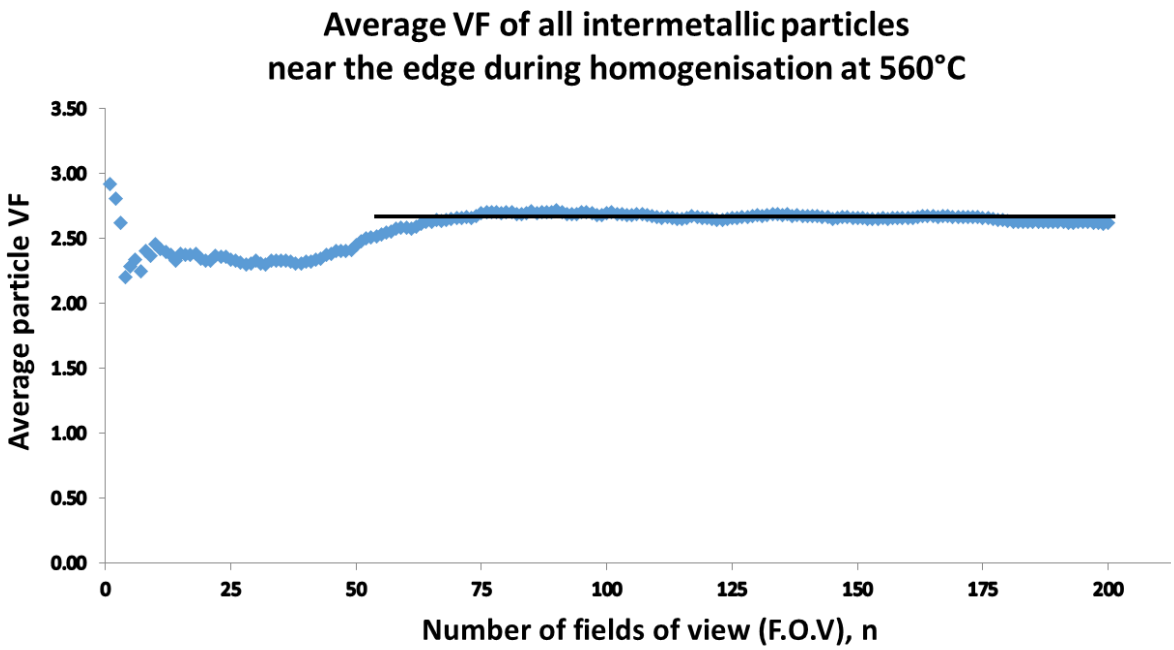

Figure 6.7: Graph showing the number of fields of view necessary to obtain a meaningful volume fraction near the ingot edge after homogenisation at 560°C/520°C.

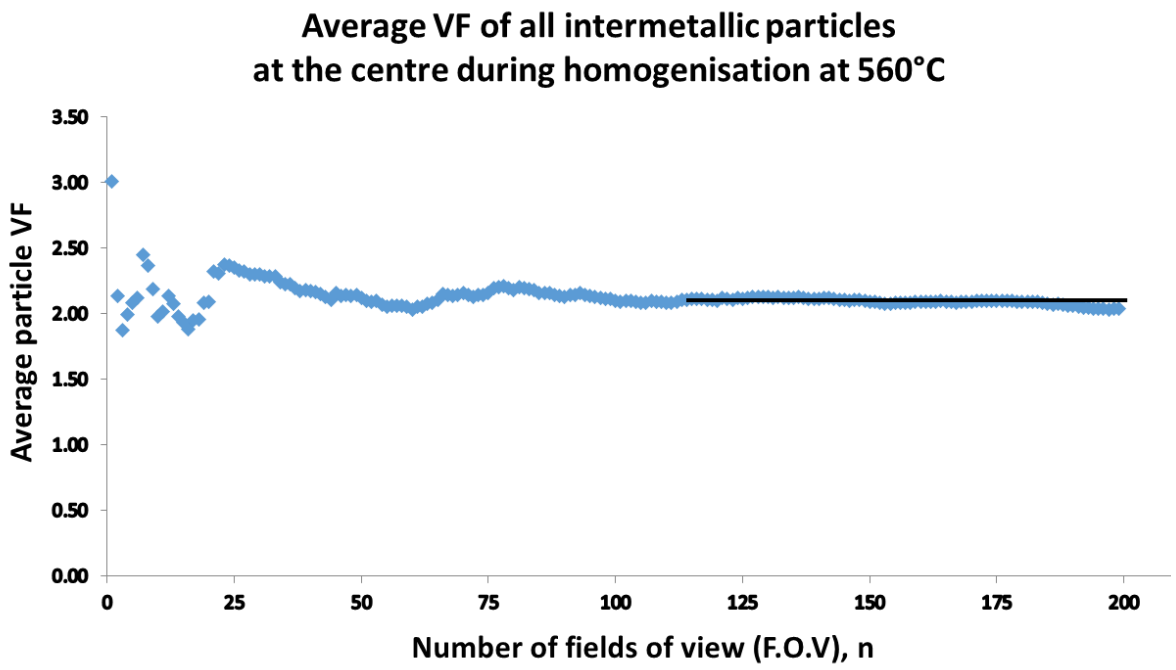

Figure 6.8: Graph showing the number of fields of view necessary to obtain a meaningful volume fraction at the ingot centre after homogenisation at 560°C/520°C.

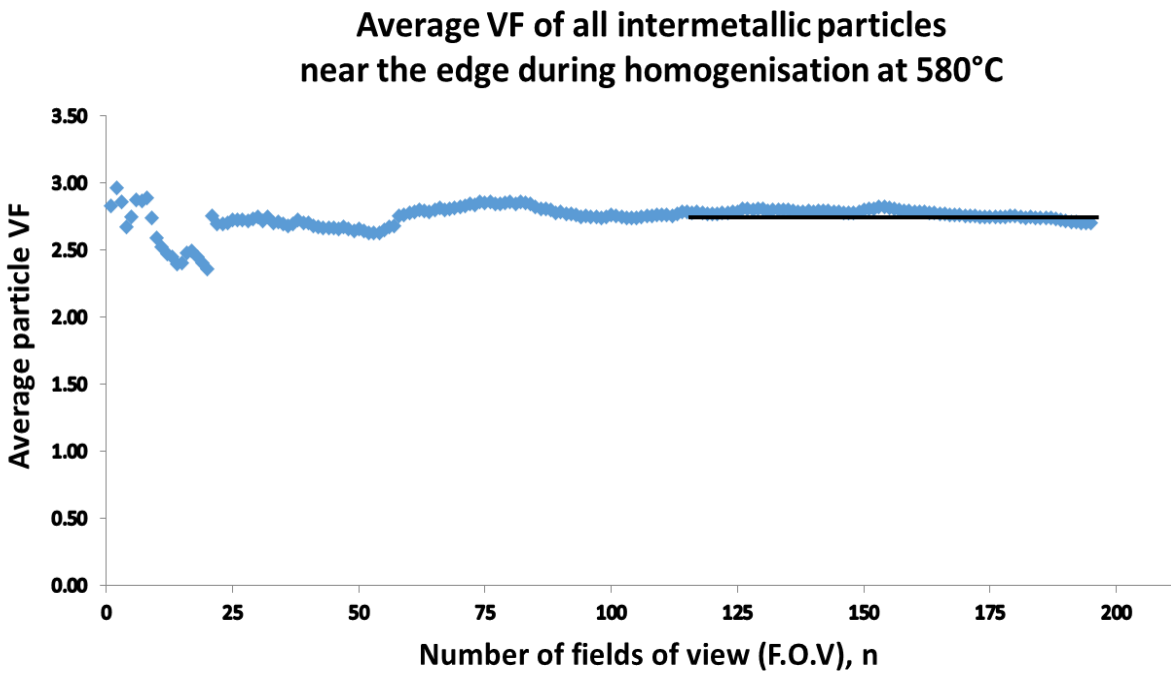

Figure 6.9: Graph showing the number of fields of view necessary to obtain a meaningful volume fraction near the ingot edge after homogenisation at 580°C/520°C.

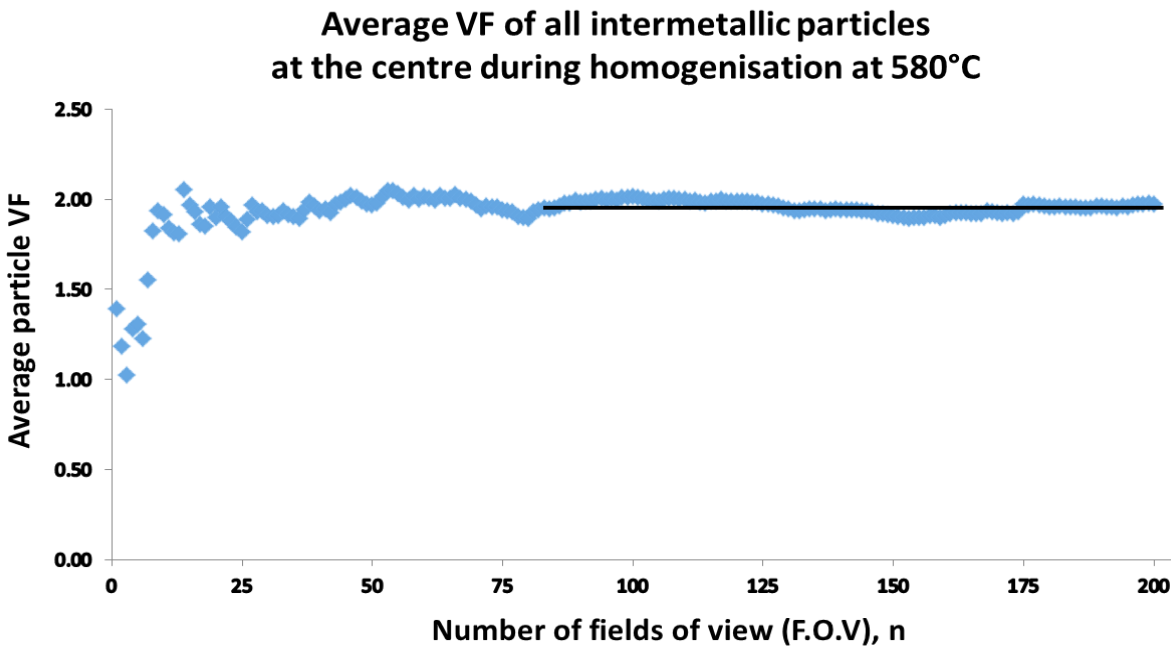

Figure 6.10: Graph showing the number of fields of view necessary to obtain a meaningful volume fraction at the ingot centre after homogenisation at 580°C/520°C.

6.1.4 Statistical and relative accuracy analysis of the data used for image analysis

Image analysis data was then further statistically analysed in order to determine whether the data was normally distributed or not. This was done in order to further analyse the number of fields of view, n, that was statistically necessary to obtain a meaningful intermetallic particle VF value using confidence intervals (CI) and relative accuracy, as suggested/developed by Van der Voort [54]. The graphs in Figure 6.11 (a) and (b) show that the MATLAB data used to produce average intermetallic particle VF is normally distributed. Therefore, confidence intervals (CI) and relative accuracy analyses can then be used to estimate the number of fields of view necessary to obtain a meaningful intermetallic particle VF.

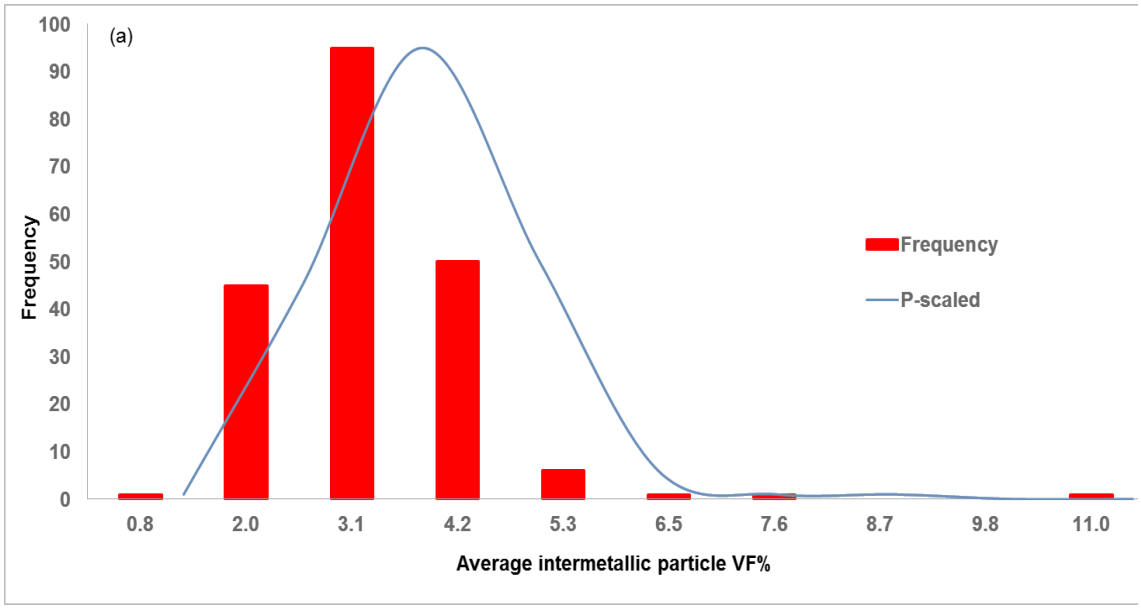

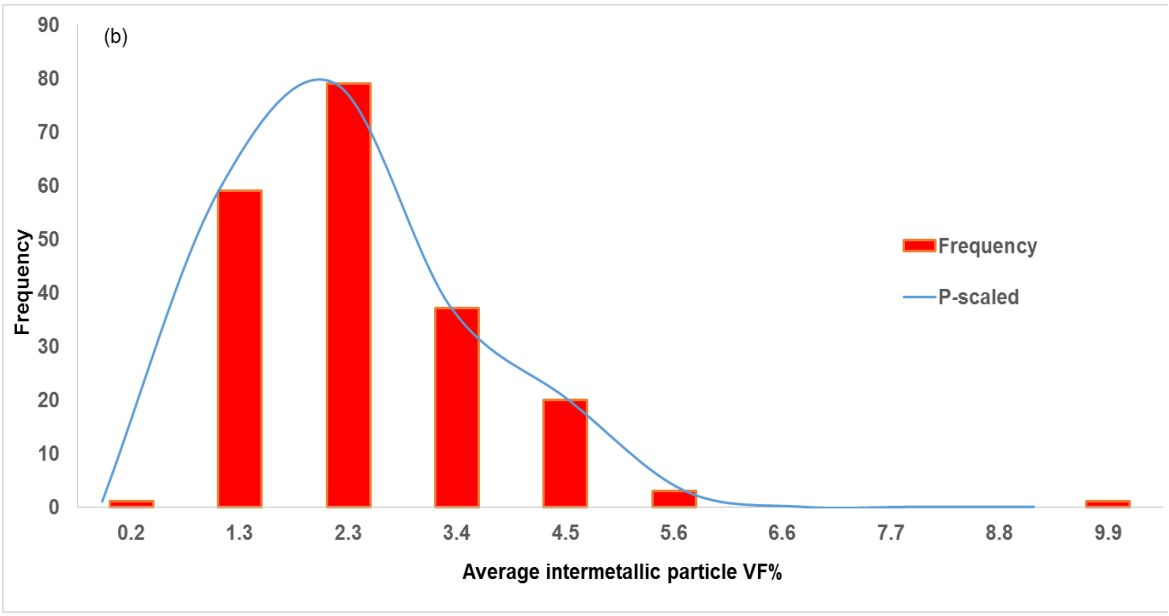

Figure 6.11: Graphs showing that the data analysed is normally distributed (a) near the edge and (b) at the centre both after homogenisation at 580°C/520°C.

Relative accuracy calculations were conducted successfully and the following results were obtained. Table 6.1 shows that the relative accuracy value decreases/becomes more acceptable/becomes more confident as the number of fields of view increases. Since analysing 200 fields of view, with RA of less than 40% takes time. Fewer fields of view were considered based on Figure 6.5 to Figure 6.10 above. Statistical analysis that shows that the average intermetallic particle VF estimation becomes constant after analysing at least 70 fields of view. Thus, it can be concluded that the estimated particle VF values are meaningful. It is then seen that fields of view between 70 and 100 gives a relative accuracy between 40% and 65% at 95% confidence interval for meaningful VF estimation. Van der Voort suggests that a higher relative accuracy (>60%) value is acceptable on materials with inclusions, therefore the values seen on Table 6.1 can be used [41].

The table shows that specimens near the edge yield a lower %RA compared to specimens at the centre, thus making the data more acceptable. Furthermore, as-cast specimens at the centre of the ingot contains a higher %RA .50 of which could be due to uneven particle size and distribution. This corresponds with the results obtained when using graphs of average particle VF to estimate fields of view necessary to obtain meaningful VF. The observation is due to the errors that arise during particle and phase quantification using image analysis as mentioned above.

Table 6.1: Showing average relative accuracy values (%) of specimens near the edge (E) and at the centre (C) of AA3104 ingot during as-cast and homogenisation obtained using image analysis and statistical analysis at 95% confidence interval.

Number of fields of view (n)	**70**	**77**	**100**	**150**	**200**
As-cast, E	37	35	31	25	22
As-cast, C	65	62	55	45	39
Homogenisation at 560°C/520°C, E	38	37	32	26	23
Homogenisation at 560°C/520°C, C	58	55	48	40	34
Homogenisation at 580°C/520°C, E	43	41	36	29	25
Homogenisation at 580°C/520°C, C	52	49	43	35	30

6.1.5 Intermetallic particle VF estimation results (using MATLAB)

Overall intermetallic particle VF varies as conditions change from as-cast to homogenised at different temperatures, as seen in Table 6.2 and Figure 6.12. The illustration in Figure 6.12 shows that specimens in the as-cast condition contain more intermetallic particles than specimens after homogenisation. However, homogenisation at 580°C/520°C near the edge contains the largest overall VF of intermetallic particles. It is also seen that specimens near the edge (E) contain more intermetallic particles compared to specimens at the centre (C). This is due to the increase in solidification rate at the centre of the ingot. Furthermore, it is seen that specimens homogenised at 560°C/520°C yields similar amount of overall intermetallic, whereas specimens homogenised at 580°C/520°C tend to differ between near the edge and at the centre of the ingot. The observations made up to this stage in terms of quantifying the intermetallic particles just give an idea of the number of particles that are present within AA3104.

Table 6.2 and Figure 6.12 also shows that as-cast specimen contain β (88%E and 86%C) as the predominant phase and traces of α-phase (12%E and 14%C). It is also seen that specimen near the edge yield α-phase particles (47% from homogenisation at 560°C/520°C and 52% from homogenisation at 580°C/520°C) that are closer to the desired 50%, compared to the centre. Additionally, specimen homogenised at 580°C/520°C show a higher amount of α-phase particles (52%E and 39%C). Phase particle quantification has a higher standard deviation at the centre compared to the phase particle quantification near the edge of the ingot. This is explained by some of the errors that arise during phase particle thresholding. This also shows that overall intermetallic particle analysis is more precise compared to particle phase analysis within the specimen microstructure using 2-D microstructural analysis. Further analysis would be necessary for a confident conclusion.

The values on Table 6.2 are averaged from the results shown in Appendix 5. This table shows that the standard deviation of overall intermetallic particles is below 1, whereas that of phase intermetallic particles is above 1. This highlights that there is less error when quantifying overall particles than the phases within the particles. Although a standard deviation of below 1 would increase the confidence on the results obtained.

.

Table 6.2: Showing average of all intermetallic particles VF, as well as particle phase fraction estimation with standard deviation by using ImageJ and MATLAB.

Phase	**Specimen/Condition**	**Estimated phase fractions (%)**					**Average** (%)	**Standard deviation**
Overall intermetallic particle VF	**As-cast, E**	3	2	3	2	3	3	0.140
	As-cast, C	3	3	2	2	2	2	0.140
	Homogenisation at 560°C, E	2	2	3	2	2	2	0.090
	Homogenisation at 560°C, C	2	2	2	2	3	2	0.170
	Homogenisation at 580°C, E	3	3	3	2	3	3	0.130
	Homogenisation at 580°C, C	2	2	2	2	2	2	0.080
β-Al6(Fe,Mn) phase	**As-cast, E**	86	86	87	91	89	88	1.790
	As-cast, C	81	83	87	84	93	86	3.870
	Homogenisation at 560°C, E	50	52	52	53	56	52	1.840
	Homogenisation at 560°C, C	60	65	72	71	76	69	4.990
	Homogenisation at 580°C, E	45	44	49	51	49	48	2.370
	Homogenisation at 580°C, C	55	56	64	62	69	61	4.810
α-Alx(Fe,Mn)$_{3Si2}$ phase	**As-cast, E**	13	14	13	9	11	12	1.620
	As-cast, C	18	17	13	16	7	14	3.630
	Homogenisation at 560°C, E	50	48	48	47	44	47	1.760
	Homogenisation at 560°C, C	39	35	28	29	24	31	4.750
	Homogenisation at 580°C, E	54	55	51	49	51	52	2.200
	Homogenisation at 580°C, C	45	43	36	38	31	39	4.590

Image analysis results in Table 6.2 show that the as-cast condition specimens contain more β-phase particles compared to the homogenised specimens. Homogenised specimens show a decrease in β-phase particles and an increase in α-phase particles due to phase transformation. The particle phase variation can be seen in Figure 6.12 where the β-phase is predominant in the as-cast condition and the α-phase increases during homogenisation. It is also seen that although the VF of the α-phase particles increase after homogenisation, specimens from near the edge contain a greater VF compared to the specimens at the centre. This can be explained by the fact that dispersoids are exposed within the microstructures of images that are used for image analysis. These dispersoids are of similar grey contrast to the α-phase particles, thus resulting in higher α-phase% estimation as seen in Figure 6.1.

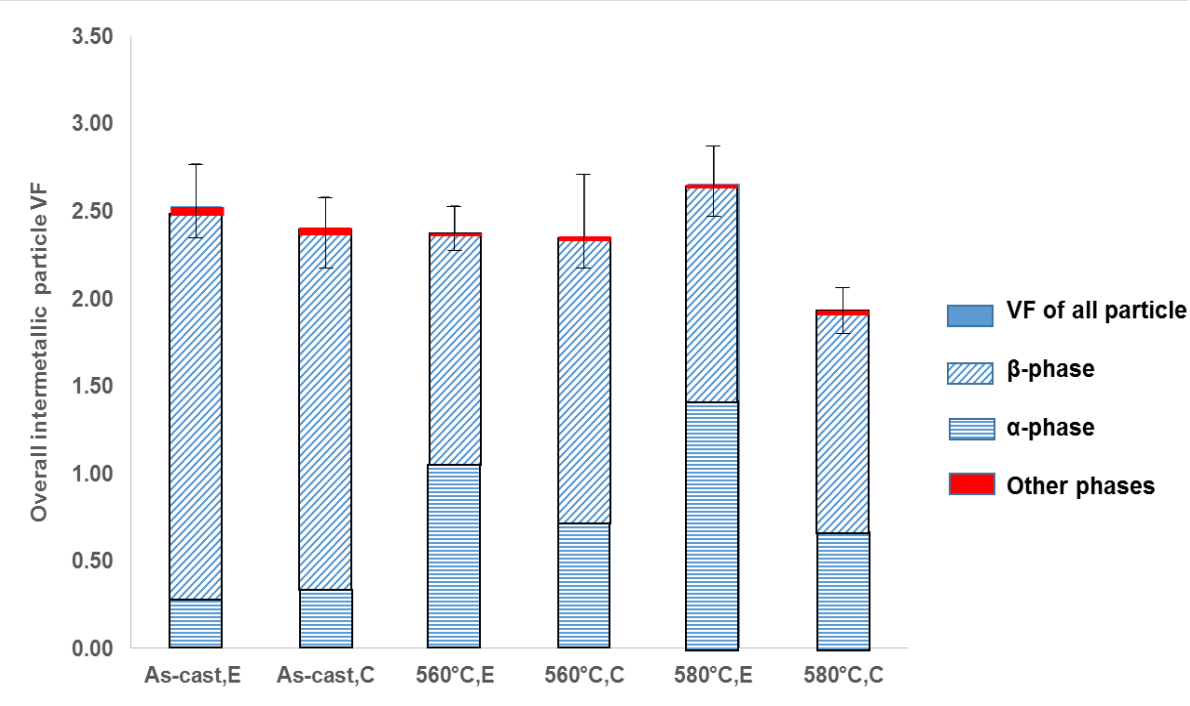

Figure 6.12: Graph showing overall intermetallic particle VF, as well as particle phase evolution during as-cast and after different homogenisation temperatures both near the edge and at the centre of the ingot, estimated using image analysis.

6.2 Particle extraction yield

After Al-matrix dissolution the solution is drained from the autoclave whilst the particles are collected by the filter inside the autoclave. It is seen that the colourless dry butanol that was in the autoclave before dissolution changes colour, indicating that a reaction has occurred. Figure 6.13 shows the colour of the solution drained after dissolution. As-cast samples produced a clear brown solution and homogenised samples produced aqueous grey solution, as seen in Figure 6.13 (a) and (b) respectively. The fact that the butanol solution drained from the homogenised samples looks aqueous could be explained by the fact that the samples are homogenised or some of the particles and dispersoids are too small that they pass through the fitted 0.1µm Teflon filter. If the drained butanol solution is colourless it means that dissolution did not occur.

Furthermore, if the solution is too dark, it means that the filter burned and some extracted particles were drained with the solution. Additionally, it is seen that the solution from samples homogenised at 560°C/520°C seems darker than that of the samples homogenised at 580°C/520°C. This, could indicate that after homogenisation at 560°C/520°C, the material contains smaller particles and dispersoids compared to after homogenisation at 580°C/520°C.

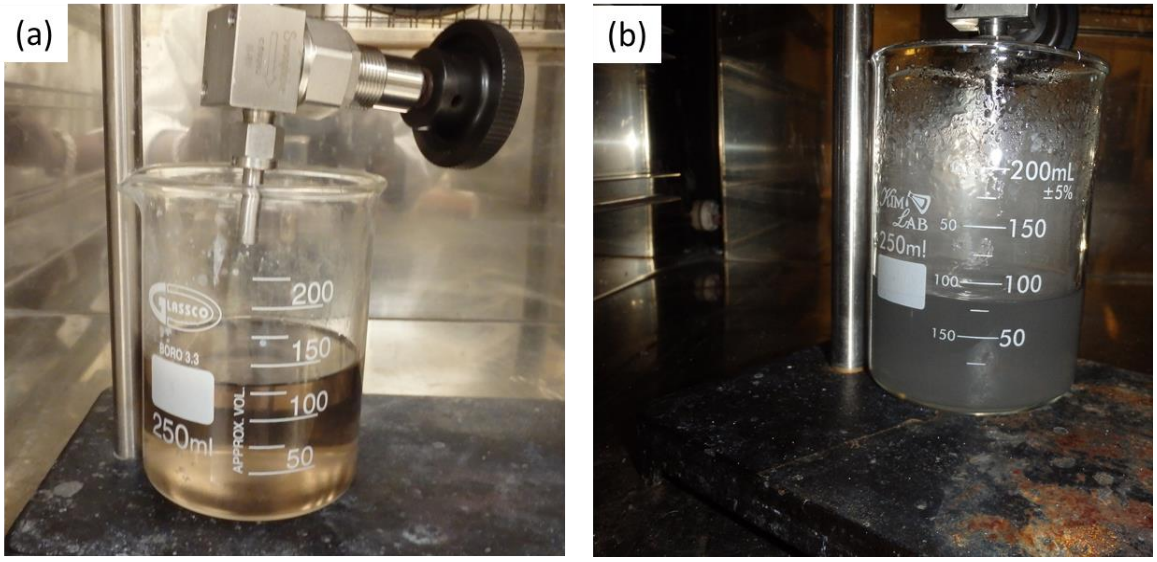

Figure 6.13: Images showing butanol solution drained after dissolution for (a) as-cast samples and (b) homogenised samples.

Table 6.3 is a summary of the table in Appendix 6 that shows the approximate time it took for dissolution to occur, as well as the amount of intermetallic particles yielded. For XRD to be conducted mass powder production was necessary, however the table highlights average results. Dissolution time varied at times due to the weather's temperature and humidity, as well as butanol drying time and Ar quality. It is also seen that extracted particle % indicates higher particle yield in samples at the edge than samples at the centre, but it is the inverse for samples homogenised at 580°C/520°C.However, this just gives an indication of what to expect and not the quantity of the intermetallic particle VF.

Table 6.3: Showing approximate dissolution time and the amount of intermetallic particles yielded.

Sample	Approximate dissolution time	Amount in (solid sample) (g)	Amount out (Extracted particles) (g)	%
As-cast, E	9-17 hrs	1.22	0.04	3.28
As-cast, C	9-21 hrs	1.15	0.03	2.81
Homogenised at 560°C/520°C, E	10-16 hrs	1.07	0.04	3.32
Homogenised at 560°C/520°C, C	6-15 hrs	1.22	0.04	3.01
Homogenised at 580°C/520°C, E	6-22 hrs	1.21	0.03	2.57
Homogenised at 580°C/520°C, C	6-21 hrs	1.23	0.04	3.03

6.3 Intermetallic phase quantification using XRD

Powder x-ray diffraction from the catalysis group at the UCT Department of Chemical Engineering and the Department of Chemistry was used for phase identification and quantification. Powder particles were quantified successfully using X-ray Diffraction (XRD) patterns, MDI Jade 5.0 software to identify the phases and Topas software to quantify the phases via the Rietveld Method. Statistical analysis for estimating the fraction of intermetallic particle phase averages was conducted using the obtained results. These detailed results can be found in Appendix 7.

Five XRD analyses were conducted per powder sample, however, only three sets of XRD analyses were used for discussion and to draw conclusions. This is because the last two analyses yielded results that were inconsistent from the original results. This is explained by the fact that the last two set of analyses were run four months after the particle extraction due to equipment unavailability. Whereas, the first three sets took two months for particle extraction and XRD analysis. The extracted particles might have been exposed to the atmosphere for too long, thus oxidising.

The results from this analysis show a typical phase fraction trend with lower errors indicated by standard deviation of up to 3. However, Table 6.4 shows a higher standard deviation of 11 on samples at the centre homogenised at 560°C/520°C and 13 on samples near the edge homogenised at 580°C/520°C (XRD analysis with Rietveld method). Whereas, Table 6.2 a lower standard deviation of 5 on specimens at the centre homogenised at 560°C/520°C and 3 on specimens near the edge homogenised at 580°C/520°C (Image Analysis). This is attributed to the errors reported from both techniques.

Table 6.4 shows that the as-cast samples contain more β-phase particles, whereas homogenised samples contain more α-phase particles. This is true for both near the edge that has 78% β and 22% α, and the centre that has 64% β and 36% α. Homogenised specimens show a decrease in β-phase particles and an increase in α-phase particles. It is also seen that samples near the edge contain more α-phase particles, while samples at the centre contain more β-phase particles. Figure 6.14 shows a column graph highlighting the change in particle VF for the different homogenisation temperatures. Error bars are also indicated in order to show the variability of the data and to indicate the uncertainty of these results. Furthermore, samples homogenised at 580°C/520°C show a further increase in α-phase particles and a further decrease in β-phase particles compared to samples homogenised at 560°C/520°C. This is expected due to the increase in temperatures which allows for high Si diffusivity thus allowing phase transformation, as explained in section 2.6.5 and section 2.7.3 [15 and 37].

Table 6.4: Showing intermetallic particle phase estimation with average and standard deviation by using the Rietveld method.

Phase		Estimated phase quantity (%)			Average (%)	Standard deviation
β-Al_6(Fe,Mn)	**As-cast, E**	82	82	70	78	5
	As-cast, C	57	67	68	64	5
	Homogenised at 560°C/520°C, E	38	40	45	41	3
	Homogenised at 560°C/520°C, C	29	41	57	43	11
	Homogenised at 580°C/520°C, E	51	44	20	38	13
	Homogenised at 580°C/520°C, C	41	46	29	39	7
α-Al_x(Fe,Mn)$_3Si_2$	**As-cast, E**	18	18	30	22	5
	As-cast, C	43	33	32	36	5
	Homogenised at 560°C/520°C, E	62	60	55	59	3
	Homogenised at 560°C/520°C, C	71	59	43	57	11
	Homogenised at 580°C/520°C, E	49	56	80	62	13
	Homogenised at 580°C/520°C, C	59	54	71	61	7

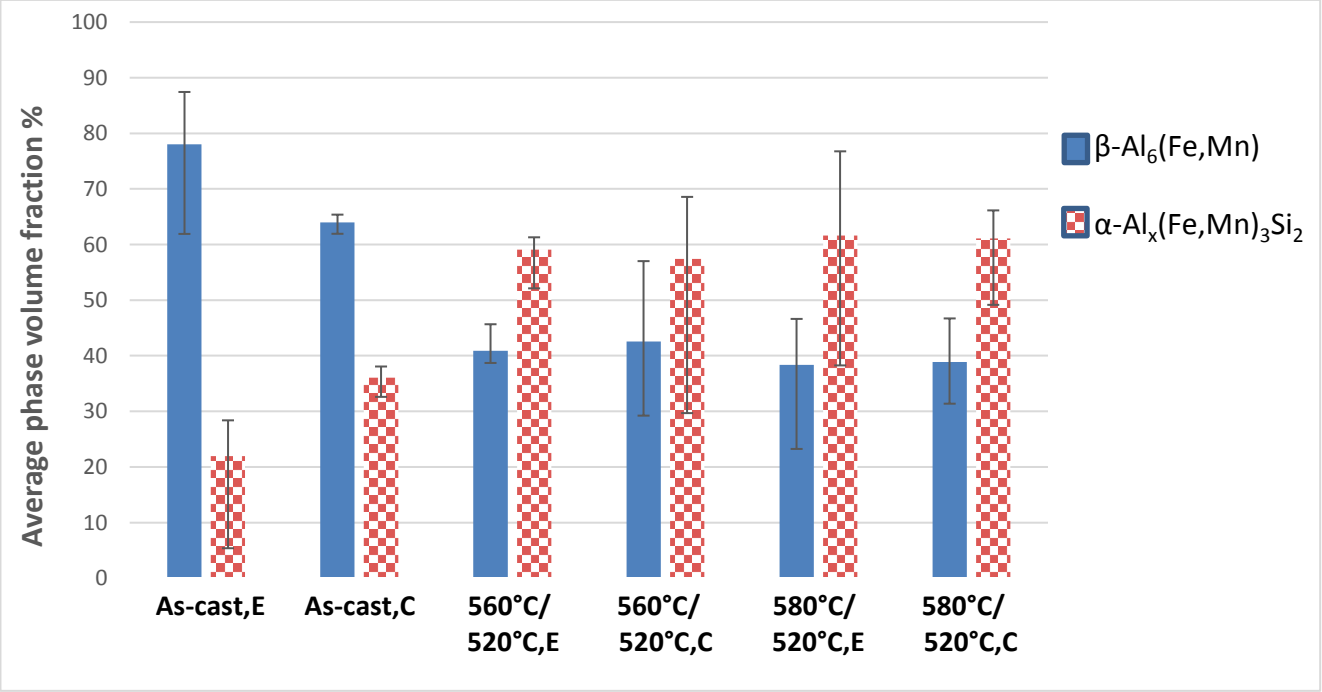

Figure 6.14: Column graph showing average intermetallic phase VF with error bars.

6.4 Summary

6.4.1 Image analysis

ImageJ and MATLAB software were used to estimate intermetallic particle VF using 2-D microstructural images. Image analysis shows that as-cast specimens contain β as the predominant phase. Whereas, homogenised specimens show a decrease in β-phase particles and an increase in α-phase particles due to phase transformation. It is also seen that specimens near the edge contain more intermetallic particles compared to specimens at the centre. This is due to the increase in solidification rate at the centre of the ingot.

Furthermore, specimens homogenised at 560°C/520°C yields similar amount of overall intermetallic at the edge and centre, whereas specimens homogenised at 580°C/520°C tend to differ between near the edge and at the centre of the ingot. Consequently, there are certain errors associated with this technique that gives inconclusive results. This can be explained by the variation in particle morphology, variation in particle distribution and the fact that dispersoids are exposed within the microstructures of the images used for image analysis. However, further analysis would be necessary for a confident conclusion.

6.4.2 Particle extraction: 3-D particle quantification

The particle extraction technique based on the SiBut method was successfully used for particle extraction. XRD was then used where Al_3Mg_2, T_AlCuMgZn, S_Al_2CuMg, Mg_2Si, Al_6Mn (β) and alpha-$Al_x(Fe,Mn)_3Si_2$ (α) phases were identified as intermetallic particles. The Rietveld method was used for intermetallic phase quantification, which shows that the as-cast samples contain more β-phase particles, whereas homogenised samples contain more α-phase particles. This is true for both near the edge and at the centre of the ingot. Homogenised specimens show a decrease in β-phase particles and an increase in α-phase particles due to phase transformation. It is also seen that samples near the edge contain more α-phase particles, while samples at the centre contain more β-phase particles. Furthermore, samples homogenised at 580°C/520°C show a higher amount of α-phase particles and a further decrease in β-phase compared to samples homogenised at 560°C/520°C.

7 COMPARISON OF 2-DIMENSIONAL AND 3-DIMENSIONAL INTERMETALLIC VOLUME FRACTION

Looking at microstructural analysis [two-dimensional (2-D)] and particle extraction analysis [three-dimensional (3-D)] of the intermetallic particles in Table 7.1, it is seen that the two techniques agree when it comes to microstructural qualification and tend to differ on microstructural/particle quantification. The table shows that both techniques show the presence of α and β phases, as well as reveal the morphological differences within the particles. However, XRD shows more phases present within AA3104. Furthermore, both techniques show similar trends of high VFs of β-phase in the as-cast condition and an increase in α-phase after homogenisation due to phase transformation.

Phase quantification using 2-D analysis shows more α-phase near the edge and less α-phase at the centre. While the extraction analysis shows less α-phase near the edge and more α-phase at the centre. Additionally, the 2-D microstructural analysis of specimens after homogenisation at 580°C/520°C yields a greater VF of α-phase than homogenisation at 560°C/520°C near the edge. Whereas, homogenisation at 560°C/520°C yields a greater VF of α-phase than homogenisation at 580°C/520°C at the centre. The difference in results obtained can be attributed to similar thresholding errors. Where, the presence of dispersoids, as well as the size of the particles contributed to the particle phase quantification during thresholding. Never the less, both 2-D microstructural analysis and particle extraction analyses show that an increase in α-phase particles and a decrease in β-phase particles as the homogenisation temperature increases.

Microstructural analysis (2-D) is less likely to be reliable due to the technique only quantifying the intermetallic particles based on 2-D particles on an areal section of a sample as well as the errors attributed to the topography and surface area of the particle phases. However, lower standar deviations are obtained from this technique. Whereas, Particle extraction analysis is more likely to be reliable due to the technique quantifying the intermetallic particle phases in their 3-D form. But the technique gives higher standard deviations due to the time frame between particle extraction and XRD analysis. Which means that more errors associated with the technique can be avoided by making sure that not a long time passes before XRD analysis on the extracted particles is conducted.

Table 7.1: Showing comparison between 2-D microstructural analysis and 3-D (Particle extraction) intermetallic particle VF analysis.

2-D (Image Analysis)	3-D (Particle Extraction/The SiBut Method)	Discussion/Comments
The presence of β-Al_6(Fe,Mn) and α-Al_x(Fe,Mn)$_3Si_2$ phase particles can be identified using LM and SEM with EDS.	The presence of β-Al_6(Fe,Mn), α-Al_x(Fe,Mn)$_3Si_2$ and other phases can be identified within the extracted particles using XRD.	Both techniques show the presence of α, β phases and traces of Mg_2Si. However, XRD shows other phases present within the AA3104 material.
Phases within the intermetallic particles are morphologically distinguishable. The β-phase is more needle-like and the α-phase is more non-geometric/Chinese-script-like.	Phases within the extracted intermetallic particles are morphologically distinguishable. The β-phase is more needle-like and the α-phase is more non-geometric/Chinese-script-like.	Both techniques reveal the morphological differences.
High β-phase particles of 88% near the edge and 86% at centre, in the as-cast condition.	High β-phase particles of 78% near the edge and 64% at centre, in the as-cast condition.	Both techniques show similar trends. However, the particle extraction method is less reliable.
Increase in α-phase and decrease in β-phase during homogenisation.	Increase in α-phase and decrease in β-phase during homogenisation.	Both techniques show similar trends.
More α-phase near the edge (47% after homogenisation at 560°C/520°C and 52% after homogenisation at 580°C/520°C) and less at the centre (31% after homogenisation at 560°C/520°C and 39% after homogenisation at 580°C/520°C).	More α-phase near the edge (59% after homogenisation at 560°C/520°C and 62% after homogenisation at 580°C/520°C) and less at the centre (57% after homogenisation at 560°C/520°C and 61% after homogenisation at 580°C/520°C).	Both techniques show similar trends. However, particle extraction analysis is more trustworthy than 2-D particle analysis, where the presence of dispersoids, the size of the particles as well as higher β-surface area compared to α contributed to the particle phase quantification during thresholding. Although standard deviations of the two techniques prove otherwise.

Homogenisation at 580°C/520°C yields a greater α-phase VF than homogenisation at 560°C/520°C both near the edge and at the centre of the ingot.	Homogenisation at 580°C/520°C yields a greater VF of α-phase than homogenisation at 560°C/520°C both near the edge and at the centre of the ingot.	Both techniques show similar trends.
Homogenisation at 560°C/520°C yields an α:β ratio at both the edge and the centre that is closer to the required 50:50 ratio for better galling resistance.	Homogenisation at 560°C/520°C yields an α:β ratio at both the edge and the centre that is closer to the required 50:50 ratio for better galling resistance.	Both techniques indicate the same trend in the ratios.
Main advantages: Saves time and resources. Also a general trend can be established easily. Main disadvantages: Not reliable	Main advantages: More reliable and pure residue yield when used properly. Main disadvantages: Possible contamination and a lot of time needed.	

8 CONCLUSIONS

This study focused on qualitatively and quantitatively investigating the extent to which intermetallic particles in aluminium alloy AA3104 can-body stock evolve during homogenisation. Of importance is the assessment of microstructural changes as well as volume fraction (VF) of the primary Si-rich α-phase and Si-free β-phase intermetallic particles using a conventional 2-D image analysis technique and a complex particle extraction technique based on the SiBut method for 3-D analysis. The following conclusions are made:

1. Microstructural analysis of both solid specimen and extracted particles shows that:
    - The phases are morphologically distinguishable with β-phase particles having a needle-like/flake-like shape and the α-phase particles having a non-geometric/comb-like/Chinese-script-like shape.
    - There is an increase in α-phase and decrease in β-phase particles after homogenisation, thus indicating phase transformation.
    - Near the edge there is a greater number of smaller and fragmented particles compared to particles at the centre, where there appears to be fewer particles that are more coarse and visually united/solid.

2. 2-D evaluation and 3-D evaluation are in agreement with both the qualitative and quantitative observations. Therefore, the two techniques complement each other, however, the 3-D evaluation revealed quantitative values that were deemed more reliable with fewer errors;
    - 2-D evaluation revealed that the as-cast condition has the β-phase as the predominant phase both near the edge (88%) and at the centre of the ingot (86%). It also revealed that there is an increase in the α-phase due to β→α phase transformation during homogenisation. Furthermore, 2-D results show that samples near the edge contain a higher number of α-phase particles when homogenised at 560°C/520°C, giving a volume fraction of 47%, compared to the volume fraction of 52% when homogenised at 580°C/520°C.
    - 3-D evaluation revealed that the as-cast condition has the β-phase as the predominant phase both near the edge (78%) and at the centre of the ingot (64%). It also revealed that there is an increase in the α-phase due to β→α phase transformation during homogenisation. Furthermore, 3-D results show that samples near the edge contain a higher number of α-phase particles when

homogenised at 560°C/520°C, giving a volume fraction of 59%, compared to the volume fraction of 62% when homogenised at 580°C/520°C.

3. Homogenisation at 580°C/520°C yield a higher VF of α-phase intermetallic particles compared to homogenisation at 560°C/520°C both near the edge and at the centre of the ingot. Additionally, samples near the edge contain more α-phase particles compared to samples at the centre.
   - Homogenisation at 560°C/520°C yields 59% of the α-phase near the edge and 57% of the α-phase at the centre.
   - Homogenisation at 580°C/520°C yields 62% of the α-phase near the edge and 61% of the α-phase at the centre.

4. For galling resistance to be improved, the AA3104 sheet materials needs to have a desired total intermetallic particle VF of 1-3% , where approximately 50% of of the particles is the harder α-$Al_x(Fe,Mn)_3Si_2$ phase. This research obtained a total intermetallic particle VF of 1.9 – 2.7% which is very close to the desired value. Homogenisation at 560°C/520°C is the better homogenisation treatment because it yields 59% of the α-phase near the edge and 57% of the α-phase at the centre which is closer to the desired β→α ratio.
   - Homogenisation at 560°C/520°C yields 58% of the α-phase on average, while Homogenisation at 580°C/520°C yields 62% of the α-phase on average. Perhaps Homogenisation at 550°C/520°C will then be closer to 50%.

9 RECOMMENDATIONS

A number of recommendations for the future investigations are made owing to the limited scope of this study, and based on findings reported in this dissertation. These are:

- Image analysis software/freeware used had some errors attributed to them. This can be explained by the variation in particle morphology, variation in particle distribution and the fact that dispersoids are exposed within the microstructures of the images used for this analysis. Thus, it is important to invest in a more advanced image analysis software that will eliminate some of these errors. The advanced software should be able to differentiate the particles in geometric morphology as well as differentiate between the major particles and dispersoids. Additionally, further research on other potential etchants that best expose and differentiate the intermetallic particles and particle phases within the matrix is necessary.
- The particle extraction experiment is very sensitive to the atmosphere and heat. Drying butanol requires an inert gas to speed up the reaction and to prevent the dry butanol collected from getting wet again. Furthermore, the whole experiment should preserve heat, preventing the dry butanol and filled autoclave from getting cold, thus allowing the dissolution to occur. A particle extraction plant containing the drying process apparatus connected to the dissolution apparatus is suggested to be set up in the fumehood, this will make sure that the whole experiment remains in an inert atmosphere and allows for the preservation of heat. This will avoid the wetting butanol and sample oxidation. Thus, eliminating contamination and accelerating the reaction process.
- The liquid drained after dissolution of homogenised samples is aqueous instead of clear. This is argued to be due to the dispersoids and/or particles that are smaller than 0.1µm thus passing through the PTFE filter used. Thus, a second filter with pores smaller than 0.1µm should be fitted in the autoclave to separately catch the dispersoids.
- Phase identification using XRD patterns took longer due to the absence a database containing phases found in this material. Thus, an advanced software containing database with these phases should be made available thus saving time and increasing the chances of matching the peaks with the correct phase.
- Actual can-body stock must be processed to industrially confirm whether homogenisation at 560°C/520°C really is better than homogenisation at 580°C/520°C.

10 REFERENCES

[1] “Think green steel cans-tin cans,” [Online]. Available: http://www.thinkgreen.com/pdf/steel-cans-tin-cans.pdf. [Accessed 09 October 2012].

[2] “Think green aluminium cans,” [Online]. Available: http://www.thinkgreen.com/pdf/aluminum-cans.pdf. [Accessed 09 October 2012].

[3] M. Winter, “Aluminium»the essentials [WebElements Periodic Table],” 1993-2015. [Online]. Available: http://www.webelements.com/aluminium/. [Accessed 05 May 2015].

[4] M. C. o. A. a. A. G. S. Aluminium, “Australian mines atlas,” 1999. [Online]. Available: http://www.australianminesatlas.gov.au/build/pdf/education/aluminium.pdf. [Accessed 31 May 2015].

[5] AZoM.com, “Aluminium Specifications,” 2000-2015. [Online]. Available: http://www.azom.com/article.aspx?articleID=2863. [Accessed 31 May 2015].

[6] Aalco Metals Ltd, “Aalco,” 04 October 2016. [Online]. Available: www.aalco.co.uk/.../Aalco-Metals-Ltd_Aluminium-Alloy-Specifications_42.pdf.ashx. [Accessed 06 June 2017].

[7] P. W. Jeffrey and J. C. Blade, “Aluminium alloy can stock and method of making same”. United States Patent 4318755, 9 March 1982.

[8] L. T. Magidi, “The evolution of intermetallic particle composition during homogenisation of AA3104 can-body stock,” University of Cape Town, Cape Town, 2012.

[9] R. B. Cayless, “Alloy and temper designation systems for Aluminum and Aluminum alloys,” *ASM Handbook,* vol. 2, pp. 15-28, 1990.

[10] aluMATTER, “aluMATTER | Aluminium | Wrought Aluminium Alloys | 3xxx Series Alloys,” The University of Liverpool, 2001-2010. [Online]. Available: http://aluminium.matter.org.uk/content/html/eng/default.asp?catid=214&pageid=2144417082. [Accessed 2015 May 31].

[11] aluMATTER, “aluMATTER | Aluminium | Beverage Cans | Beverage Cans,” The university of Liverpool, 2001-2010. [Online]. Available: http://aluminium.matter.org.uk/content/html/eng/default.asp?catid=84&pageid=1941055071. [Accessed 31 May 2015].

[12] I. Jin and J. Fitzsimon, “Cast aluminium alloy for can stock and process for producing the alloy”. Montreal, Canada Patent 6120621, September 2000.

[13] P. Wycliffe, E. Luce, D. J. Lloyd, J. Fitzsimon and G. Burger, “Process for producing aluminium can body stock”. Montreal, Canada Patent 5913989, 22 June 1999.

[14] R. G. Kamat, “Alloy and method for making continuously cast aluminium alloy can stock”. Richmond, Va Patent 5634991, 3 June 1997.

[15] R. Rick and P. Evans, “Intermetallic Phase Transformation: galling performance,” Pietermaritzburg, Durban, 2014.

[16] G. F. Wyatt-Mair and D. G. Harrington, “Method of Manufacturing Can Body Sheet”. California Patent 5470405, 1995.

[17] M. F. Frolish, J. C. Walker, W. M. Rainforth and J. H. Beynon, “Formation and structure of a subsurface layer in hot rolled aluminium alloy AA3104 transfer bar,” *Tribology International,* vol. 38, pp. 1050-1058, 2005.

[18] C. Gandhi, “Effect of Homogenisation on The Microstructural Development in Ad.C. Cast AA3104 Aluminium Alloy Used for Canbody Stock,” Indian Institute of Technology, Kharagpur, India, 1999.

[19] R. G. Kamat, “Can-body stock ingot characterization and homogenization,” *The Journal of Minerals, Metals & Materials Society,* vol. 48, no. 6, pp. 34-38, June 1996.

[20] G. J. Marshall, “Microstructural control during processing of aluminium canning alloys,” *Materials Science Forum,* Vols. 217-222, pp. 19-30, 1996.

[21] D. L. Alexander and A. L. Greer, “Solid-state intermetallic phase transformations in 3XXX aluminium alloys,” *Acta Materialia,* vol. 50, pp. 2571-2583, 2002.

[22] R. G. Hamerton, H. Cama and M. W. Meredith, “Development of the coarse intermetallic particle population in wrought aluminium alloys during ingot casting and thermo-mechanical processing,” *Materials Science Forum,* Vols. 331-337, pp. 143-154, 2000.

[23] AluMATTER, “aluMATTER,” 2001-2010. [Online]. Available: http://aluminium.matter.org.uk/content/html/eng/default.asp?catid=84&pageid=-1941055071. [Accessed 07 April 2015].

[24] W. B. Hutchinson, A. Oscarsson and A. Karlsson, “Control of microstructure and earing behaviour in aluminium alloy AA3004 hot bands,” *Materials science and technology,* vol. 5, November 1989.

[25] R. G. Kamat, J. Ng-Yelim and S. Saimoto, “Morphology and precipitation of α-Al(Fe,Mn)Si phase in hot rolled AA3004,” *Zeitschrift fur metallkunde,* vol. 86, 1995.

[26] A. Verma, S. Kumar, P. S. Grant and K. Q. O'Reilly, “Influence of cooling rate on the Fe intermetallic formation in an AA6063 Al alloy,” *Journal of Alloys and Compounds,* vol. 555, pp. 274-282, 2013.

[27] . T. Smith, K. O'Reilly, S. Kumar and I. Stone , “Influence of grain-refiner addition on the morphology of Fe-bearing intermetallics in a semi-solid processed Al-Mg-Si alloy,” *Metallurgical and Materials Transactions A,* vol. 44A, pp. 4866-4871, November 2013.

[28] D. T. L. Alexander and A. L. Greer, “Formation of eutectic intermetallic rosettes by entrapment of liquid droplets during cellular columnar growth,” *Acta Materialia,* vol. 52, pp. 5853-5861, 2004.

[29] C. J. Simensen, P. Fartum and A. Andersen, “Analysis of intermetallic particles in aluminium by dissolution of the sample in butanol,” *Fresenius Z Anal Chem,* vol. 319, pp. 286-292, 1984.

[30] W. Yang, S. Ji, X. Zhou, I. Stone, G. Scamans, G. E. Thompson and Z. Fan, “Heterogeneous Nucleation of alpha-Al Grain on Primary alpha-AlFeMnSi Intermetallic Investigated using 3-D SEM Ultramicrotomy and HRTEM,” *Metallurgical and Materials Transaction A,* vol. 45A, pp. 3971-3979, 2014.

[31] G. Mrowka-Nowonik, J. Sieniawski and M. Wierzbinska, “Intermetallic phase particles in 6082 aluminium alloy,” *Archives of Materials Science and Engineering,* vol. 28, no. 2, pp. 69-76, February 2007.

[32] S. Lin, C. Aliravci and M. O. Pekguleryuz, “Hot-Tear Susceptibility of Aluminum Wrought Alloys,” *Metallurgical and Materials Transactions A,* vol. 38A, pp. 1056-1068, 2007.

[33] D. L. Alexander and A. L. Greer, “Nucleation of the Al6(Fe, Mn)-to α-Al–(Fe, Mn)–Si transformation in 3XXX aluminium alloys. I. Transformation in cast aluminium alloys,” *Philosophical Magazine,* vol. 84, no. 28, pp. 3051-3070, October 2004.

[34] D. L. Alexander and A. L. Greer, “Nucleation of the Al6(Fe, Mn)-to α-Al–(Fe, Mn)–Si transformation in 3XXX aluminium alloys. II. Transformation in cast aluminium alloys,” *Philosophical Magazine,* vol. 84, no. 28, pp. 3071-3083, October 2004.

[35] Y. J. Li and L. Arnberg, “Quantitative study on the precipitation behavior of dispersoids in DC-cast AA3003 alloy during heating and homogenization,” *Acta Materialia,* vol. 51, pp. 3415-3428, 2003.

[36] A. Lise Dons, “The Alstruc homogenisation model for industrial aluminium alloys,” *Journal of Light Metals,* vol. 1, pp. 133-149, 2001.

[37] M. Dehmas , P. Weisbecker, G. Geandier, P. Archambault and E. Aeby-Gautier, “Experimental study of phase transformation in 3003 aluminium alloys during heating by in situ high energy X-ray synchrotron radiation,” *Journal of Alloys and Compounds,* vol. 400, pp. 116-124, 2005.

[38] N. Saunders, “The application of calculated phase equilibria to multi-component aluminium alloys,” *Keikinzoku Gakkai,* vol. 51, no. 3, pp. 141-150, 2001.

[39] N. Saunders, “The modelling of stable and metastable phase formation in multi-component Al-alloys,” in *Proceedings 9th International Conference on Aluminium Alloys*, Brisbane, Australia, 2004.

[40] “Mathworks,” The Mathworks, inc, 199-2017. [Online]. Available: https://www.mathworks.com/discovery/imageanalysis.. [Accessed 01 February 2017].

[41] G. F. Van der Voort, “Introduction to stereology and quantitative metallography,” Beuhler Ltd., Lake Bluff, Illinois USA.

[42] N. C. W. Kuijpers, W. H. Kool, P. T. G. Koenis, K. E. Nilsen, I. Todd and S. van der Zwaag, “Assesment of different techniques for quantification of α-Al(FeMn)Si and β-AlFeSi intermetallics in AA6xxx alloys,” *Materials Characterization,* vol. 49, pp. 409-420, 2003.

[43] N. C. W. Kuijpers, J. Tirel, D. N. Hanlon and S. van der Zwaag, “Quantification of the evolution of the 3D intermetallic structure in 6005A aluminium alloy during a homogenisation treatment,” *Materials Characterization,* vol. 48, pp. 379-392, 2002.

[44] J. Kang, D. S. Wilkinson, D. V. Malakhov, H. Halim, M. Jain, D. J. Embury and R. K. Mishra, “Effect of processing route on the spatial distributions of constituent particles and their role in fracture process in AA5754 alloy sheet materials,” *Materials Science & Engineering A,* vol. 456, pp. 85-92, 2007.

[45] N. C. W. Kuijpers, “Kinetics of the β-AlFeSi to α-Al(FeMn)Si transformation in Al-Mg-Si alloys,” The Netherlands Institute for Metals Research (NMR), Netherlands, 2004.

[46] S. Kumar, P. S. Grant and K. Q. O'Reilly, “Fe bearing intermetallic phase formation in a wrought Al-Mg-Si alloy,” *Transactions of the Indian Institute of Metals,* vol. 65, no. 6, pp. 553-557, December 2012.

[47] S. Kumar, N. Hari Babu, G. M. Scamans, Z. Fan and K. Q. O'Reilly, “Twin roll casting of Al-Mg alloy with high added impurity content,” *Metallurgical and Materials Transactions A,* vol. 45A, February 2014.

[48] C. J. Simensen and A. I. Spjelkavik, “Analysis of oxides, carbides and iron-rich particles in magnesium,” *Fresenius' Zeitschrift für analytische Chemie,* vol. 300, pp. 177-182, 1980.

[49] M. Hosseinifar , “Physical meatllurgy and thermodynamics of aluminum alloys containing cerium and lanthanum,” Sharif University of Technology, Tehran, Iran, 2001.

[50] E. Marie, J. C. Grenier, D. Daniel, A. Baldacci, H. Klocker and A. Bigot, “Quantitative 3D characterization of intermetallic phases in an Al-Mg industrial alloy by X-ray microtomography,” *Scripta Materalia,* vol. 55, pp. 123-126, 2006.

[51] X.-y. Lu, E.-j. Guo, P. Rometsch and L.-j. Wang, “Effect of one-step and two-step homogenization treatments on distribution of Al3Z dispersoids in commercial AA7150 aluminium alloy,” *Trans. Nonferrous Met. Soc. China,* vol. 22, pp. 2645-2651, 2012.

[52] D. T. L. Alexander, R. G. Hamerton, H. Cama and A. L. Greer, “Investigating the alpha transformation - A solid-state phase change of dispersed intermetallic particles from an Al6(Fe,Mn) phase to an α-Al-(Fe,Mn)-Si phase,” in *Light Metals*, Springer International Publishing, 2016, pp. 1015-1020.

[53] E. E. Underwood, “Quantitative Stereology for Microstructural Analysis,” in *Microstructural Analysis*, New York, Springer US, 1973, pp. 35-66.

[54] G. F. Vander Voort, “George Vander Voort,” 1988. [Online]. Available: http://www.georgevandervoort.com/metallography/quantitative/20001339-measurement-of-extremely-low-inclusion-contents-by-image-analysis.html. [Accessed 03 August 2015].

[55] Y. Zhang, Z. Zhang and R. E. Sanders, “Study of the Phase Transformation from (Fe,Mn)Al6 to α-Al(Fe,Mn)3Si in AA3104 Aluminium Alloy During Homogenization,” *Acta Metallurgica Sinica,* vol. 48, no. 3, pp. 351-356, 2012.

[56] A. M. F. Muggerud, Y. Li and R. Holmestad, “Composition and orientation relationships of constituent particles in 3xxx aluminium alloys,” *Philosophical Magazine,* vol. 94, no. 6, pp. 556-568, 2014.

[57] J. P. Martins, A. M. Carvalho and A. F. Padilha, “Microstructure and texture assessment of Al-Mn-Fe-Si (3003) aluminium alloy produced by continuous and semicontinuous casting processes,” *Journal of Material Science,* vol. 44, pp. 2966-2976, 2009.

[58] G. Mrowka-Nowotnik, J. Sieniawski and A. Nowotnik, “The chemical phenol extraction of intermetallic particles from casting AlSiCu1Mg alloy,” *Journal of Microscopy,* vol. 237, no. 3, pp. 407-410, 2010.

[59] G. Mrowka-Nowotnik, J. Sieniawski and M. Wierzbinska, “Analysis of intermetallic particles in AlSi1MgMn aluminium alloy,” *Journal of Achievements in Materials and Manufacturing Engineering,* vol. 20, no. 1-2, January-February 2007.

[60] P. R. Goulart, V. B. Lazarine, C. V. Leal, J. E. Spinelli, N. Cheung and A. Garcia, “Investigation of intermetallics in hypoeutectic Al-Fe alloys by dissolution of the Al matrix,” *Intermetallics,* vol. 17, pp. 753-761, 2009.

[61] Y. Birol, “Homogenisation of a twin-roll cast thin Al-Mn strip,” *Journal of Alloys and Compounds,* vol. 471, pp. 122-127, 2009.

[62] C. Gras, M. Meredith and J. D. Hunt, “Microdefects formation during the twin-roll casting of Al-Mg-Mn aluminium alloys,” *Journal of Materials Processing Technology,* vol. 167, pp. 62-72, 2005.

[63] Y. Birol, “Homogenization of direct chill cast AlSi1MgMn billets,” *International Journal of Materials Research,* vol. 105, pp. 75-81, 2014.

[64] G. Sha, K. O'Reilly, B. Cantor, J. Worth and R. Hamerton, “Growth related metastable phase selection in a 6xxx series wrought Al alloy,” *Materials Science and Engineering,* Vols. A304-306, pp. 612-616, 2001.

[65] V. L. Niranjani, K. C. Hari Kumar and V. Subramanya Sarma, “Development of high strength Al-Mg-Si AA6061 alloy through cold rolling and ageing,” *Materials Science and Engineering,* vol. A515, pp. 169-174, 2009.

[66] M. Zawrah and L. Shaw, “Microstructure and hardness of nanostrustured Al-Fe-Cr-Ti alloys through mechanical alloying,” *Materials Science and Engineering,* vol. A355, pp. 37-49, 2003.

[67] [Online]. Available: http://www.sphweb.bumc.bu.edu/otlt/MPH-Modules/BS/SAS/SAS-OneSampleTtest/SAS4-OneSampleTtest_print.html. [Accessed 05 April 2016].

[68] D. Crystal, “Brooks/Cole,” Thompson Learning, 2005. [Online]. Available: http://www.slideshare.net/rwmiller/chapter09. [Accessed 05 April 2016].

11 APPENDICES

11.1 Appendix 1: ImageJ

The following steps demonstrate how ImageJ program was used to estimate the image threshold value for each specimen.

1. Open ImageJ program then open image

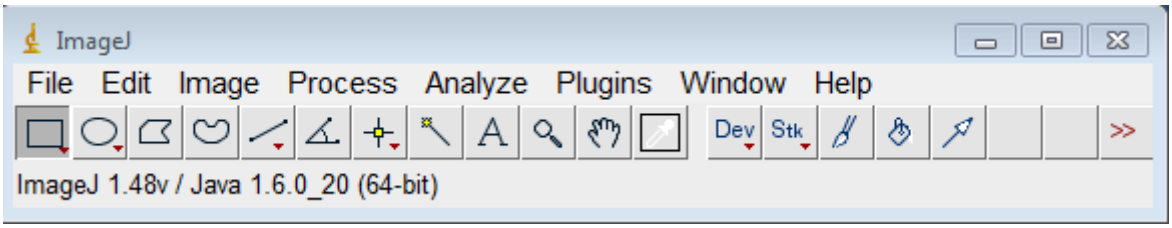

Figure 11.1: Showing ImageJ work window.

Select File>Open>select the image to be analysed (image B1_14, B143 50X magnification)

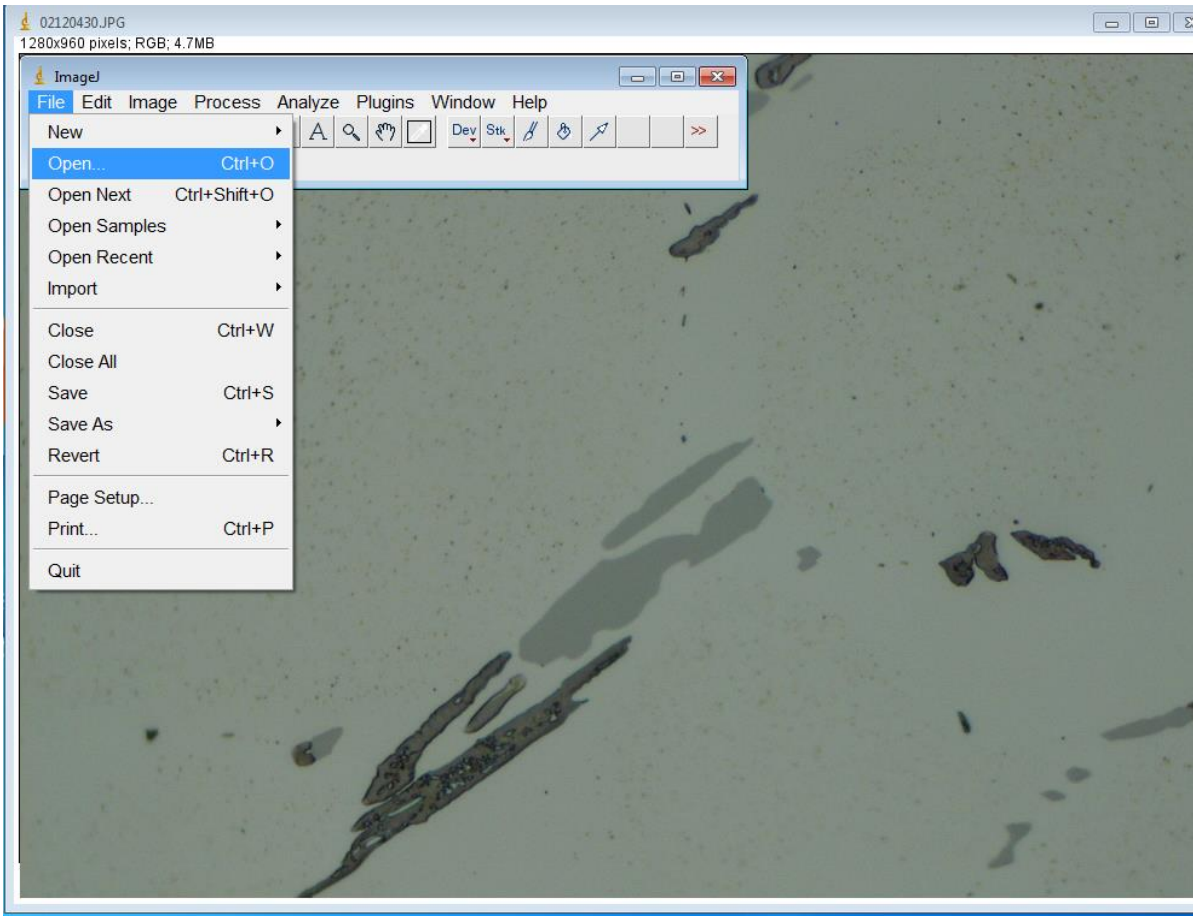

Figure 11.2: showing image selection.

2. Calibrate by setting the scale

Draw a line on image>measure the line with a ruler>select analyse>measure length

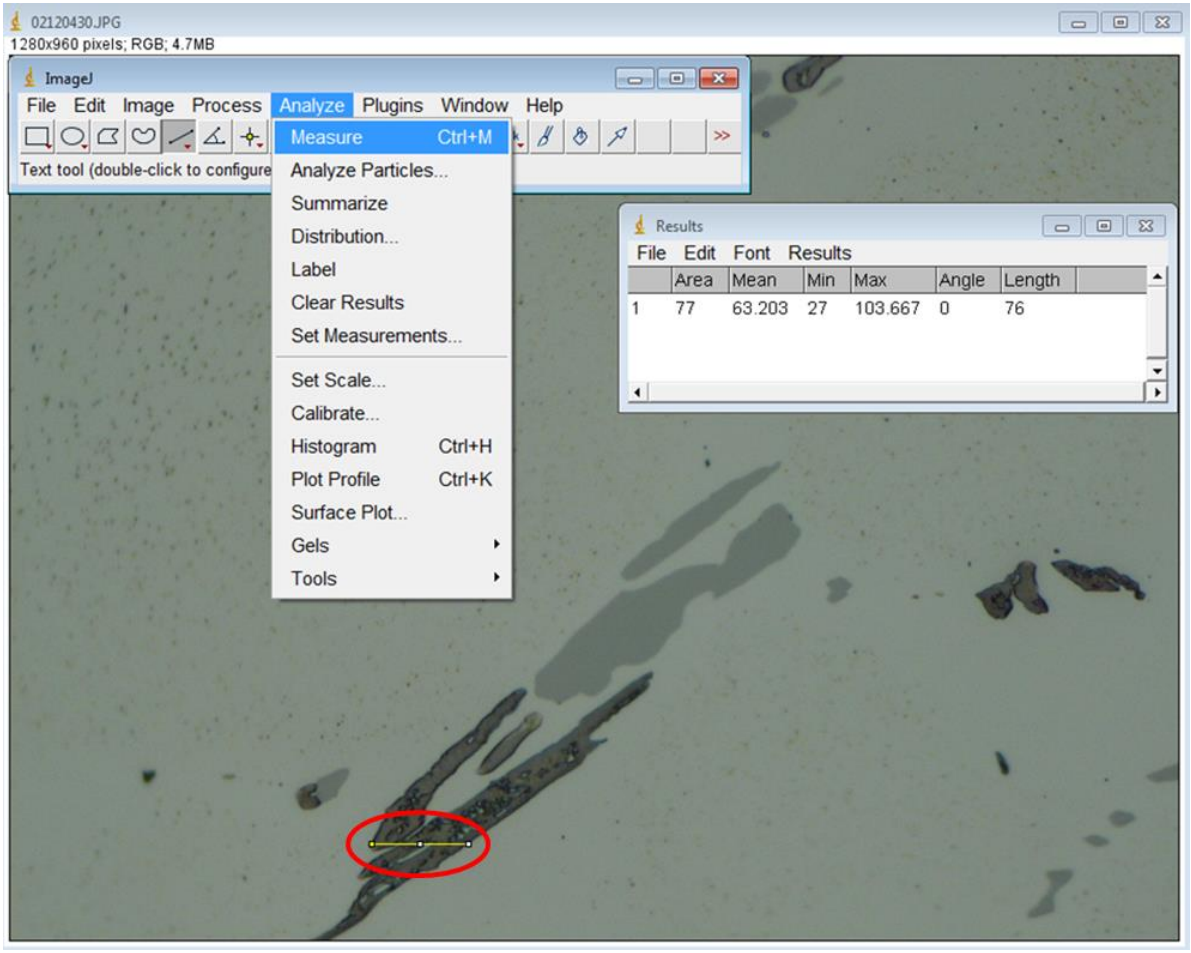

Figure 11.3: Showing calibration.

Then select analyse> set scale and a small window will pop-up>input values. Check global if the same scale applies to the next series of images.

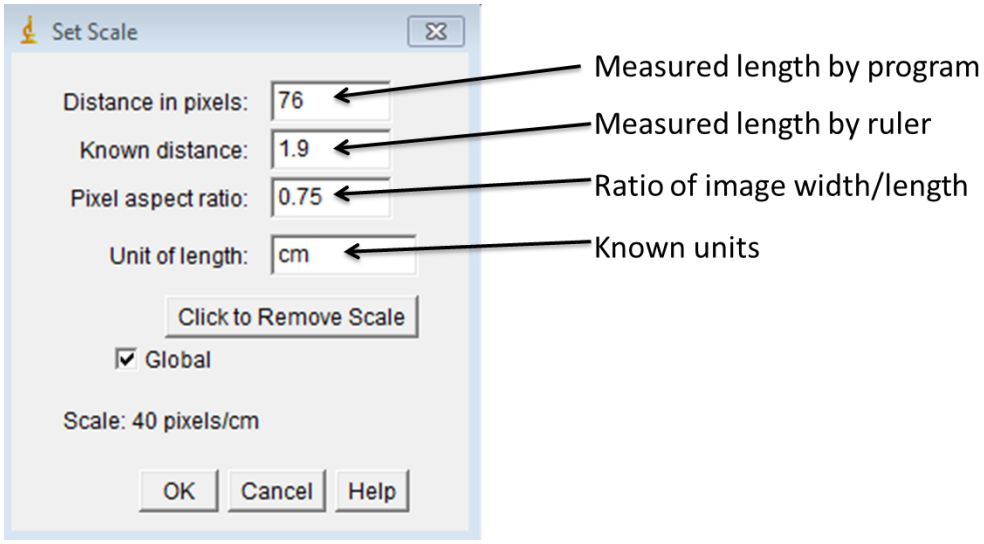

Figure 11.4: Showing an example of values used when calibrating software.

3. Change image to greyscale

Select image>type>8-bit

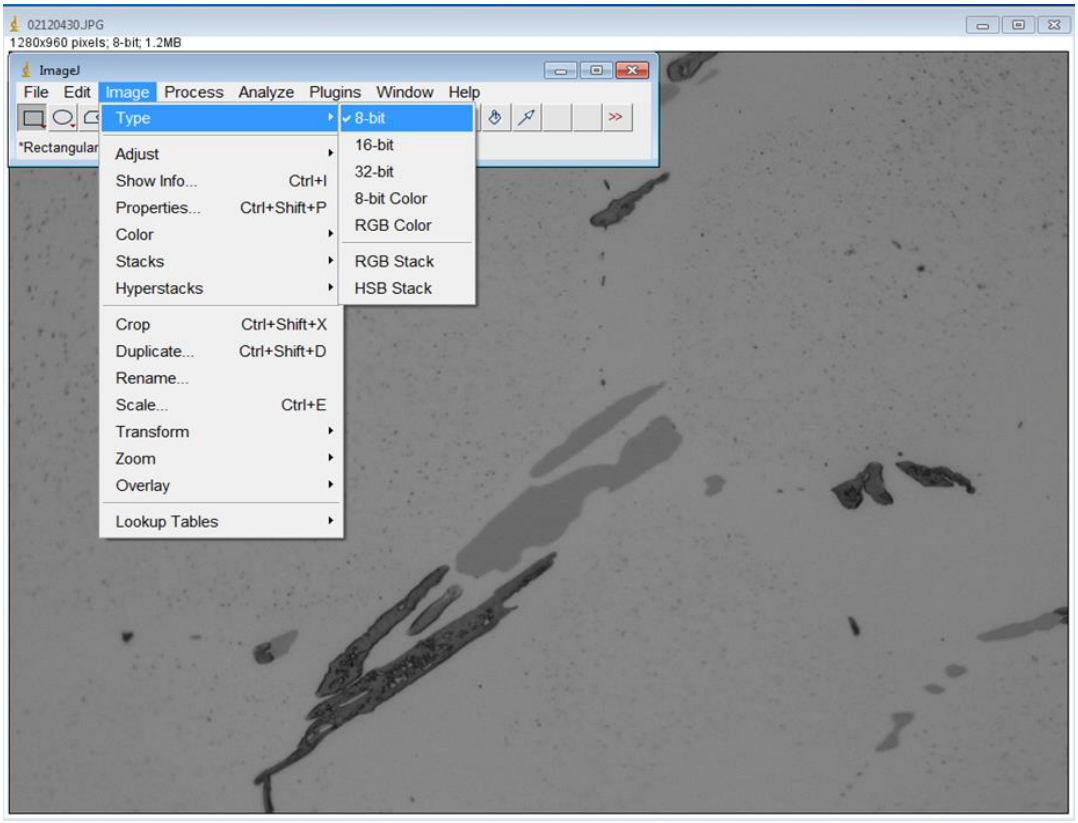

Figure 11.5: Showing image changed to greyscale.

4. Threshold image

Select image>adjust>threshold

The threshold window pops-up showing a peak illustrating the greyscale with the most pixel count.

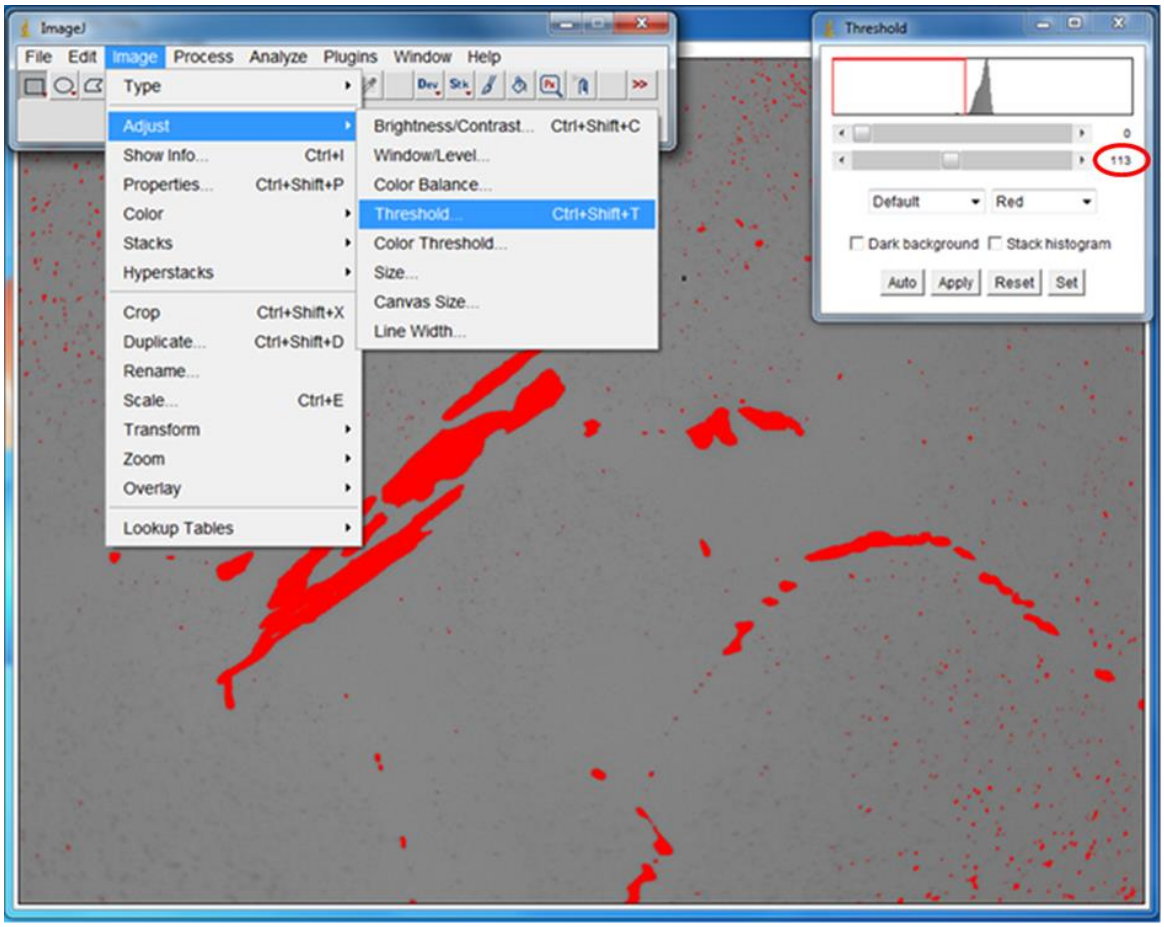

Figure 11.6: Showing how images were thresholded.

5. Analyse particles

Select analyse>analyse particles and a small window will pop-up. Check each box according to preferences. Then click ok.

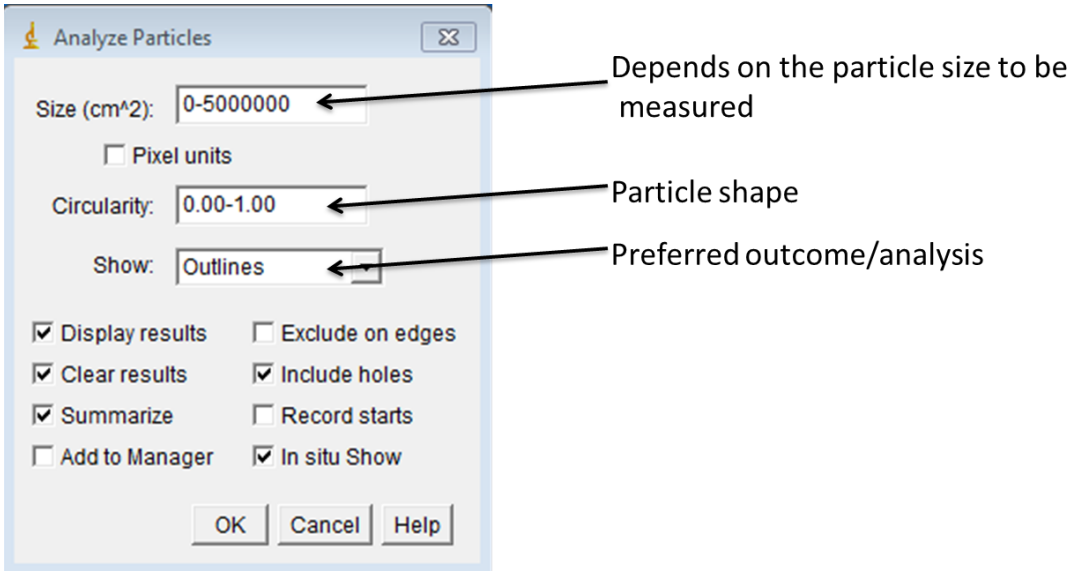

Figure 11.7: Showing values used to analyse particles according to particle dimensions.

A summary window with results pops-up and the file is saved as a Microsoft Excel spreadsheet.

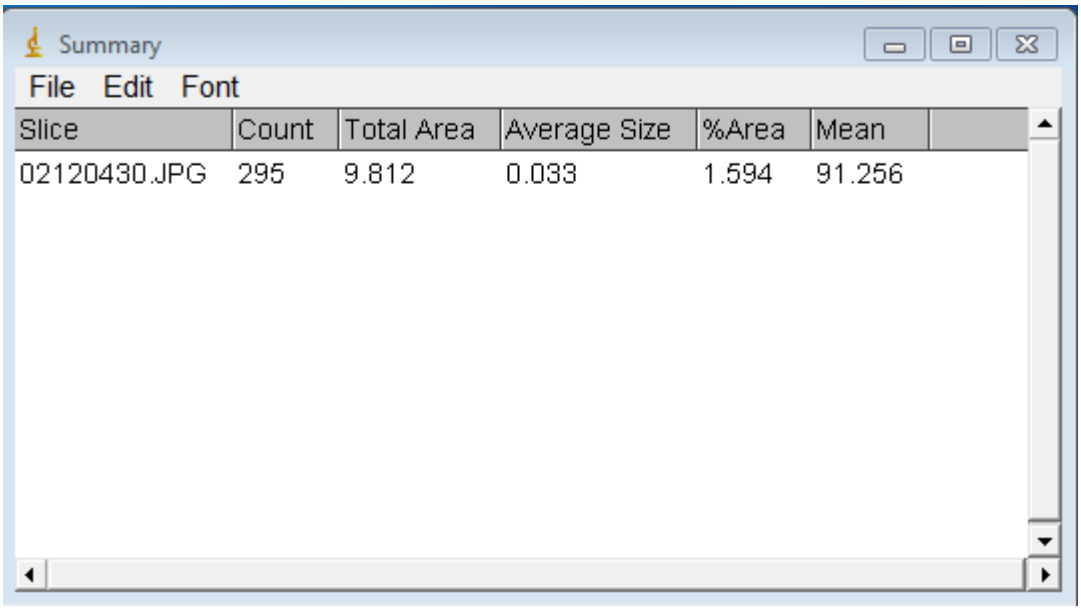

Figure 11.8: Showing results summary.

6. Record and save data

The above mentioned steps were repeated for 15-30 images and an excel spreadsheet is produced, as seen below. The mean threshold values (highlighted in blue) were then used to estimate particle VF using MATLAB. The whole procedure was repeated for all specimens. After that, steps 3 to 6 were repeated to estimate α-phase and Mg_2Si particles threshold value.

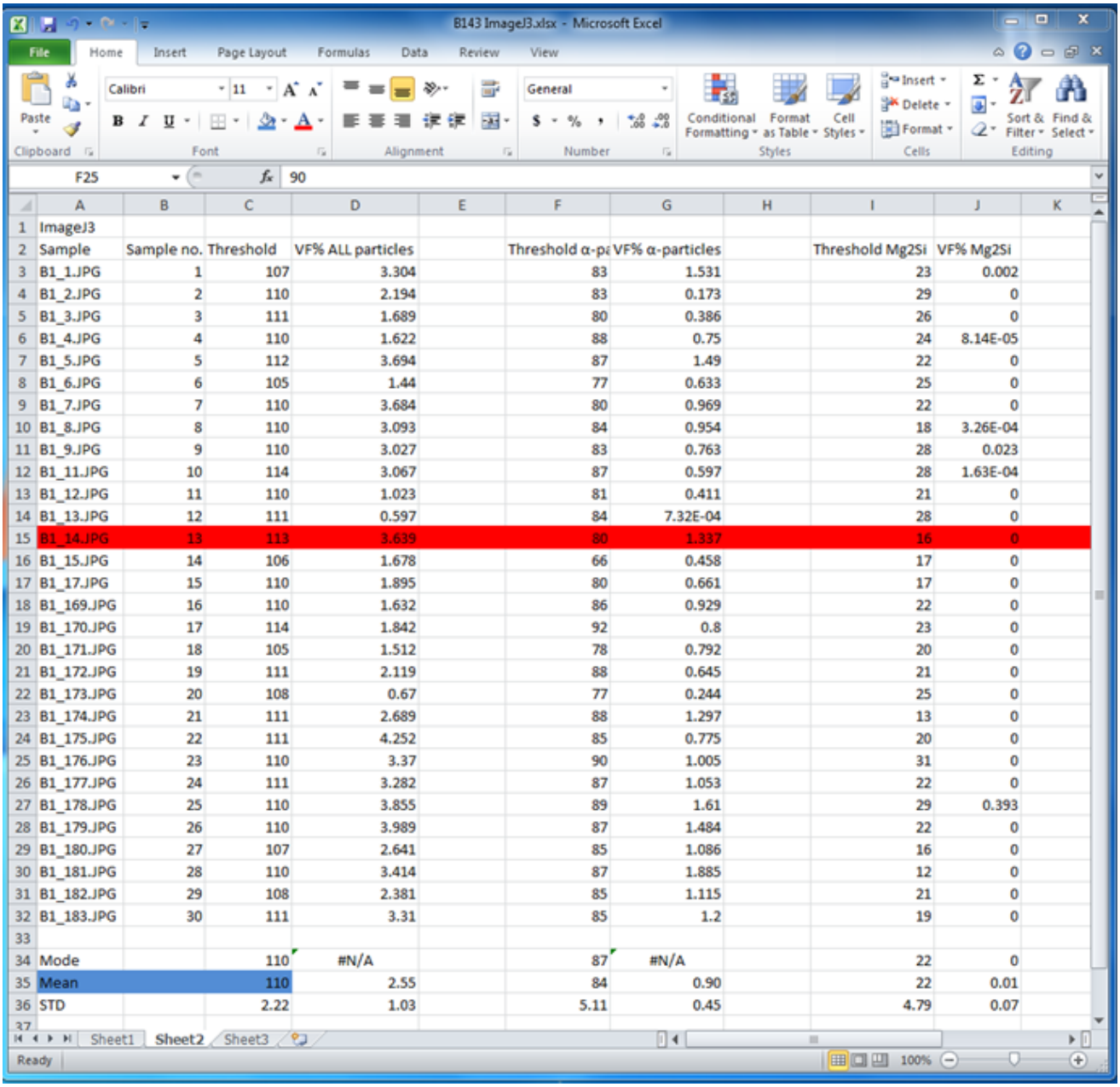

B143 ImageJ3.xlsx - Microsoft Excel

	A	B	C	D	E	F	G	H	I	J	K
1	ImageJ3										
2	Sample	Sample no.	Threshold	VF% ALL particles		Threshold α-pa	VF% α-particles		Threshold Mg2Si	VF% Mg2Si	
3	B1_1.JPG	1	107	3.304		83	1.531		23	0.002	
4	B1_2.JPG	2	110	2.194		83	0.173		29	0	
5	B1_3.JPG	3	111	1.689		80	0.386		26	0	
6	B1_4.JPG	4	110	1.622		88	0.75		24	8.14E-05	
7	B1_5.JPG	5	112	3.694		87	1.49		22	0	
8	B1_6.JPG	6	105	1.44		77	0.633		25	0	
9	B1_7.JPG	7	110	3.684		80	0.969		22	0	
10	B1_8.JPG	8	110	3.093		84	0.954		18	3.26E-04	
11	B1_9.JPG	9	110	3.027		83	0.763		28	0.023	
12	B1_11.JPG	10	114	3.067		87	0.597		28	1.63E-04	
13	B1_12.JPG	11	110	1.023		81	0.411		21	0	
14	B1_13.JPG	12	111	0.597		84	7.32E-04		28	0	
15	B1_14.JPG	13	113	3.639		80	1.337		16	0	
16	B1_15.JPG	14	106	1.678		66	0.458		17	0	
17	B1_17.JPG	15	110	1.895		80	0.661		17	0	
18	B1_169.JPG	16	110	1.632		86	0.929		22	0	
19	B1_170.JPG	17	114	1.842		92	0.8		23	0	
20	B1_171.JPG	18	105	1.512		78	0.792		20	0	
21	B1_172.JPG	19	111	2.119		88	0.645		21	0	
22	B1_173.JPG	20	108	0.67		77	0.244		25	0	
23	B1_174.JPG	21	111	2.689		88	1.297		13	0	
24	B1_175.JPG	22	111	4.252		85	0.775		20	0	
25	B1_176.JPG	23	110	3.37		90	1.005		31	0	
26	B1_177.JPG	24	111	3.282		87	1.053		22	0	
27	B1_178.JPG	25	110	3.855		89	1.61		29	0.393	
28	B1_179.JPG	26	110	3.989		87	1.484		22	0	
29	B1_180.JPG	27	107	2.641		85	1.086		16	0	
30	B1_181.JPG	28	110	3.414		87	1.885		12	0	
31	B1_182.JPG	29	108	2.381		85	1.115		21	0	
32	B1_183.JPG	30	111	3.31		85	1.2		19	0	
33											
34	Mode		110	#N/A		87	#N/A		22	0	
35	Mean		110	2.55		84	0.90		22	0.01	
36	STD		2.22	1.03		5.11	0.45		4.79	0.07	
37											

Figure 11.9: Showing an example of a spreadsheet produced by ImageJ as an output.

11.2 Appendix 2: ImageJ thresholding results

The following table shows particle thresholding values which were averaged and used for particle VF estimation using MATLAB. Section 6.1 shows a table of averaged threshold values from Table 11.1 to Table 11.5 of each specimen which highlights the common particle greyscale contrast values.

Table 11.1: Showing part 1 of particle average thresholding greyscale values obtained after several analyses using ImageJ.

Specimen/Condition	Overall intermetallic particle	α-phase particles	Mg_2Si
As-cast, E	115	76	30
As-cast, C	111	75	22
Homogenised at 560°C/520°C, E	113	90	31
Homogenised at 560°C/520°C, C	110	88	27
Homogenised at 580°C/520°C, E	111	89	29
Homogenised at 580°C/520°C, C	111	91	24

Table 11.2: Showing part 2 of particle average thresholding greyscale values obtained after several analyses using ImageJ.

Specimen/Condition	Overall intermetallic particle	α-phase particles	Mg_2Si
As-cast, E	112	72	16
As-cast, C	111	70	17
Homogenised at 560°C/520°C, E	114	90	25
Homogenised at 560°C/520°C, C	110	85	21
Homogenised at 580°C/520°C, E	112	91	25
Homogenised at 580°C/520°C, C	112	91	22

Table 11.3: Showing part 3 of particle average thresholding greyscale values obtained after several analyses using ImageJ.

Specimen/Condition	Overall intermetallic particle	α-phase particles	Mg_2Si
As-cast, E	168	114	29
As-cast, C	170	112	28
Homogenised at 560°C/520°C, E	170	136	30
Homogenised at 560°C/520°C, C	170	131	35
Homogenised at 580°C/520°C, E	173	138	33
Homogenised at 580°C/520°C, C	163	127	27

Table 11.4: Showing part 4 of particle average thresholding greyscale values obtained after several analyses using ImageJ.

Specimen/Condition	Overall intermetallic particle	α-phase particles	Mg_2Si
As-cast, E	167	94	29
As-cast, C	169	110	23
Homogenised at 560°C/520°C, E	168	134	37
Homogenised at 560°C/520°C, C	173	138	34
Homogenised at 580°C/520°C, E	173	137	40
Homogenised at 580°C/520°C, C	165	131	29

Table 11.5: Showing part 5 of particle average thresholding greyscale values obtained after several analyses using ImageJ.

Specimen/Condition	Overall intermetallic particle	α-phase particles	Mg_2Si
As-cast, E	170	113	24
As-cast, C	172	115	29
Homogenised at 560°C/520°C, E	170	133	32
Homogenised at 560°C/520°C, C	176	136	35
Homogenised at 580°C/520°C, E	175	141	40
Homogenised at 580°C/520°C, C	168	127	31

11.3 Appendix 3: MATLAB R2013b

The following steps and images seen in Figure 11.10 and Figure 11.11 demonstrate how the MATLAB R2013b program was used to estimate particle volume fraction (VF) within images for each specimen. The program gives Excel spreadsheets as output which contains estimated overall particle and phase VF. The obtained results are averaged, and then presented in the Results and Discussion section 6.1.5.

1 Open MATLAB, both Code and script
2 Enter the file name containing images to be analysed for each specimen in the spaces selected in green
3 Enter threshold values of all the particles within the microstructure of the alloy for each specimen in the spaces (selected in red)
4 Save the script, then run it
5 Excel sheets containing data are produced as outputs (selected in blue) and then saved in the directory folder
6 Repeat steps 2 to 5 using α-phase particles and Mg_2Si particles threshold values

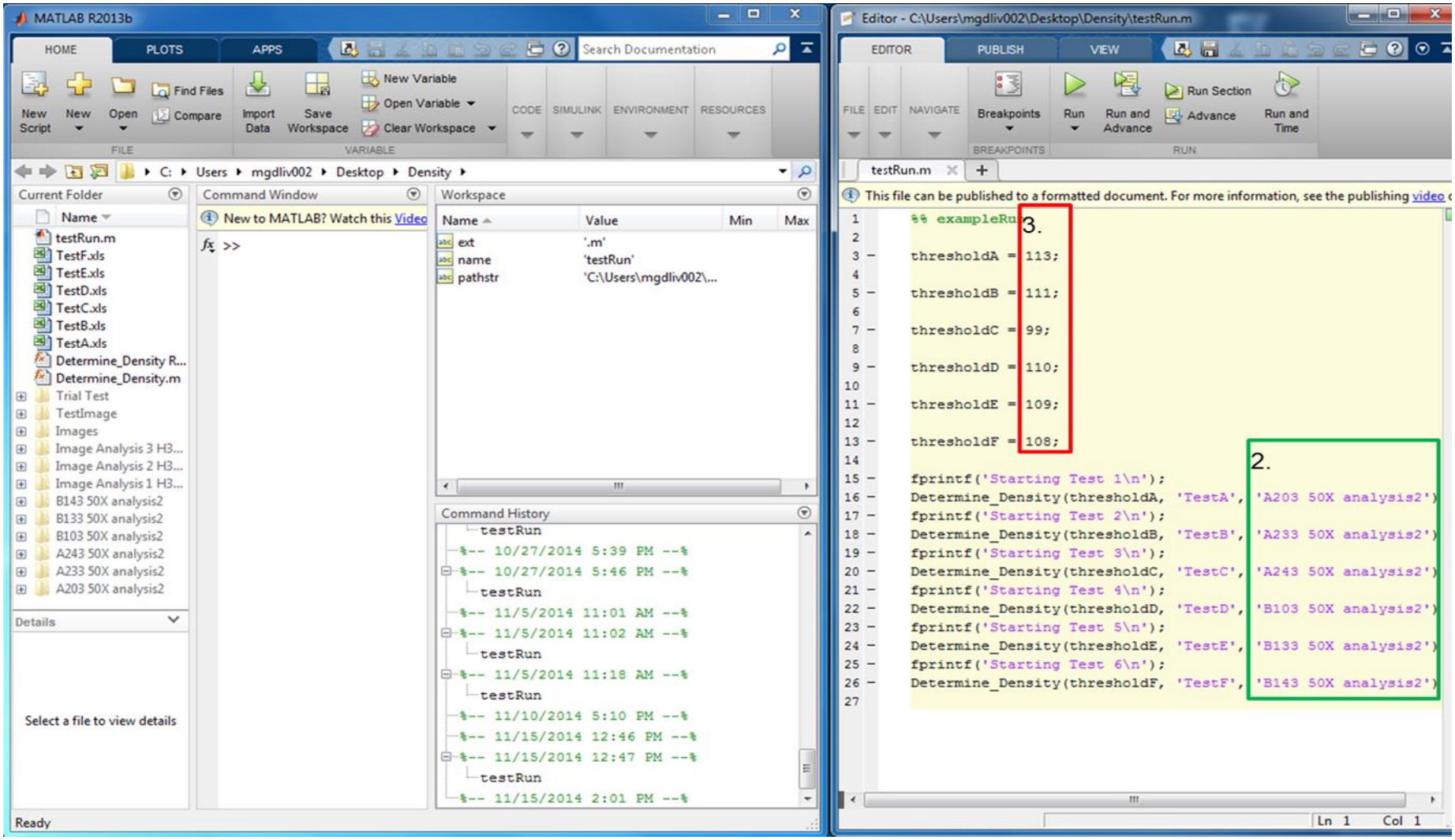

Figure 11.10: Showing the micrograph image directory in the green box and the threshold values in the red box before running the program.

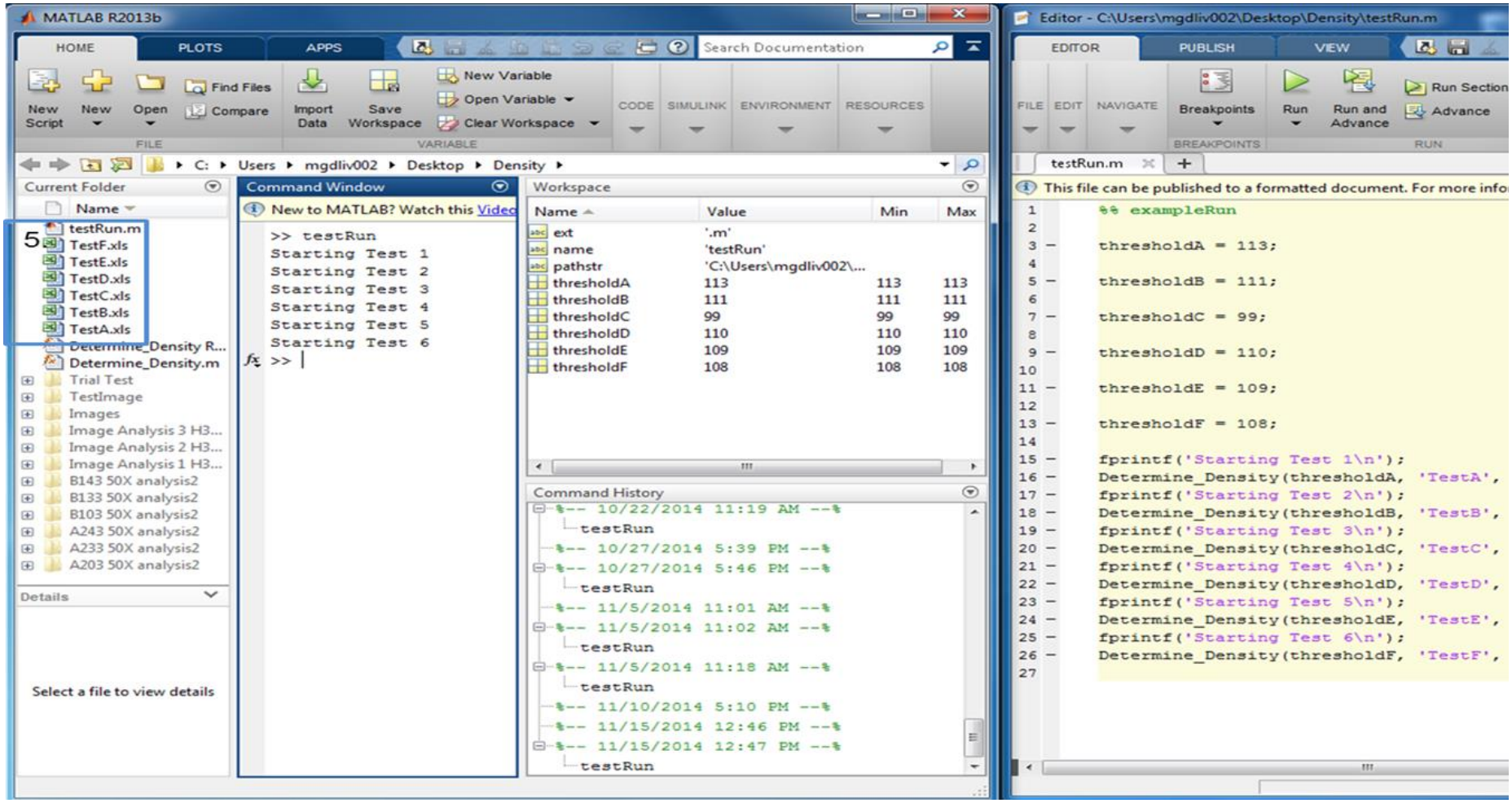

Figure 11.11: Showing the spreadsheet output containing estimated particle VF.

11.4 Appendix 4: Statistical analysis of 2-D phase quantification results using normal distribution and relative accuracy analysis of the data used for image analysis

Table 11.6 and Table 11.7 show the z-value used for data normal distribution and critical z-values associated with a confidence interval used for relative accuracy estimation, respectively.

Table 11.6: Showing the z-values used for normal distribution and relative accuracy [67].

Cumulative Standard Normal Distribution (i.e., P(Z > z), the area to the right of the cut off)

Z	.00	.01	.02	.03	.04	.05	.06	.07	.08	.09
0.0	0.5000	0.4960	0.4920	0.4880	0.4840	0.4801	0.4761	0.4721	0.4681	0.4641
0.1	0.4602	0.4562	0.4522	0.4483	0.4443	0.4404	0.4364	0.4325	0.4286	0.4247
0.2	0.4207	0.4168	0.4129	0.4090	0.4052	0.4013	0.3974	0.3936	0.3897	0.3859
0.3	0.3821	0.3783	0.3745	0.3707	0.3669	0.3632	0.3594	0.3557	0.3520	0.3483
0.4	0.3446	0.3409	0.3372	0.3336	0.3300	0.3264	0.3228	0.3192	0.3156	0.3121
0.5	0.3085	0.3050	0.3015	0.2981	0.2946	0.2912	0.2877	0.2843	0.2810	0.2776
.										
.										
1.5	0.0668	0.0655	0.0643	0.0630	0.0618	0.0606	0.0594	0.0582	0.0571	0.0559
1.6	0.0548	0.0537	0.0526	0.0516	0.0505	0.0495	0.0485	0.0475	0.0465	0.045
1.7	0.0446	0.0436	0.0427	0.0418	0.0409	0.0401	0.0392	0.0384	0.0375	0.0367
1.8	0.0359	0.0351	0.0344	0.0336	0.0329	0.0322	0.0314	0.0307	0.0301	0.0294
1.9	0.0287	0.0281	0.0274	0.0268	0.0262	0.0256	0.0250	0.0244	0.0239	0.0233
2.0	0.0228	0.0222	0.0217	0.0212	0.0207	0.0202	0.0197	0.0192	0.0188	0.0183
3.0	0.0013	0.0013	0.0013	0.0012	0.0012	0.0011	0.0011	0.0011	0.0010	0.0010

Table 11.7: Showing critical z-score values associated with a confidence interval [68].

Confidence level	z critical value
80%	1.28
90%	1.645
95%	1.96
98%	2.33
99%	2.58
99.8%	3.09
99.9%	3.29

11.5 Appendix 5: Intermetallic particle VF estimation results (using MATLAB)

Image analysis was concluded using MATLAB and the averaged results in Table 11.8 to Table 11.12 were obtained. The averaged results were further analysed and then reported in the Results and Discussion section 6.1.5.

Table 11.8: Showing part 1 of the averaged overall and phase particle VF obtained using MATLAB.

Specimen/condition	VF of All particles	Fraction of α-phase % Particles	Fraction of β-phase % Particles
As-cast, E	2.77±0.93	12.71±4.95	85.95±5.55
As-cast, C	2.58±1.61	18.13±14.49	80.75±15.95
Homogenisation at 560°C/520°C, E	2.28±0.74	49.84±9.89	49.81±10.13
Homogenisation at 560°C/520°C, C	2.26±1.19	38.76±15.36	60.49±15.93
Homogenisation at 580°C/520°C, E	2.78±1.08	54.07±8.30	45.33±9.22
Homogenisation at 580°C/520°C, C	1.91±0.98	44.81±15.43	54.56±16.07

Table 11.9: Showing part 2 of the averaged overall and phase particle VF obtained using MATLAB.

Specimen/condition	VF of All particles	Fraction of α-phase % Particles	Fraction of β-phase % Particles
As-cast, E	2.39±0.79	13.51±5.31	86.43±5.34
As-cast, C	2.56±1.59	16.69±13.31	82.97±13.80
Homogenisation at 560°C/520°C, E	2.28±0.74	48.26±9.92	51.67±9.96
Homogenisation at 560°C/520°C, C	2.25±1.19	35.04±14.38	64.63±14.68
Homogenisation at 580°C/520°C, E	2.87±1.09	55.30±8.47	44.37±9.02
Homogenisation at 580°C/520°C, C	2.01±1.03	43.46±15.84	56.03±16.29

Table 11.10: Showing part 3 of the averaged overall and phase particle VF obtained using MATLAB.

Specimen/condition	VF of All particles	Fraction of α-phase % Particles	Fraction of β-phase % Particles
As-cast, E	2.50±0.70	13.01±5.32	86.79±5.46
As-cast, C	2.18±1.25	13.04±12.28	86.81±12.44
Homogenisation at 560°C/520°C, E	2.53±0.80	47.99±9.27	51.98±9.26
Homogenisation at 560°C/520°C, C	2.18±1.09	28.23±15.10	71.68±15.19
Homogenisation at 580°C/520°C, E	2.56±0.79	50.55±8.60	49.42±8.60
Homogenisation at 580°C/520°C, C	1.80±0.98	35.73±14.42	64.24±14.43

Table 11.11: Showing part 4 of the averaged overall and phase particle VF obtained using MATLAB.

Specimen/condition	VF of All particles	Fraction of α-phase % Particles	Fraction of β-phase % Particles
As-cast, E	2.35±0.65	8.78±4.01	91.05±4.11
As-cast, C	2.31±1.45	15.79±16.83	84.19±16.84
Homogenisation at 560°C/520°C, E	2.34±0.72	47.30±9.18	52.67±9.18
Homogenisation at 560°C/520°C, C	2.37±1.10	28.76±15.56	71.22±15.57
Homogenisation at 580°C/520°C, E	2.47±0.80	48.78±8.55	51.17±8.57
Homogenisation at 580°C/520°C, C	1.90±1.01	38.31±15.34	61.65±15.35

Table 11.12: Showing part 5 of the averaged overall and phase particle VF obtained using MATLAB.

Specimen/condition	VF of All particles	Fraction of α-phase % Particles	Fraction of β-phase % Particles
As-cast, E	2.64±0.74	10.61±4.35	89.36±4.37
As-cast, C	2.35±1.32	6.88±7.37	93.08±7.41
Homogenisation at 560°C/520°C, E	2.45±0.74	44.01±9.00	55.97±9.00
Homogenisation at 560°C/520°C, C	2.71±1.14	24.20±14.20	75.79±14.21
Homogenisation at 580°C/520°C, E	2.61±0.84	50.80±8.83	49.15±8.84
Homogenisation at 580°C/520°C, C	2.06±1.05	31.11±13.82	68.84±13.84

11.6 Appendix 6: Dissolution time and product yield

Particle extraction (dissolution) was achieved using the particle extraction technique based on the SiBut method. Table 11.13 shows the time it took for the experiment to complete, the pressure within the autoclave when dissolution occurred as well as the product yield (powder particles) when dissolution was complete.

Table 11.13: Showing experiment time, pressure within autoclave during dissolution and product yield.

Sample name		Drying time	Dissolution time	Initial pressure	Final pressure	Sample (g)	Product yield (Particles) (g)	%		Average	
As-cast, E	1	2 hrs 45min	14 hrs	3.5	Rose to 4.0, dropped to 3.5	2.30	0.05	2.16	2.16	1.00	2.16
	2	1 hrs 45min	9 hrs 20min	3.5	rose to 3.9, dropped to 3.5	1.37	0.04	2.92	5.08	2.00	2.54
	3	2 hrs 15min	9 hrs	4	rose to 5.0, dropped to 3.95	1.34	0.04	2.92	8.00	3.00	2.67
	4	3 hrs 35min	17 hrs	3.5	rose to 5.0, dropped to 3.5	1.27	0.05	3.68	11.68	4.00	2.92
	5	2 hrs 25min	7 hrs 13min	3.5	3.5	1.08	0.05	3.84	15.52	5.00	3.10
	6	2 hrs 17min	12 hrs 55min	3.5	3.45	1.05	0.03	3.02	18.54	6.00	3.09
As-cast, C	1	6 hrs 15min	13 hrs	3.7	3.5	1.09	0.06	5.53	5.53	1.00	5.53
	2	3 hrs 15min	12 hrs	3.8	rose to 5.0, dropped to 3.5	1.35	0.05	3.61	9.14	2.00	4.57
	3	4 hrs 43min	12 hrs 5min	3.7	rose to 5.0, dropped to 3.5	1.37	0.03	2.43	11.57	3.00	3.86

	4	3 hrs 30min	9 hrs	3.5	3.5	1.07	0.02	1.58	13.15	4.00	3.29
	5	3 hrs 5min	2 1hrs 13min	3.6	3.5	1.11	0.03	2.72	15.87	5.00	3.17
	6	3 hrs 50min	20 hrs 32min	3.55	3.5	0.94	0.01	1.00	16.87	6.00	2.81
Homogenisation at 560°C/520°C, E	1	6 hrs	12 hrs	3.7	3.45	1.16	0.04	3.83	3.83	1.00	3.83
	2	3 hrs 10min	12 hrs 10min	3.7	3.5	1.30	0.04	3.36	7.19	2.00	3.60
	3	2 hrs 20min	16 hrs	4	4	0.71	0.02	3.33	10.52	4.00	2.63
	4	3 hrs 15min	10 hrs	4	4	1.09	0.04	3.40	13.92	5.00	2.78
	5	4 hrs 15min	16 hrs 30min	3.96	3.7	1.06	0.03	3.13	17.05	8.00	2.13
	6	3 hrs 18min	15 hrs 50min	4	3.6	1.09	0.03	2.88	19.93	9.00	2.21
Homogenisation at 560°C/520°C, C	1	4 hrs 5min	14 hrs 20min	3.2	3.5	1.32	0.03	2.17	2.17	1.00	2.17
	2	4 hrs 30min	13 hrs 50min	3.4	3.5	1.23	0.04	3.07	5.24	2.00	2.62
	3	3 hrs 22min	7 hrs 18min	4	rose to 5.5, dropped to 3.6	1.26	0.05	3.99	9.23	3.00	3.08
	4	2 hrs 35min	6 hrs	4	rose to 5.5, dropped to 3.7	1.35	0.04	2.98	12.21	4.00	3.05
	5	4 hrs	15 hrs 5min	3.97	3.8	1.08	0.02	1.87	14.08	5.00	2.82
	6	3 hrs 37min	14 hrs 13min	4	3.7	1.07	0.04	3.97	18.05	7.00	2.58
Homogenisation at 580°C/520°C, E	1	5 hrs 25min	16 hrs	2.2	2.5	1.17	0.03	2.21	2.21	1.00	2.21
	2	6 hrs	16 hrs	2.4		1.48	0.05	3.28	5.49	2.00	2.75
	3	2 hrs 20min	15 hrs	3.8	3.5	1.36	0.03	2.31	7.80	3.00	2.60
	4	2 hrs 32min	6 hrs	3.5	3.3	1.05	0.02	1.76	9.56	4.00	2.39
	5	2 hrs 25min	22 hrs	3.9	3.6	1.08	0.02	1.97	11.53	5.00	2.31

	6	2 hrs 45min	17 hrs 16min	3.9	3.6	1.12	0.04	3.86	15.39	7.00	2.20
Homogenisation at 580°C/520°C, C	1	6 hrs 20min	16 hrs	2	2.5	0.91	0.02	2.48	2.48	1.00	2.48
	2	4 hrs 50min	18 hrs 15min	2.8	3	1.71	0.06	3.31	5.79	2.00	2.90
	3	2 hrs 30min	7 hrs	3.7	rose to 5.4, dropped to 3.5	1.36	0.05	4.00	9.79	3.00	3.26
	4	2 hrs 50min	7 hrs	4	rose to 5.2, dropped to 3.7	1.37	0.05	3.30	13.09	4.00	3.27
	5	4 hrs 5min	19 hrs 45min	3.6	3.5	0.99	0.03	3.08	16.17	6.00	2.70
	6	5 hrs 10min	21 hrs 10min	3.7	3.5	1.03	0.02	2.02	18.19	7.00	2.60

11.7 Appendix 7: Statistical analysis of 3-D phase quantification results

The Rietveld method was then conducted on the powder particle XRD patterns generated. The results obtained from this method are statistically analysed and reported in Table 11.14. Furthermore, the obtained results were then averaged in Table 11.15 and a graph in Figure 11.12 was plotted. After that outliers were removed from the data and the new information was reported in the Results and Discussion section 6.3.

Table 11.14: Showing intermetallic particle phase VF estimation by using the Rietveld method before removing outliers.

Phase	Specimen/Condition	Part 1	Part 2	Part 3	Part 4	Part 5
β-Al_6(Fe,Mn)	**As-cast, E**	82	82	70	57	54
	As-cast, C	57	67	68	64	66
	Homogenisation at 560°C/520°C, E	38	40	45	26	38
	Homogenisation at 560°C/520°C, C	29	41	57	14	15
	Homogenisation at 580°C/520°C, E	51	44	20	37	40
	Homogenisation at 580°C/520°C, C	41	46	29	31	36
α-Al_x(Fe,Mn)$_3Si_2$	**As-cast, E**	18	18	30	43	46
	As-cast, C	43	33	32	36	34
	Homogenisation at 560°C/520°C, E	62	60	55	74	62
	5 Homogenisation at 60°C/520°C, C	71	59	43	86	85
	Homogenisation at 580°C/520°C, E	49	56	80	63	60
	Homogenisation at 580°C/520°C, C	59	54	71	69	64

Table 11.15: Showing average intermetallic particle phase VF estimated using the Rietveld method before removing outliers.

Phase	Specimen/Conditon	Average	Standard deviation
β-Al_6(Fe,Mn)	**As-cast, E**	69	12
	As-cast, C	64	4
	Homogenisation at 560°C/520°C, E	37	6
	Homogenisation at 560°C/520°C, C	31	16
	Homogenisation at 580°C/520°C, E	38	10
	Homogenisation at 580°C/520°C, C	37	6
α-Al_x(Fe,Mn)$_3Si_2$	**As-cast, E**	31	12
	As-cast, C	36	4
	Homogenisation at 560°C/520°C, E	63	6
	Homogenisation at 560°C/520°C, C	69	16
	Homogenisation at 580°C/520°C, E	62	10
	Homogenisation at 580°C/520°C, C	63	6

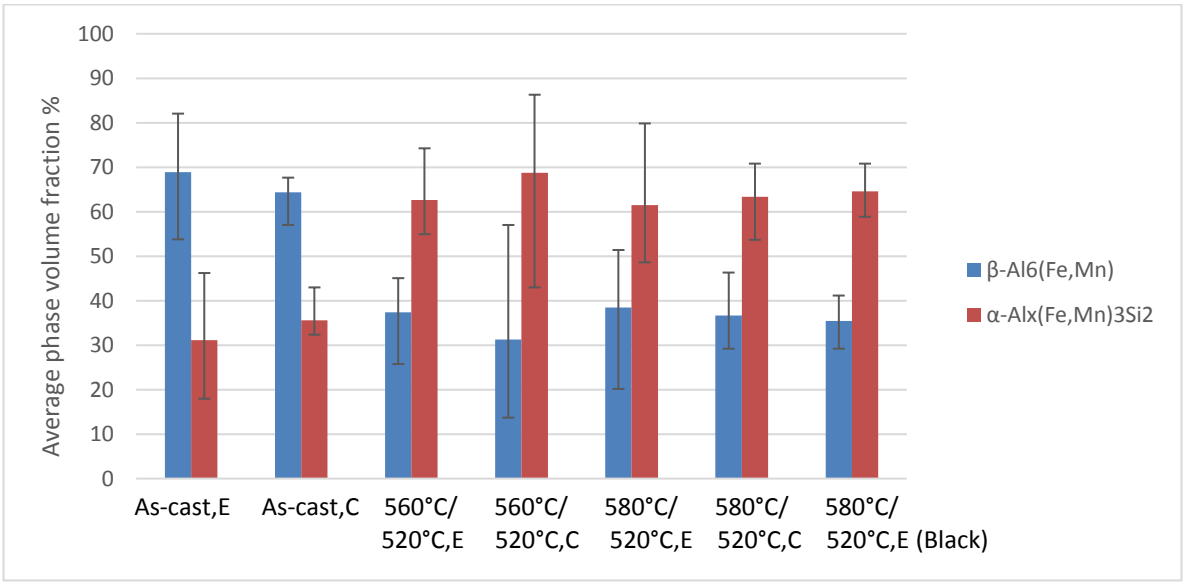

Figure 11.12: Column graph showing average intermetallic phase VF before removing outliers.